
Nonlinear Dual-Comb Spectroscopy

Takuro Ideguchi



München 2014

Nonlinear Dual-Comb Spectroscopy

Takuro Ideguchi

Dissertation
an der Fakultät für Physik
der Ludwig-Maximilians-Universität
München

vorgelegt von
Takuro Ideguchi
aus Ibaraki

München, den 22.01.2014

Erstgutachter: Theodor W. Hänsch

Zweitgutachter: Wolfgang Zinth

Tag der mündlichen Prüfung: 21.02.2014

Zusammenfassung

Laserfrequenzkämme revolutionierten das Wissenschaftsgebiet der absoluten Frequenzmessung. Die Kammlinien haben den stets gleichen Abstand von einander und bilden so ein Frequenz-Lineal unerreichter Genauigkeit, das für die Messung beliebiger Laserfrequenzen eingesetzt werden kann. In den letzten Jahren fanden optische Frequenzkämme zunehmend Eingang in das Feld breitbandiger molekularer Spektroskopie. Bei Wechselwirkung mit einer molekularen Probe tasten sie eine Vielzahl möglicher Übergänge ab. Die Zweifrequenzkammspektroskopie, eine Technik die auf der Zeitdomänen-Interferenz zweier Frequenzkämme mit voneinander verschiedenen Repetitionsraten basiert, ist eine dieser Methoden. Im letzten Jahrzehnt hat selbige Fourier-Transformationsmethode, die ganz ohne bewegliche Bauteile auskommt, eindrucklich demonstriert welches Potential sie zur Aufnahme von multiplexen, breitbandigen, schnellen und präzisen Absorptionsspektren mittels eines einzigen Photodetektors hat. Doch diese Technik hat bisher noch nicht ihre vollen Möglichkeiten ausgeschöpft.

Die vorliegende Arbeit ergründet neuartige Aspekte der Zweifrequenzkammspektroskopie, überwindet einige der verbliebenen Schwierigkeiten und erweitert ihre Anwendbarkeit auf das Gebiet der nichtlinearen Spektroskopie.

Eines der größten Hindernisse sind sehr anspruchsvolle Anforderungen an die Kurzzeitstabilität der Frequenzkämme um ihre Kohärenz während der interferometrischen Messung zu erhalten. Wir präsentieren eine Technik des adaptiven Abtastens, welche die beschriebene Anforderung unter Verwendung von frei laufenden Femtosekundenlasern einhält, ohne dabei Leistungseinbußen hinnehmen zu müssen. Spektren werden in Echtzeit und ganz ohne Stabilisierung oder Software-basierender a posteriori Datenverarbeitung aufgenommen. Ungeachtet dessen, dass diese Methode für lineare Absorptionsmessungen im Nahinfraroten realisiert worden ist, kann jeder Zweifrequenzkammspektroskopie- oder asynchrone Abtastebau davon profitieren.

Frequenzkämme sind derzeit größtenteils im nahinfraroten Wellenlängenbereich verfügbar, weswegen die meisten Demonstrationen der Zweifrequenzkammspektroskopie in selbigem durchgeführt worden sind. Jedoch ist der mittelinfrarote Wellenlängenbereich, in welchem die meisten Moleküle starke Schwingungsübergänge aufweisen, der vielversprechendere Wellenlängenbereich für die Anwendung der Zweifrequenzkammspektroskopie in Hinsicht auf wissenschaftliche Grundlagenforschung und optische Diagnostik. Wir haben deshalb einen synchron gepumpten femtosekundenoptisch-parametrischen Osziallter entwickelt, durchstimmbare zwischen 1,8 und 4,2 μm und mit einer bisher unerreichten Pulsdauer von nur 33 fs. Wir zeigen ferner, dass ein auf einem Chip integrierter Silikon-Nanodraht das Spektrum eines solchen mittelinfraroten Frequenzkammes so zu verbreitern vermag, dass es mehr eine Oktave abdeckt.

Da Frequenzkämme intensive ultrakurze Pulse emittieren können nichtlineare Interaktionen mit einer Probe ausgenutzt werden. Wir demonstrieren die ersten Experimente zur nichtlinearen Zweifrequenzkammspektroskopie und nutzen insbesondere nichtlineare Ramaneffekte aus. Zwei Ansätze welche den Raman-induzierten Kerr-Effekt und kohärente Stokes- und Anti-Stokes Ramanstreuung involvieren werden erforscht. Sie untersuchen eine breite Spanne an fundamentalen Schwingungsübergängen einer Probe in flüssiger Phase. Solche Methoden, die auch auf weitere nichtlineare Phänomene ausgedehnt werden können, sind in Bezug auf Echtzeitspektroskopie und bildgebende Verfahren vielversprechend; Beispiele hierfür wären die Verfolgung chemischer Reaktionen und die Mikroskopie biologischer Proben ohne deren vorherige Färbung.

Abstract

Laser frequency combs have revolutionized the field of absolute frequency measurements. The evenly spaced comb lines provide an optical frequency ruler of unprecedented precision, good for the measurement of any laser frequency. In recent years, frequency combs have been extended to the field of broadband molecular spectroscopy. When interacting with a molecular sample, they may interrogate a vast range of transitions. Dual-comb spectroscopy, based on time-domain interference between two combs of slightly different repetition frequencies, is one of these techniques. In the past decade, this technique of Fourier transform spectroscopy without moving parts has demonstrated an exciting potential for the acquisition of multiplex, broadband, rapid and precise spectra with a single photodetector. The technique has, however, not realized its full capabilities yet.

This thesis explores novel aspects of dual-comb spectroscopy, whilst overcoming some of its remaining difficulties and expanding its capabilities to the field of nonlinear spectroscopy.

One of the main impediments of dual-comb spectroscopy is the demanding condition on the short-term stability of the combs to maintain their coherence throughout the entire interferometric measurement. We demonstrate a technique of adaptive sampling that meets such a requirement with free-running femtosecond lasers, without sacrificing performance. Real-time spectra are measured without any stabilization nor post computational data processing. Although implemented with linear absorption spectroscopy in the near-infrared, the technique could benefit any kind of dual-comb or asynchronous sampling set-up.

Currently, frequency comb sources are essentially available in the near-infrared region and consequently most of the demonstrations of dual-comb spectroscopy have been performed in this domain. The mid-infrared spectral range, where most molecules have strong vibrational transitions, is, however, the most promising region for the applications of linear absorption dual-comb spectroscopy to fundamental science and optical diagnostics. We have thus developed a synchronously-pumped femtosecond optical parametric oscillator tunable between 1.8 and 4.2 μm , with a record pulse duration of 33 fs. We show that a silicon nanowire on a chip broadens the spectrum of such mid-infrared comb to span more than one octave.

Since frequency combs emit intense ultrashort pulses, nonlinear interactions with the sample may be harnessed. We demonstrate the first experiments of nonlinear dual-comb spectroscopy and exploit nonlinear Raman effects. Two schemes involving the Raman-induced Kerr effect and coherent Stokes and anti-Stokes Raman scattering are explored. They interrogate a broad span of fundamental vibrational transitions with μs -scale measurement times and a resolution only limited by the intrinsic linewidth of the vibrational transitions of the liquid sample. Such techniques, which could be extended to other nonlinear phenomena, hold much promise for new approaches to real-time spectroscopy and imaging, like e.g. chemical reaction monitoring or label-free microscopy of biological samples.

Contents

1. Introduction	1
2. Frequency comb and molecular spectroscopy	5
2.1. Frequency comb	5
2.1.1. Principle of laser frequency comb	6
2.1.2. Direct frequency comb molecular spectroscopy	8
2.2. Dual-comb spectroscopy	9
2.2.1. Fourier transform spectroscopy	9
2.2.2. Principle of dual-comb spectroscopy	11
2.2.3. Brief review of literature on dual-comb spectroscopy	16
I Linear dual-comb spectroscopy	19
3. Adaptive dual-comb spectroscopy	21
3.1. Background	21
3.1.1. Stability requirements of combs in dual-comb spectroscopy	22
3.2. Stability characterization of the free-running femtosecond lasers	24
3.3. Adaptive sampling with a single adaptive signal	24
3.3.1. Principle	25
3.3.2. Mathematical description	26
3.3.3. Experimental setup	27
3.3.4. Results and discussion	28
3.4. Adaptive dual-comb spectroscopy with two adaptive signals	31
3.4.1. Principle	31
3.4.2. Mathematical description	32
3.4.3. Experimental setup	34
3.4.4. Results and discussion	35
3.5. Adaptive dual-comb spectroscopy in the visible with nonlinear frequency conversion	40
3.5.1. Experimental setup	40
3.5.2. Results and discussion	42
3.6. Conclusion	43

4. Development of a mid-infrared frequency comb	47
4.1. Background	48
4.1.1. Mid-infrared frequency combs	48
4.1.2. Direct mid-infrared frequency comb spectroscopy	50
4.2. Ultrashort synchronously pumped optical parametric oscillator	50
4.2.1. Developed OPO system	51
4.2.2. Nonlinear crystal	52
4.2.3. Characterization of the mid-infrared idler pulse	53
4.3. Mid-infrared supercontinuum generation in Silicon waveguide	58
4.3.1. Silicon waveguide	59
4.3.2. Experimental setup	60
4.3.3. Mid-infrared supercontinuum spectrum	61
4.3.4. Coherence	61
4.4. Conclusion	62
II Nonlinear dual-comb spectroscopy	65
5. Raman-induced Kerr-effect dual-comb spectroscopy	69
5.1. Background	69
5.1.1. Stimulated Raman spectroscopy	69
5.1.2. Raman-induced Kerr-effect spectroscopy	72
5.2. Principle	73
5.3. Experimental setup	73
5.3.1. Yb fiber laser and power amplifier (Pump laser)	75
5.3.2. Synchronization of the pump and Stokes lasers	76
5.4. Results and discussion	78
5.5. Conclusion	81
6. Coherent anti-Stokes Raman dual-comb spectroscopy and microscopy	83
6.1. Background	83
6.1.1. Coherent anti-Stokes Raman spectroscopy	83
6.2. Principle	85
6.2.1. Impulsive stimulated Raman scattering	85
6.2.2. Fourier transform CARS	86
6.2.3. Dual-comb CARS	88
6.3. Spectroscopy	91
6.3.1. Experimental setup	91
6.3.2. Recording parameters	92
6.3.3. Results and discussion	94
6.3.4. Time-resolved spectroscopy	96
6.3.5. Heterodyne detection	97
6.4. Hyperspectral imaging	99

6.4.1. Experimental setup	99
6.4.2. Results and discussion	99
6.5. Duty cycle	102
6.5.1. Demonstration of duty cycle improvement	104
6.6. Differential detection of CARS and CSRS	105
6.6.1. Principle	106
6.6.2. Experimental setup	107
6.6.3. Results and discussion	107
6.7. Conclusion	109
6.8. Comparison between DC-RIKES and DC-CARS	111
7. Summary and outlook	115
List of publications	140
Conference contributions	142
Curriculum Vitae	144
Acknowledgments	146

Chapter 1

Introduction

Optical spectroscopy has greatly contributed to the development of fundamental science and applied technologies. This is due to the fact that there are many types of light-matter interactions, e.g. absorption, scattering, emission etc., which can provide different material information through linear or nonlinear material responses to an applied optical field. While elaborate precision spectroscopy of static materials have given fruitful insights on the basic rules of the nature, time-resolved rapid spectroscopy has played a big role for investigating dynamics of the nature. Concerning time-resolved rapid spectroscopy, improving the measurement speed can provide opportunities not only to investigate new science but also to have new diagnostic tools with an unprecedented fine time-resolution [1]. In general, however, speeding up spectral measurements often accompanies with trade-offs: degrading either spectral bandwidth, precision or sensitivity, though these spectral parameters are important especially for quantitative measurements such as lineshape or concentration analysis. Although achieving high performances for all of them is always a challenge, advanced laser technologies could provide innovative solutions.

The optical frequency comb has revolutionized optical precision measurements with its broadband and highly coherent nature [2, 3]. Beyond its original purpose, the laser frequency comb has been harnessed for other applications including optical broadband spectroscopy [4]. The evenly-spaced narrow laser lines are an ideal spectroscopy source if it is combined with a proper detection scheme. Among the spectroscopy schemes involving a frequency comb, e.g. dispersive spectroscopy [5, 6], Fourier transform spectroscopy [7] etc., dual-comb spectroscopy is a unique way that brings out the potential of the frequency comb, especially its inherent capability of rapid measurements. This comb spectroscopy has shown unprecedented measurement speed as well as high accuracy, high resolution and

robustness.

Although many proof-of-principle demonstrations have been shown the significant potential of the dual-comb spectroscopy, there still have been remaining challenges to bring out the full potential. If these challenges are overcome, it could push this technology to the next stage: namely, for example, where the broadband and ultra-rapid dual-comb spectroscopy accesses the molecular fundamental vibrational transitions, the most interesting and useful features of molecules, with an easy implementation. This thesis addresses the challenges toward this end.

Before getting into the heart of the thesis, **Chapter.2: Frequency comb and molecular spectroscopy** provides the basics of laser frequency combs and dual-comb spectroscopy, and then give an overview of the literature dealing with frequency comb spectroscopy and dual-comb spectroscopy to clarify the position of this work.

The achievements of this thesis are divided into two parts: **Part.I**, Linear dual-comb spectroscopy (Chapter.3, Chapter.4) and **Part.II**, Nonlinear dual-comb spectroscopy (Chapter.5, Chapter.6).

Part.I, Linear dual-comb spectroscopy deals with the challenges in the linear interaction regime.

One of the fundamentally important challenges to be addressed is the spectrum distortion due to the laser instability. Since the measurement time of the dual-comb spectroscopy is in the range of microseconds to milliseconds, the intrinsic laser noise at high frequency, which is not easy to eliminate even with state-of-the-art stabilization technique, causes relative timing and phase jitters between the combs and distorts the dual-comb spectra. **Chapter.3: Adaptive dual-comb spectroscopy** proposes and demonstrates a new technique which elegantly avoids the distortion without elaborate stabilization of the combs nor post computational processing. This technique only uses free-running mode-locked lasers and therefore drastically eases implementation of dual-comb spectroscopy. This invention could become a trigger to provide the new rapid measurement scheme to non-laser specialists in a variety of fields. This could also serve to nonlinear dual-comb spectroscopy introduced in **Part.II**.

Exploring the potential of dual-comb spectroscopy for interrogating fundamental molecular vibrational transitions is an intriguing challenge. There are many applications in a variety of fields based on molecular vibrational spectroscopy from fundamental molecular science to medical, biological and material sciences where it is mostly used as a diagnostics tool. Such vibrational spectroscopy has been featured especially in biomedical imaging with the term “label-free imaging” because monitoring fluorescent labels, which are the standard technique to make image of the target molecules, is not required anymore if one directly probes the inherent molecular vibrations. Therefore one can avoid the perturbation due to the target molecules and ease the sample treatments before measurements.

Chapter.4: Development of a mid-infrared frequency comb deals with the development of a mid-infrared frequency comb appropriate for linear dual-comb spectroscopy of molecular fundamental vibrational transitions. While linear dual-comb spectroscopy in the mid-infrared region would be a straight-forward way to access the fundamental molecular vibrational transitions, suitable mid-infrared frequency combs are still missing. This chapter first give an overview of the current situation of the development of mid-infrared frequency combs, and this work focuses on a mid-infrared frequency comb based on an optical parametric oscillator because its high nonlinear frequency conversion efficiency, low noise, large spectral tunability are all attractive for the dual-comb spectroscopy. Especially we focus on achieving ultrashort pulses with broad spectral bandwidth. Additionally, a new spectral broadening scheme in the mid-infrared region with a silicon waveguide on a chip is also demonstrated to achieve much broader spectral span of the mid-infrared frequency comb.

Part.II, Nonlinear dual-comb spectroscopy pioneers nonlinear spectroscopy with the dual-comb technique. As frequency combs emit intense ultrashort pulses, nonlinear interactions with the sample may be harnessed. Investigating the potential of nonlinear spectroscopy with rapid and broadband dual-comb spectroscopy can open a window of new science and technologies. This thesis especially deals with nonlinear coherent Raman spectroscopy which is another approach to access the molecular fundamental vibrational transitions by utilizing nonlinear Raman scattering. While linear dual-comb spectroscopy requires technically demanding mid-infrared frequency combs, Raman transitions allow to use laser sources in any frequency region, therefore molecular fundamental vibrational tran-

sitions are readily accessible with sophisticated commercially available frequency combs in the near-infrared region. We, for the first time, demonstrate nonlinear Raman scattering processes with the dual-comb method. The nonlinear effects enhance the intensity of the Raman signals when compared to the weak spontaneous Raman emission and enable rapid measurements.

Chapter.5: Raman-induced Kerr-effect dual-comb spectroscopy utilizes Raman-induced Kerr-effect (RIKE), which is closely related to stimulated Raman scattering (SRS). This is the first demonstration of nonlinear dual-comb spectroscopy as well as the first dual-comb spectroscopy based on Raman transitions. This work successfully reveals Raman signals of C-H stretching modes around 3000 cm^{-1} , however, this experiment practically requires a complicated system with three laser sources. This situation motivates the development of another approach investigated in the next chapter.

Chapter.6: Coherent anti-Stokes Raman dual-comb spectroscopy and microscopy utilizes coherent anti-Stokes Raman scattering (CARS) instead. In this scheme, only two near-infrared frequency combs are required and the implementation is nearly as simple as conventional linear dual-comb spectroscopy. This approach accesses the broadband molecular fingerprinting area below 1500 cm^{-1} within unprecedented measurement speed. This dual-comb based broadband and ultra-rapid molecular fingerprinting spectroscopy may have promising future to bring distinguishing new applications in a variety of fields of science and technology.

Chapter.7: Summary and outlook conclude the work of this thesis and discuss further future developments.

Chapter 2

Frequency comb and molecular spectroscopy

Since the advent of the optical frequency comb that revolutionized optical precision measurement, the laser has been an enabling tool in this field [2, 3, 8–10]. Unexpectedly, a variety of other applications of the frequency comb have been proposed and demonstrated afterwards [4]. Broadband direct frequency comb molecular spectroscopy is one of such applications. This chapter provides an overview of the relation between frequency combs and broadband molecular spectroscopy.

2.1 Frequency comb

The optical frequency comb demonstrated its full potential in the late 90s and the invention has had a tremendous impact in the field of precision measurement [2, 3, 8–10]. The optical frequency comb works as a frequency ruler in the optical frequency domain and enables to measure absolute optical frequencies within the accuracy of an atomic clock. With such high accuracy, for example, the frequency of the 1S-2S two-photon transition in atomic hydrogen, the most accurately calculated atomic transition with the theory of quantum electrodynamics (QED), has been measured to address tests of fundamental physics [11, 12]. Optical frequency combs provide the long missing clockwork mechanism for optical atomic clocks [13]. Several types of optical atomic clocks based on an electronic transition in, e.g. a trapped ion [14], trapped neutral atoms in an optical lattice [15, 16], are now considered as the next generation of frequency standard. Other examples of applications, which are beyond the original purpose, are, for example, calibration of an astronomical spectrograph [17, 18], and attosecond science [19, 20]. For calibration of an astronomical spectrograph, a

frequency comb, called “astro-comb”, is harnessed as a calibration light source which could become an improved alternative to conventional gas-based lamp calibration sources. It increases the calibration accuracy by about a hundredfold, which lets astronomers pursue fundamental discoveries in precision astronomy. Attosecond science requires few cycle pulses to generate attosecond pulses through high-harmonic generation and to investigate electron motion. The waveform of a few cycle pulse is highly dependent on the phase of the carrier wave against the pulse envelope, called carrier-envelope phase (CEP), so that the technique to stabilize the CEP, originally invented for realization of the frequency comb, is crucial. Moreover, frequency/time transfer [21–23], low-phase-noise microwave generation [24], ranging coherent LIDAR [25, 26], arbitrary optical/radio frequency (RF) waveforms [27] have been demonstrated with frequency combs. In terms of spectroscopy, a frequency comb or a dual-comb system [28] can be used for calibration of a frequency-tunable continuous-wave laser [28–30]. The technique boosts the calibration speed and accuracy over conventional ways based on gas absorptions. The other approach is direct frequency comb spectroscopy which utilizes all the comb lines of broadband spectrum to directly interrogate the sample. This thesis explores the potential of direct frequency comb spectroscopy.

2.1.1 Principle of laser frequency comb

In order to describe a laser frequency comb, we consider the case where a pulse with a carrier frequency f_c circulates in a laser (linear) cavity of length L . The output of the laser consists in a pulse train which repetition frequency f is the inverse of the pulse round-trip time $T = 1/f = v_g/2L$, where v_g is cavity’s mean group velocity defined by the round-trip time. The pulses do not have an identical electric field because the pulse envelope $A(t)$ propagates in the cavity with a group velocity v_g while its carrier wave travels with a phase velocity v_c . The discrepancy between v_g and v_c comes from the intracavity material dispersion and results in a carrier phase slippage with respect to the pulse envelope after each round trip by an amount of $\Delta\phi$. Assuming a perfect periodicity of the pulse envelope and a constant phase slippage, the electric field of the pulse train ($E(t)$) may be written:

$$\begin{aligned}
 E(t) &= A(t)\exp(-i2\pi f_c t) + c.c. \\
 &= \sum_{n'} A_{n'} \exp\{-i2\pi(f_c + n'f)t\} + c.c. \\
 &= \sum_n A_n \exp\{-i2\pi(f_0 + nf)t\} + c.c.
 \end{aligned} \tag{2.1}$$

where n is an integer, and A_n is a Fourier component of $A(t)$. f_0 is the carrier-envelope offset (CEO) frequency. Since the carrier frequency f_c is not necessarily an integer multiple

of the repetition frequency f , an offset frequency f_0 may be chosen to satisfy $0 \leq f_0 < f$, and each frequency component may be written:

$$f_n = f_0 + nf \quad (2.2)$$

The carrier envelope offset (CEO) frequency f_0 is related to the carrier envelope phase slippage $\Delta\phi$ by:

$$\Delta\phi = 2\pi f_0/f \quad (2.3)$$

The Equation.2.1 implies that the Fourier transform of the periodic pulse train is a spectrum which consists of equally spaced lines with the mode spacing of f and the offset frequency of f_0 (Figure.2.1).

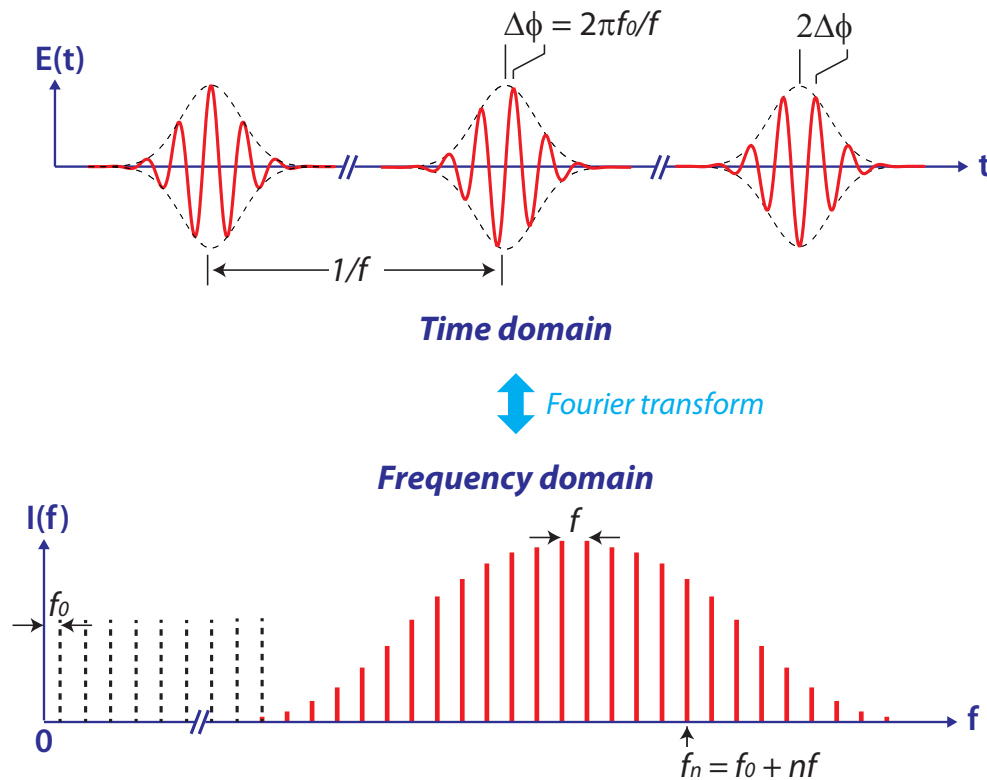


Figure 2.1: Time and frequency domain picture of frequency comb

The comb structure written in the Equation.2.1 results from the assumption of periodic pulse envelope ($T = 1/f = \text{const.}$) and constant carrier phase slippage ($\Delta\phi = 2\pi f_0/f = \text{const.}$). In the real world, however, these values fluctuate because of different kind of noises, therefore one needs to stabilize these two degrees of freedom to obtain the comb structure. Although the periodicity of the pulse envelope is easily monitored and stabilized, monitoring the carrier phase slippage is not trivial because the oscillation frequency of the

carrier wave is too high for electronic devices. The so-called f-2f interferometer enables to monitor the carrier envelope offset frequency f_0 which results in realization of a self-referenced optical frequency comb. The self-referenced optical frequency comb works as a frequency gear which transfers the frequency accuracy of an atomic clock in the radio frequency to the optical frequency region. Although the first self-referenced optical frequency comb was demonstrated with a Ti:Sa femtosecond mode-locked laser [31, 32], fiber laser based frequency combs are, nowadays, widely used because of their turn-key operation. Fully equipped commercial frequency combs are also available.

2.1.2 Direct frequency comb molecular spectroscopy

All the comb lines of a frequency comb can be used to interrogate molecular transitions over a broadband spectral bandwidth. Since a frequency comb consists of a highly coherent ultrashort pulse train, it holds two aspects which may seem contradictory: single-frequency-precision and broad-bandwidth. This feature promises that direct frequency comb spectroscopy merges advantages of the conventional spectroscopy in two other directions, precision measurement based on a continuous-wave laser and broadband measurement based on a short pulsed laser. In order to benefit from the superior accuracy, the comb structure has to be resolved with sufficient instrumental resolution.

Several detection methods have been invented for such comb-resolving spectroscopy. At large comb tooth spacing, a high-resolution virtually imaged phased array (VIPA) disperser with a diffraction grating can be a comb resolving spectrometer [5]. The combination of two dispersive elements successfully separates every single spectral component of the frequency comb in space and maps them onto a 2D CCD camera, which enables to detect all the comb lines at the same time. At narrow comb tooth spacing, a Vernier spectrometer, which consists of a scanning Fabry-Perot resonator, a grating and a CCD camera, can be a comb-resolving spectrometer [6]. Although these dispersive spectrometer can resolve the comb lines, the requirement of a 2D CCD camera is cumbersome in some applications, e.g. data transfer speed of such a camera leads to limited measurement speed. Furthermore, it is not readily available over the entire electromagnetic spectrum, especially demanding in the mid-infrared region because 2D cameras in the mid-infrared have a poor sensitivity due to the thermal noise, and also the materials for detectors are expensive. Fourier-transform spectroscopy is another approach. The combination of a frequency comb and a Michelson-based Fourier transform spectrometer brings a significant improvement of the sensitivity over a conventional Fourier transform spectrometer based on an incoherent light source [7]. The practical advantage of this method over the dispersive spectrometer is that it only uses

one detector instead of multi-elements detector such as a 2D camera. This relaxes constraint of detectable wavelength region because a single detector is readily available in most regions. In this sense, a mid-infrared frequency comb with a Michelson Fourier transform spectrometer is suitable for broadband direct comb molecular vibrational spectroscopy [33]. In order to resolve the comb structure, however, a long range mechanical scanning stage is required, e.g. a 1.5 m long stage to resolve 100 MHz comb tooth spacing. Moving a stage over such long distance within interferometric precision is very demanding in practice. Dual-comb spectroscopy elegantly overcomes this practical difficulty with motion-less pulse delay principle (Section.2.2). As shown above, direct frequency comb spectroscopy successfully merges the precise and broadband capabilities of frequency comb. Moreover, frequency comb holds a big potential, namely ultra-rapid broadband spectroscopic measurement. Since frequency comb is based on an ultrashort pulse-train at high repetition rate, the high frequency periodicity can bring an efficient measurement in time. From this point of view, however, most of the spectroscopy instruments limit the measurement speed and the high-speed capability of the light source due to the e.g. charge transfer speed in a CCD camera, speed of mechanical motion in a Michelson interferometer etc. Dual-comb spectroscopy overcomes these limitations with its working principle without moving parts, therefore it is a suitable method to achieve rapid broadband spectroscopy. The work in this thesis mainly focuses on the high-speed capability.

2.2 Dual-comb spectroscopy

Among several types of direct frequency comb spectroscopy, dual-comb spectroscopy has a unique standpoint: the method holds great potential both for precision measurement with resolved comb lines and for ultra-rapid measurement. The temporal coherence property of consecutive pulses of frequency comb can be efficiently utilized by combination of two frequency combs with slightly detuned repetition frequencies.

2.2.1 Fourier transform spectroscopy

Dual-comb spectroscopy is a technique of Fourier transform spectroscopy, therefore we first introduce the principle of conventional Fourier transform spectroscopy based on a Michelson interferometer. The method was developed in the late 1950s [34], and since then it has been used as a workhorse for broad-spectral-band measurements in a variety of scientific and industrial fields. The major fundamental advantage of the method over dispersive spectroscopy is the multiplex (Fellgett's) advantage, which comes from the fact that all the spectral information is collected simultaneously. This results in a higher signal-to-noise

ratio for a given time and consistency of the measurement over dispersive spectrometers. A Michelson interferometer splits a broadband light source into two beams of equal intensity and both are combined again with a certain optical delay τ which is induced by a mechanical delay-stage in an arm of the interferometer (Figure.2.2). The electric fields at the output of the interferometer are identical except for the phase shift. The combined electric field may be written $E(t) + E(t - \tau)$. The photodetector only sees the optical intensity of the field:

$$I(\tau) = \int_{-\infty}^{\infty} |E(t) + E(t - \tau)|^2 dt \quad (2.4)$$

This intensity contains a field autocorrelation, called interferogram, term as a function of the delay¹ τ :

$$S(\tau) = \int_{-\infty}^{\infty} E(t)E^*(t - \tau)dt + c.c. \quad (2.5)$$

The Wiener-Khinchin theorem tells that the Fourier transform of the field autocorrelation (interferogram) is the spectrum of the field $E(t)$. Complex spectrum $B(\nu)$ in the frequency ν may be written:

$$B(\nu) = \int_{-\infty}^{\infty} S(\tau)\exp(-i2\pi\nu\tau)d\tau \quad (2.6)$$

Due to the relation of Fourier transform, the inverse Fourier transform of the spectrum $B(\nu)$ is the interferogram:

$$S(\tau) = \int_{-\infty}^{\infty} B(\nu)\exp(i2\pi\nu\tau)d\nu \quad (2.7)$$

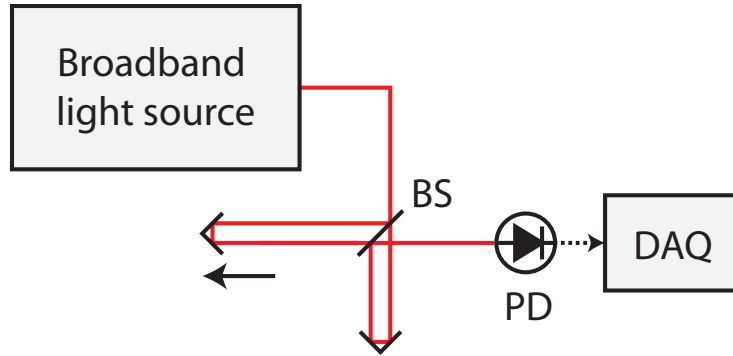


Figure 2.2: Fourier transform spectroscopy based on a Michelson interferometer. BS: beam-splitter, PD: photodetector, DAQ; data acquisition device

¹In practice, τ is limited within a certain range.

Michelson Fourier transform spectroscopy with a frequency comb

Here we consider the case where a frequency comb is the input light source of a Michelson interferometer with a constantly moving mirror of velocity v . The delay τ of the interferometer may be written:

$$\tau = 2vt/c \quad (2.8)$$

With the electric field of a frequency comb (Equation.2.1), the interferogram (Equation.2.5) may be written:

$$\begin{aligned} S(t) &= \int_{-\infty}^{\infty} \sum_n A_n A_n^* \exp\{2\pi i(f_0 + nf)2v/ct\} dt + c.c. \\ &\propto \sum_n A_n A_n^* \exp\{2\pi i(f_0 + nf)2v/ct\} + c.c. \end{aligned} \quad (2.9)$$

we only chose the pairs of the nearest combs which have the same comb number n . This is experimentally done easily by proper low-pass filtering. According to the Equation.2.6, the power spectral density is:

$$\begin{aligned} B(\nu) &\propto \int_{-\infty}^{\infty} S(t) \exp(-i2\pi\nu t) dt \\ &= \int_{-\infty}^{\infty} \sum_n A_n A_n^* \exp[-2\pi i\{\nu - (f_0 + nf)2v/c\}t] dt + c.c. \\ &= \sum_n A_n A_n^* \delta\{\nu - (f_0 + nf)2v/c\} + c.c. \end{aligned} \quad (2.10)$$

where $\delta\{\nu - (f_0 + nf)2v/c\}$ describes a Dirac delta function. This equation shows that the spectrum of the frequency comb is mapped onto the down-converted frequency region with a down-conversion factor of $2v/c$. For example, a moving mirror with velocity of 15 mm/s provides down-conversion factor 10^{-10} , hence an optical frequency (e.g. 100 THz) is down-converted to the audio frequency range (10 kHz).

2.2.2 Principle of dual-comb spectroscopy

The Michelson interferometer can be replaced by a second frequency comb which repetition frequency ($f + \delta f$) is slightly different from that of the first frequency comb (f) (Figure.2.3). In the time domain, due to the difference of repetition frequencies, the time delay between pairs of pulses (one from each frequency comb) increases linearly by an amount of $\delta f/f^2$ from pulse-pair to pulse-pair. The automatically scanned delay plays a comparable role to that of the moving mirror in the Michelson interferometer. In the dual-comb case, however, much faster scan is possible because of the absence of moving parts.

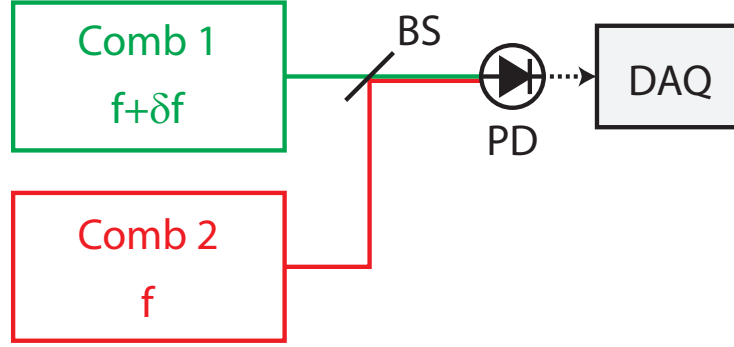


Figure 2.3: Dual-comb spectroscopy

According to the Equation.2.1, the electric fields of the frequency combs are written:

$$E_1(t) = \sum_n A_{1,n} \exp[-i2\pi\{f_{1,0} + n(f + \delta f)\}t] + c.c. \quad (2.11)$$

$$E_2(t) = \sum_n A_{2,n} \exp[-i2\pi\{f_{2,0} + nf\}t] + c.c. \quad (2.12)$$

where $A_{i,n}$ and $f_{i,0}$ are a Fourier component of a pulse envelope $A_i(t)$ and the carrier-envelope offset (CEO) frequency of each comb ($i = 1, 2$). The two pulse trains are combined by a beamsplitter and detected on a single photodetector. The signal intensity may be written:

$$I(t) \propto |E_1(t) + E_2(t)|^2 \quad (2.13)$$

This signal contains many frequency components, but here, we only consider the combination between the nearest comb teeth of frequency comb 1 and comb 2. This selection, in practice, can be easily made by proper low-pass electronic filtering. An interferogram may be written:

$$S(t) \propto \sum_n A_{1,n} A_{2,n}^* \exp\{-i2\pi(\delta f_0 + n\delta f)t\} + c.c. \quad (2.14)$$

Where $\delta f_0 = f_{1,0} - f_{2,0}$ is the difference in offset frequency of comb 1 and comb 2. The Fourier transform of the interferogram reveals the spectrum:

$$B(\nu) \propto \sum_n A_{1,n} A_{2,n}^* \delta\{\nu - (\delta f_0 + n\delta f)\} + c.c. \quad (2.15)$$

The Equation.2.15 tells that the spectrum of the frequency comb is mapped to a lower frequency region with the down-conversion factor of $\delta f/f$. The factor can be optimized by the difference in repetition frequency δf and is typically about 10^{-6} , hence optical frequency scale, e.g. a 10 THz bandwidth comb, down-converted to the radio frequency range, a 10 MHz bandwidth comb.

Molecular linear-absorption dual-comb spectroscopy

All the situations explained above analyze the light source itself. In order to extract information on the investigated molecules, the sample can be inserted into the optical path. There are two possible configurations for inserting the sample (Figure.2.4), (a) in a beam path of one of the combs before combining the two combs, (b) in a beam path after combining the two combs. In the case of (a), while the second comb works as a pure local oscillator, the first comb interacts with the sample and the electric field at the detector may be written:

$$E_1(t) = \sum_n A_{1,n} \exp[-\alpha_{1,n} - i\phi_{1,n} - i2\pi\{f_{1,0} + n(f + \delta f)\}t] + c.c. \quad (2.16)$$

where $\alpha_{1,n}$ is amplitude attenuation factor and $\phi_{1,n}$ is phase shift of the electric field due to the sample. The interferogram and the spectrum are written:

$$S_{(a)}(t) \propto \sum_n A_{1,n} A_{2,n}^* \exp\{-\alpha_{1,n} - i\phi_{1,n} - i2\pi(\delta f_0 + n\delta f)t\} + c.c. \quad (2.17)$$

$$B_{(a)}(\nu) \propto \sum_n A_{1,n} A_{2,n}^* \exp(-\alpha_{1,n} - i\phi_{1,n}) \delta\{\nu - (\delta f_0 + n\delta f)\} + c.c. \quad (2.18)$$

This shows that a complex Fourier transform reveals both the amplitude attenuation and phase shift induced by the sample. This results from the fact of using the comb 2 as the local oscillator.

In the case of (b), both combs interact with the sample, and the spectrum may be written:

$$\begin{aligned} B_{(b)}(\nu) &\propto \sum_n A_{1,n} A_{2,n}^* \exp\{-(\alpha_{1,n} + \alpha_{2,n}) - i(\phi_{1,n} - \phi_{2,n})\} \delta\{\nu - (\delta f_0 + n\delta f)\} + c.c. \\ &= \sum_n A_{1,n} A_{2,n}^* \exp(-2\alpha_n) \delta\{\nu - (\delta f_0 + n\delta f)\} + c.c. \end{aligned} \quad (2.19)$$

where $\alpha_n \approx \alpha_{1,n} \approx \alpha_{2,n}$. Here the amplitude attenuation gets twice as large but the phase shift vanishes because of $\phi_{1,n} \approx \phi_{2,n}$. While the phase shift cannot be extracted, the sensitivity for absorption is higher in this configuration.

Recipe for choosing a value of difference in repetition frequency

There is an optimum value of difference in repetition frequency δf for an efficient data sampling. Here we discuss how one can choose such value. We assume the frequency combs which spectral spans are both ΔF with repetition frequency $f + \delta f$ and f . Therefore the frequency of the cross-correlation-like optical sampling of the dual-comb scheme is f . Due to the Nyquist-Shannon sampling theorem, the free spectral range of the optical sampling

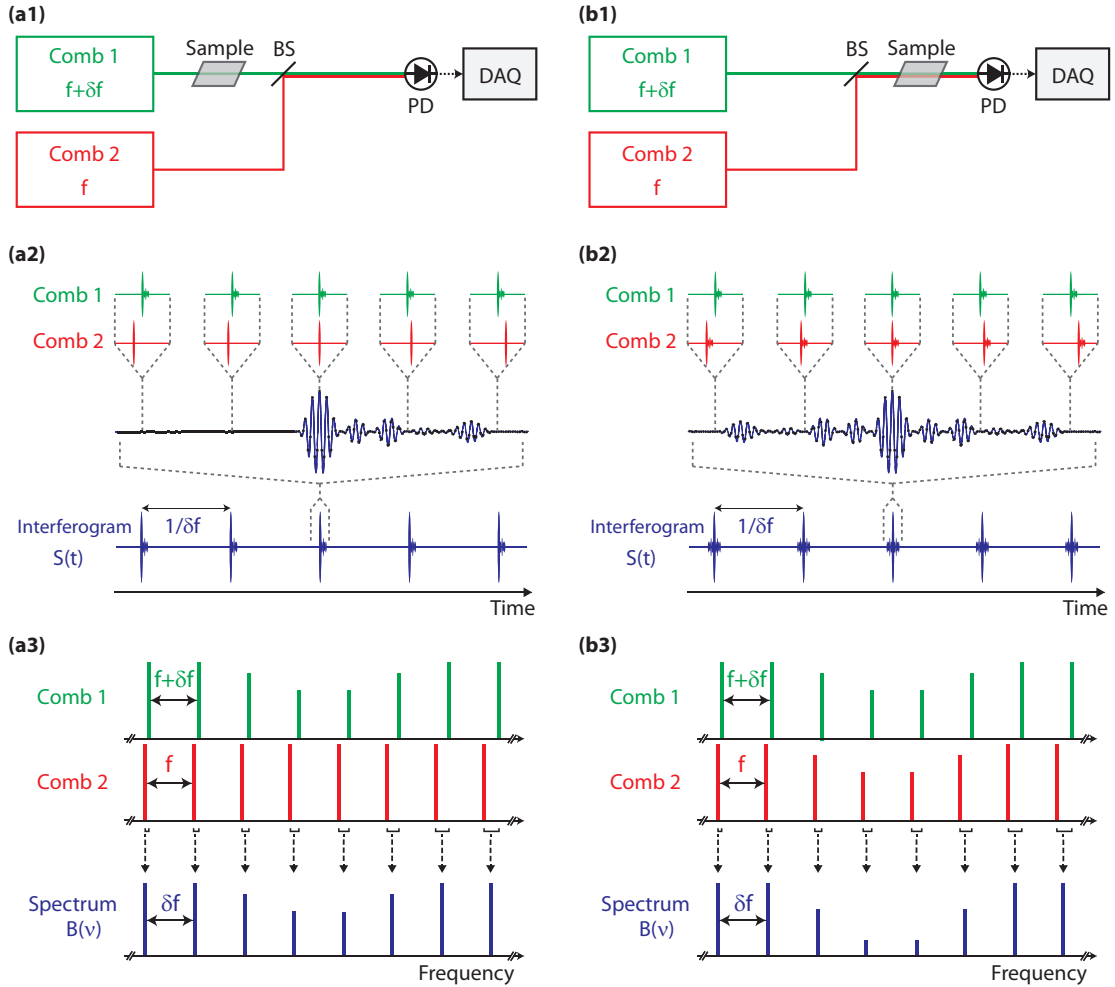


Figure 2.4: Molecular dual-comb spectroscopy in the configuration that (a) a single comb interacts with the sample, (b) both combs interact with the sample. (a1)(a2): configuration of the setup. (a2)(b2): time domain picture. (a3)(b3): frequency domain picture.

covers from 0 to $f/2$ in the frequency domain. We assume the electronic sampling frequency of the data acquisition is higher than the optical sampling frequency f , so that one can make sure the limitation of the free spectral range is set by the optical sampling ($0 - f/2$). Since the measurement speed of the dual-comb scheme is proportional to the difference in repetition frequency δf , one wants to choose a value as large as possible for an efficient sampling. As the down-converted spectrum has a bandwidth of $\Delta F \delta f / f$, a larger δf leads to a larger spectral span. If the down-converted dual-comb spectrum does not fit inside the free spectral range, undesired aliasing occurs by the sampling. To avoid the aliasing,

one must obey the condition:

$$\begin{aligned}\Delta F \times \frac{\delta f}{f} &\leq \frac{f}{2} \\ \delta f &\leq \frac{f^2}{2\Delta F}\end{aligned}\quad (2.20)$$

At best, $\delta f = \frac{f^2}{2\Delta F}$ where the down-converted spectrum spans 0 - $f/2$. Assuming, for example, $\Delta F=10$ THz and $f=100$ MHz, the difference in repetition frequency must obey $\delta f \leq 500$ Hz. Note that, in order to put the down-converted spectrum in the free spectral range, one has to adjust position of the spectrum by choosing a proper difference in offset frequency δf_0 .

Measurement time and spectral resolution

As shown above, dual-comb spectroscopy conducts cross-correlation-like optical sampling with pulse trains emitted from two frequency combs which repetition frequencies are f and $f + \delta f$. If one samples N pulse pairs within a measurement, The measurement time T_{lab} in the laboratory time-scale may be written:

$$T_{lab} = \frac{N}{f} \quad (2.21)$$

Since the optical sampling step from pulse pair to pulse pair is $\delta f/f^2$, the sampling time T_{eff} in the effective time-scale may be written:

$$T_{eff} = N \frac{\delta f}{f^2} = T_{lab} \frac{\delta f}{f} \quad (2.22)$$

This shows that the interferogram observed in the laboratory is stretched out in time by $f/\delta f$ from that in the effective time.

The spectral resolution in the lab-time scale $\delta\nu_{rf}$ may be written:

$$\delta\nu_{rf} = \frac{F_{ap}}{T_{lab}} = \frac{F_{ap}f}{N} \quad (2.23)$$

where F_{ap} is an apodization factor of a window function at Fourier transform (e.g. 1.77 for the triangular function etc.). The spectral resolution in the effective time-scale $\delta\nu_{opt}$ may be written:

$$\delta\nu_{opt} = \frac{F_{ap}}{T_{eff}} = \frac{F_{ap}}{T_{lab}} \frac{f}{\delta f} = \delta\nu_{rf} \frac{f}{\delta f} \quad (2.24)$$

2.2.3 Brief review of literature on dual-comb spectroscopy

The use of two frequency combs of slightly different repetition frequencies as an asynchronous sampling interferometer without moving parts was first demonstrated in 2001 [35]. This demonstration was intended for rapid scan optical coherence tomography (OCT). The theoretical proposal of dual-comb spectroscopy was published in 2002 [36]. In this article, a methodology how to extract the spectral features of sample was discussed in terminology of frequency comb. The first proof-of-principle of dual-comb spectroscopy was demonstrated with mid-infrared free-running combs generated by optical rectification in GaSe pumped by TiSa mode-locked lasers in 2004 [37]. Mid-infrared spectra in $750\text{-}1300\text{ cm}^{-1}$ were measured within $100\text{ }\mu\text{s}$. The group lead by Fritz Keilmann implemented a technique to improve the duty cycle of the measurement and demonstrated real-time recording of chemical vapor fluctuations from 22 m away with a rate of 950 spectra/s [38]. They also demonstrated near-field optical scanning microscopy (SNOM) with the mid-infrared system [39].

In 2008, stabilized frequency combs were utilized for dual-comb spectroscopy and the demonstration showed convincing quality of spectra for precise molecular spectroscopy by taking advantage of the precision capability of frequency combs [21]. The group lead by Nathan R. Newbury stabilized two Er-doped fiber combs to two continuous-wave lasers: one is a Hz-level linewidth continuous-wave laser stabilized to an ultrastable reference cavity, and the other is stabilized to a self-referenced frequency comb. Absorption and dispersion spectra of a molecular gas were measured over 3 nm bandwidth with a tunable optical filter. Such measurements with narrow bandwidth were repeated many times with tuning the spectral region over 15.5 THz with $155\text{ }000$ frequency elements with resolution of 100 MHz . With fully stabilized combs², they investigated molecular free-induction decay [40], and details of the system in terms of signal-to-noise ratio [41, 42]. The group has expanded the frequency range by spectral broadening with highly nonlinear fibers for accurate near-infrared spectroscopy [43, 44]. They also expand their stabilized system to mid-infrared region by difference frequency generation with a continuous wave laser [45].

Dual-comb spectroscopy was combined with cavity enhanced spectroscopy in 2010 [46, 47]. A broadband comb was injected to an external cavity resonant to the frequency comb. With careful intracavity dispersion management, each comb line over broad spectral span was enhanced in the cavity. Filling a gas sample in the enhancement cavity increases the effective interaction length so that sensitivity was drastically increased, while dual-comb spectroscopy provides short measurement times.

²Two continuous-wave lasers are stabilized to an ultrastable reference cavity.

Remote gas sensing with the dual-comb spectroscopy was also demonstrated [38, 48].

A posteriori interferometric-phase-error correction technique was demonstrated by post data processing [49–51]. In this technique, the comb fluctuations were measured at the same time as the dual-comb interferogram, and the phase errors were corrected by post data processing with the measured comb fluctuations. In this thesis, another approach is investigated, which is so called adaptive sampling technique [52, 53] (Chapter.3). In this technique, all the phase error correction is made by analog electronic processing so that no stabilization nor a posteriori correction is needed.

About the frequency range, most of demonstrations have been conducted in near-infrared region where frequency combs are readily available, but several demonstrations have been reported in the visible [52] (Chapter.3), mid-infrared [37–39, 45, 46, 54], and THz [55–58] region.

Recently, nonlinear dual-comb spectroscopy, which is pioneered by the work in this thesis, has been investigated with coherent Raman scattering [59, 60] (Chapter.5, Chapter.6), two-photon excitation [61, 62], and saturated absorption [63].

The dual-comb scheme have been applied to other fields apart from molecular spectroscopy, e.g. coherent LIDAR [25, 48, 64], optical time-frequency transfer [23], fast calibration of continuous-wave laser spectroscopy [28], whispering gallery mode sensing [65], and static fiber-Bragg-grating (FBG) strain sensor [66].

Challenges of dual-comb spectroscopy

At the time when the work of this thesis began, there were several challenges associated with dual-comb spectroscopy to be addressed.

The first unsolved fundamental issue was the spectral distortion due to the laser instability which prevented real-time measurements. Since the measurement time-scale of the dual-comb spectroscopy is microseconds to milliseconds, high frequency instability of the combs, which is not a trivial issue to eliminate, leads to missampling of the interferogram. One solution for the issue was stabilizing the combs with state-of-the-art technology in the best precision measurement laboratory [21]. But even the tightly stabilized combs might still have residual fluctuations which required averaging to clear up the distortion. The averaging, however, lost the real-time capability which is one of the unique capability of the dual-comb spectroscopy. Another solution was a posteriori correction of the fluctuations by post computational data processing [49, 50]. The method required additional computational time to correct the sampling errors and lost real-time capability as well. The work in this thesis addresses this issue and achieves real-time dual-comb spectroscopy by a new scheme called “Adaptive sampling”, which does not require neither stabilization of the combs nor post computational data processing (Chapter.3).

Another challenge was accessing molecular fundamental vibrations by dual-comb scheme. Due to the poor stability and narrow spectral bandwidth of existing mid-infrared frequency combs, demonstrations of linear absorption mid-infrared dual-comb spectroscopy did not show convincing quality of absorption spectra [37–39,46]. In the work of this thesis (Chapter.4), a broadband mid-infrared frequency comb is developed toward high quality linear absorption dual-comb spectroscopy.

As frequency combs emit intense ultrashort pulses, nonlinear interactions with the sample may be harnessed. Before the work of this thesis, however, none of experiments had investigated the potential of nonlinear dual-comb spectroscopy. In the part.II, we pioneer the field of nonlinear dual-comb spectroscopy and show its potential.

Part I

Linear dual-comb spectroscopy

Chapter 3

Adaptive dual-comb spectroscopy

Dual-comb spectroscopy has an important potential for rapid measurements of broadband molecular spectra, but its development has been hindered by demanding stability requirements of the optical frequency combs. We overcome the difficulty with a straightforward way which compensates the laser instabilities by electronic signal processing only. This new technique only uses free-running lasers without any phase-lock stabilization of the lasers nor post data processing, and drastically simplifies dual-comb spectroscopy. The demonstration of the technique shows that the quality of Doppler-limited molecular spectra is suitable for concentration measurements. The new technique of adaptive dual-comb spectroscopy offers a powerful transdisciplinary instrument for analytical sciences.

3.1 Background

Dual-comb spectroscopy has been demonstrated with a variety of laser sources (Section.2.2.3) and the spectroscopic method is now recognized for its capabilities of broadband, high speed, high resolution, and high accuracy. Indeed, the technique holds capabilities which surpasses conventional Fourier transform spectrometers, however in practice, the simplicity has been hindered by state of the art frequency comb stabilization technique which is only achievable in the best optical metrology laboratory. In many of previous demonstrations except for the highly stabilized dual-comb systems, quality of molecular spectra is much worse than those measured by the conventional Fourier transform spectrometers. These spectra have strong distortions which are not acceptable for quantitative spectroscopic applications. These distortions result from timing and phase fluctuations of frequency

The contents in this chapter is published in [52, 53]

combs. This quality degradation of spectra shares the same principle as a phenomenon known as interferometric phase error in the field of Fourier transform spectroscopy [67]. In a case of Michelson Fourier transform spectrometer, missampling of an interferogram due to position errors of a moving mirror leads to distortion of the interferogram. This distortion in the interferogram results in a chromatically distorted spectrum by Fourier transformation. The spectral distortion hampers precise analysis of lineshape or intensity of the spectrum. In general, position errors of the moving mirror by scale of nanometers leads to such distortions.

3.1.1 Stability requirements of combs in dual-comb spectroscopy

Dual-comb spectroscopy can be considered with a metaphor of a sampling oscilloscope. Pulses from comb 1 excite molecular free induction decay and pulses from comb 2 sample the waveform of this decay interferometrically. For simplicity, we at first ignore carrier-envelope phase shifts. At best, interferometric samples are taken at intervals $1/f$ (e.g. 10^{-8} s) where f is the repetition frequency of comb 2 (e.g. 100 MHz). If δf is the difference of comb repetition frequencies (e.g. 100 Hz), consecutive interferometric samples result from pulse pairs showing a time separation increased by an amount $\delta\tau = \delta f/f^2$ (e.g. 10^{-14} s). The “sampling oscilloscope” thus effectively stretches the waveform of the free induction decay signal by a factor $s = f/\delta f$ (e.g. 10^6). Signal frequencies in this waveform are transformed down from the optical to the radio-frequency region by the same factor s . In the experiment, the signal of the photodetector is electronically low-pass filtered in order to suppress the pulse repetition frequency f . The time-stretched waveform appears thus as a continuous electronic signal. This signal is digitized at a constant clock rate determined by the data acquisition board of the computer. For ideally stable frequency combs, the waveform thus sampled can be Fourier-transformed to reveal the signal spectrum. In the real world, major difficulties arise from the residual instabilities of the frequency combs, even when these benefit from state-of-the-art stabilization. The time intervals between excitation and sampling pulses are indeed subject to some variations δt , which appear in the detector signal stretched in time by the factor s . Let us now consider the slippage of the carrier phase relative to the pulse envelope due to laser dispersion. If the carrier-envelope slippage frequencies of the two combs differ by δf_0 , the relative phases of pump and probe pulse will change by an additional $2\pi\delta f_0/f$ between two interferometric samples, and all frequencies in the Fourier spectrum of the detector signal will be translated by δf_0 . As long as δf_0 is constant, the spectral translation can be accounted for if δf_0 is measured or

if the absolute frequency of some spectral feature is known.

In the frequency domain, dual-comb spectroscopy can be understood by considering the two frequency combs of slightly differing line spacing. The optical frequencies f_n of a laser frequency comb may be written $f_n = nf + f_0$, where n is a large integer and f_0 is the carrier-envelope offset frequency. Each pair of optical lines, one from each comb, produces a radio frequency beat note on the detector. These beat signals form a comb of radio frequencies $f_{n,rf} = n\delta f + \delta f_0$. Optical frequencies are thus converted into radio frequencies with a conversion factor $\delta f/f$. The beat note between one pair of lines from the two combs must therefore be kept narrower than δf to preserve the resolution. Furthermore, for coherent measurement, the intrinsic linewidth of the beat note should be narrower than the inverse of the acquisition time. In other words, dual-comb spectroscopy requires interferometric short-term stability and the intrinsic noise of a radio-frequency locked comb is significantly too high on times shorter than a millisecond [68] to allow for correct measurements. To record a distortion-free real-time interferogram, the jitters between subsequent pulses must be kept lower than 10 attoseconds. Otherwise, chromatic artifacts (phase errors) spoil the spectrum [67] and cannot be accounted for a posteriori.

These stability requirements are much more demanding than those for optical frequency metrology. There, it is common practice to reference the comb to a stable microwave clock. Relatively slow servo loops of some kHz bandwidth are used to compensate for drifts of the pulse repetition frequency and the carrier-envelope-offset frequency relative, and for shorter time scales, one relies on the intrinsic “flywheel” stability of the laser [69]. Even though the width of the comb lines remains typically on the order of 0.1 to 1 MHz under these circumstances, the effect of such short-term fluctuations becomes negligible for optical frequency measurements when averaging over times of seconds or minutes. Locking the comb to optical references makes it possible to achieve much narrower linewidths, but sub-Hz linewidth continuous-wave laser and fast feedback loop development require significant efforts that are not compatible with an easy-to-operate instrument. As a consequence, real-time dual-comb spectroscopy allowing for distortion-free spectra of good quality Doppler-broadened line profiles remains challenging.

Free-running or radio-frequency locked combs yield artifacts and reduced signal-to-noise ratio [37, 46, 54, 70, 71]. Stabilizing the combs against state-of-the-art cavity-stabilized continuous-wave lasers with a hertz-level linewidth, far exceeding the stability available from common microwave oscillators, enables to record high-quality interferograms averaged over several seconds or minutes [21, 41, 44, 45]. Such reports focused on long integration

time for signal-to-noise ratio improvement and highly resolved comb lines. Possible phase errors in ms-time scale acquisitions might be thus cleaned up. However this demanding approach can hardly be implemented outside the best frequency metrology laboratories. Alternatively, simultaneously recording the interferometric signal and the fluctuations of two loosely-stabilized combs against two continuous-wave lasers to compute a posteriori corrections has been demonstrated [50, 51]. This solution, with multiple data acquisition channels and computational treatment, also prevents fast acquisition rates.

3.2 Stability characterization of the free-running femtosecond lasers

We have investigated the frequency stability of our free-running femtosecond lasers to characterize the instabilities we need to compensate for. The repetition frequency of each laser is measured with a frequency counter referenced to the 10 MHz signal of a hydrogen maser. The drift is nearly linear and amounts for about 7 mHz per second. Such drifts are mostly due to thermal fluctuations and are easy to suppress with a low-bandwidth feedback loop. The instability of an optical comb line is measured by an optical beat measurement with a continuous-wave erbium-doped fiber laser. The continuous-wave erbium-doped fiber laser is emitting at 6483 cm^{-1} (1542.5 nm) and is stabilized against an ultra-low-expansion Fabry-Perot high finesse resonator. It has a line-width of 1.5 Hz in a 1 Hz bandwidth and thermal drifts of its central position of 20 mHz/s [22]. Figure.3.1 shows the beat notes at 460 μs (Figure.3.1a) and 1.3 s (Figure.3.1b) measurement times. Their linewidths are about 60 kHz and 260 kHz, respectively. For longer times, the beat measurement drifts linearly by 6 kHz/s. As the linewidth and drift of the cw laser are negligible compared to these values, we can infer that we directly measure the width and instability of one optical comb line. The measured short-term comb linewidths are significantly too broad to achieve Doppler-limited dual-comb measurements in which the beat notes between pairs of comb lines should be narrower than a few hundreds of Hertz.

3.3 Adaptive sampling with a single adaptive signal

Dual-comb spectroscopy requires demanding timing and phase stability. Adaptive sampling is a technique to automatically compensates the undesired interferometric phase errors

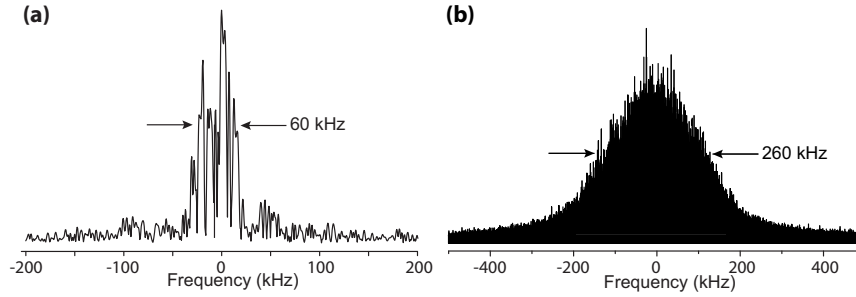


Figure 3.1: Fourier transform of the beating signal between one comb line and a stabilized Hz-linewidth continuous wave laser. (a) Over $467 \mu\text{s}$, the time required for the acquisition of an interferogram, the width of the comb line is of the order of 60 kHz. This is much broader than radio-frequency comb line spacing (344.9 Hz). (b) Over 1.3 s, the width of the comb line increases to 260 kHz. The spectra are displayed on a linear intensity scale.

by analog electronic processing. In this section, we show that concept of the adaptive sampling surely works and effectively compensates the phase errors by implementing a simple scheme with a single adaptive signal. With the single adaptive signal, however, one cannot fully compensate the phase errors because a frequency comb has two degrees of freedom, repetition frequency and carrier envelope offset frequency. We introduce a full compensation scheme in the following section (Section.3.4).

3.3.1 Principle

Compensation for timing variations can be achieved by triggering data acquisition with a single adaptive clock signal. Such a signal, which automatically provides the needed correction at a single optical frequency, can be derived from the radio-frequency beat note between two comb lines. The filtered beat note signal with a frequency f_a can be considered as a time-stretched sampled waveform of an optical comb line. Any timing variation δt will shift the beat signal by the stretched amount $s\delta t$. If the pulses were only subject to such timing variations, all frequencies in the spectrum would benefit equally from the produced correction signal. However frequency combs can also produce random variations $\delta\phi$ of the phase difference between pump and probe pulse. These phase variations $\delta\phi$ are directly imprinted onto each frequency component of the detected signal, and they can only be corrected to lowest order by a timing change of the clock signal. A timing change δt gives a frequency-dependent phase correction $2\pi f_a \delta t$, whereas we would need to correct for a frequency-independent phase shift $\delta\phi$.

3.3.2 Mathematical description

The electric field of the frequency comb $E_j(t)$ ($j=1,2$) may be written:

$$E_j(t) = A_j(t) \exp\{-i2\pi(f_{c_j}t + \phi_j)\} \quad (3.1)$$

where $A_i(t)$ is the pulse-envelope function of the frequency comb, f_{c_j} is the carrier frequency and ϕ_j is the phase of the carrier-wave. The photodetector sees optical intensity of the combined field of the two frequency combs ($E_1(t) + E_2(t)$):

$$I(t) = |E_1(t) + E_2(t)|^2 \quad (3.2)$$

The interferogram is written:

$$\begin{aligned} S(t) &= E_1(t)E_2^*(t) + c.c. \\ &= B(t) \exp\{-i2\pi(\Delta f_c t + \Delta\phi)\} + c.c. \end{aligned} \quad (3.3)$$

where $B(t) = A_1(t)A_2^*(t)$, $\Delta f_c = f_{c_1} - f_{c_2}$ and $\Delta\phi = \phi_1 - \phi_2$. Here, we introduce the relative timing jitter $\delta t(t)$ and relative phase jitter $\delta\phi(t)$ of the pulse pairs due to the instability of the combs, then the interferogram $S_d(t)$ may be written:

$$S_d(t) = B\{t + \delta t(t)\} \exp[-i2\pi\{\Delta f_c(t + \delta t(t)) + \Delta\phi + \delta\phi(t)\}] + c.c. \quad (3.4)$$

An adaptive signal is a single beat note between comb 1 and comb 2, which may be written:

$$AS_a(t) = B_a \exp[-i2\pi\{f_a(t + \delta t(t)) + \Delta\phi + \delta\phi(t)\}] + c.c. \quad (3.5)$$

where B_a is the amplitude of the adaptive signal which is approximately constant in time, and f_a is the frequency of the adaptive signal. If one uses zero-crossing points of the adaptive signal as a sampling clock, the sampling time τ_N obeys:

$$f_a(\tau_N + \delta t(\tau_N)) + \Delta\phi + \delta\phi(\tau_N) = N \quad (3.6)$$

where $N (= 0,1,2,\dots)$ is the sampling points number. With this sampling clock, however, the timing and phase jitters are perfectly compensated for at the frequency f_a only.

Aliasing

Since the frequency of the adaptive signal f_a lies in the middle of the radio frequency spectrum, it is not high enough as a sampling frequency to avoid aliasing. In order to avoid the aliasing, one can multiply the adaptive signal to the value above twice as the maximum frequency of the spectrum to be observed.

3.3.3 Experimental setup

The experimental setup (Figure.3.2) is placed in a basic laboratory environment, without air-conditioning system, vibration isolation, or dust protection. Two free-running commercial femtosecond erbium-doped fiber lasers emitting in the 6452 cm^{-1} (1550 nm) region with slightly different repetition frequencies have two fibered output ports. For each of the femtosecond lasers, the port that emits an average power of about 20 mW is used for the dual-comb interferometric setup. The two beams are combined to interrogate the sample and beat on a fast InGaAs photodiode. The time-domain interferometric signal exhibits a periodic succession of huge bursts every $1/\delta f$ when femtosecond pulses from the two lasers coincide. A low-pass filter essentially suppresses the unmodulated part of the interferogram. This part consists of pulses generated at a repetition frequency of 100 MHz by the two lasers. In order to synchronize the interferometric signal with the adaptive clock, one has to compensate for the delays induced by the different optical paths and the various electronic components. An electronic delay line is therefore inserted in the interferometric signal path. A low-noise 100 MHz bandwidth amplifier with variable gain scales the filtered detector signal to the full range of a 16-bit analog-to-digital converter. This high-resolution digitizer, onboard a personal computer, has 65 MHz-bandwidth and sampling rate capabilities of up to 180 MSamples/s. It is externally synchronized with the adaptive clock described below.

Adaptive signal generation

The second output port of the femtosecond lasers serves to generate the adaptive clock signal. Each laser beats with a free-running continuous-wave erbium-doped fiber laser that emits at 6519 cm^{-1} (1534 nm). One line of each of the two femtosecond lasers is isolated by beating each comb with the continuous-wave laser emitting at a frequency f_{cw} , thus producing two beat notes $f_{cw} - f_{1,n}$ and $f_{cw} - f_{2,n}$, around 60 and 80 MHz, respectively. The electric signals are filtered and a delay line adjusts the timing between the two beat signals. The two beat notes are electronically mixed so that the contribution of the continuous-wave laser cancels to generate the signal $f_a = f_{1,n} - f_{2,n}$ around 20 MHz. As the radio-frequency spectrum spans the free spectral range $0 - f/2$, i.e 0-50 MHz, the 20 MHz signal does not have a frequency high enough to avoid aliasing. Therefore it is frequency-multiplied by five and the resulting 100 MHz provides the adaptive clock signal that is connected to the external clock input of the digitizing data acquisition board.

lasers without the adaptive sampling scheme do not allow for dual-comb spectroscopic measurements. The quality of our present results also far exceeds what is obtained with the commercially available servo-controlled comb systems developed for frequency metrology.

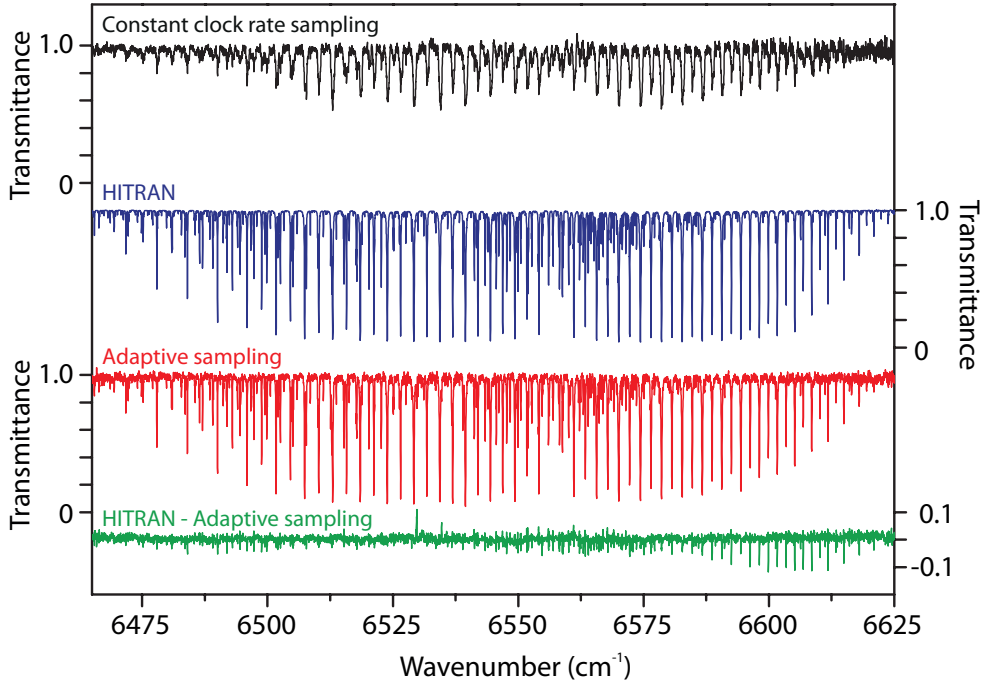


Figure 3.3: Illustration of the quality of the adaptive sampling spectra. Experimental absorption spectra of $^{12}\text{C}_2\text{H}_2$ and $^{12}\text{C}^{13}\text{CH}_2$ sampled at adaptive and constant clock rates, respectively, are compared to a spectrum computed from the line parameters available in the HITRAN database [72]. Both experimental spectra are measured with free-running fs lasers in identical conditions except for the data acquisition clock. The difference in repetition frequencies between the two free-running fs lasers is set to 447.5 Hz. Six consecutive spectra with an apodized resolution of 0.033 cm^{-1} (1 GHz), each measured within $396\text{ }\mu\text{s}$, are averaged, resulting in a total measurement time of 2.38 ms and a total experimental time of 13.4 ms. The agreement of the experimental adaptive spectrum with the HITRAN data confirms the suitability of our technique for measurements with Doppler-limited resolution. When sampled at the constant clock rate of the digitizing data acquisition board, the spectrum is strongly distorted due to the relative fluctuations of the repetition frequency and carrier envelope phase slips of the fs lasers. This lowers the sensitivity and scrambles the spectral features.

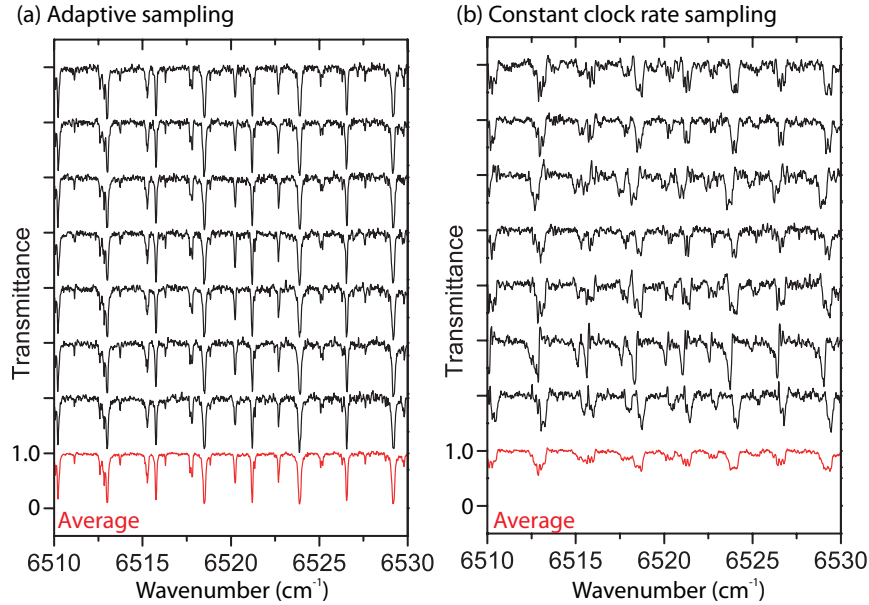


Figure 3.4: Portions of experimental and computed spectra of acetylene. (a) Zoom of a span of 20 cm^{-1} of seven consecutive adaptive individual spectra and their average. (b) Spectra digitized at the constant clock rate of the data acquisition board and identical conditions than in (a) otherwise. The acetylene line profiles are strongly distorted and the drifts in the frequency scale do not allow for averaging.

Residual phase error

The scheme with a single adaptive signal perfectly compensates for the fluctuations of the femtosecond lasers at a given optical frequency only. Apart from this frequency, the amount of phase error increases. In order to visualize the residual phase error over the entire spectral range of the lasers, a Fabry-Pérot spectrum was measured with the same setup (Figure.3.5). The Fabry-Pérot interferometer consists of two mirrors which free spectral range is 2 cm^{-1} (60 GHz) and the finesse 90. The spectrum clearly shows that the phase error increases from the frequency where the phase error is perfectly compensated. Combs where the carrier-envelope offset cancels, producible by difference frequency generation [37, 73], would allow for an unlimited correction. The femtosecond lasers that we used are unmodified commercial sources. Proper design of the oscillators to minimize the pulse-to-pulse phase shift, e.g. with low-noise pumping diodes, would certainly improve the present results.

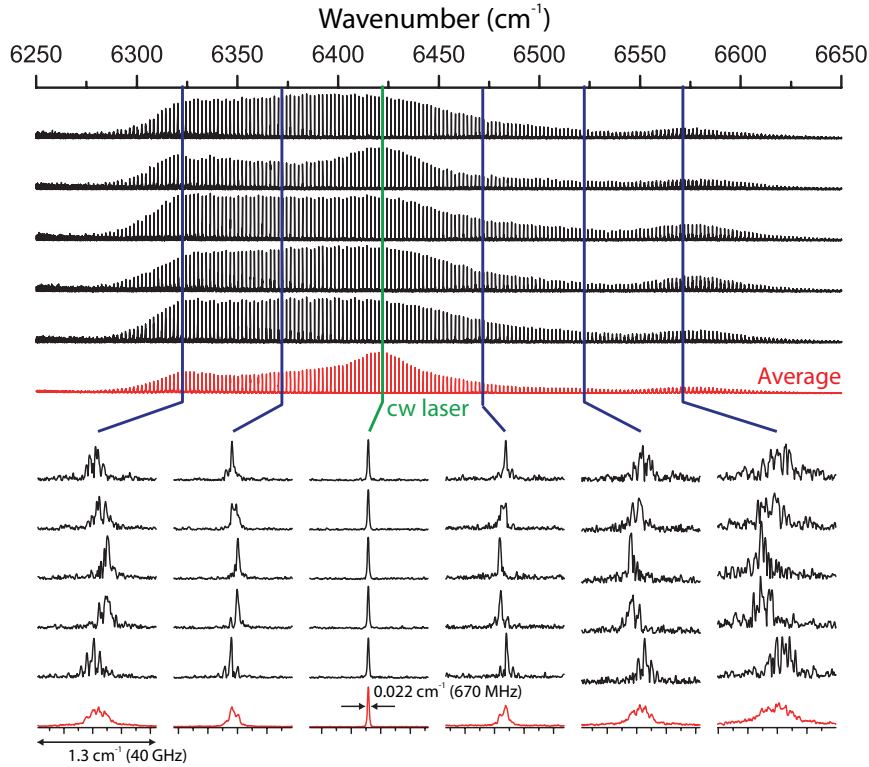


Figure 3.5: Fabry-Pérot spectrum measured with the adaptive sampling. Wavenumber of a continuous-wave laser to make the adaptive clock is 6423 cm^{-1} (1557 nm). Free spectral range of the Fabry-Perót interferometer is 2 cm^{-1} (60 GHz) with the finesse 90.

3.4 Adaptive dual-comb spectroscopy with two adaptive signals

Phase error correction by the adaptive sampling with an adaptive signal shows good quality spectrum around a certain optical frequency only. Here we introduce a second adaptive signal and shows full compensation of phase errors.

3.4.1 Principle

Adaptive dual-comb spectroscopy enables real-time compensation for the timing fluctuations and carrier-envelope phase shift variations by automatically triggering the data acquisition and correcting the interferometric signal with two adaptive signals. These signals are derived from two radio-frequency beat notes f_a and f_b originating from different pairs of individual lines of the two different combs. Each filtered beat note signal can be consid-

ered as a time-stretched sampled waveform of an optical comb line. Any relative timing variation δt shifts the interferometric signal by the stretched amount $s\delta t$. If such a time shifted beat note is used as a clock signal to trigger the data acquisition, it would correct for timing fluctuations automatically if the pulses were only subject to timing variations. However, frequency combs also produce unintended variations $\delta\phi$ of the phase difference between pump and probe pulse. These phase variations $\delta\phi$ are directly imprinted onto each frequency component of the detected signal. In order to correct for such phase fluctuations, the signal of the sampling detector is multiplied electronically with the beat note signal at f_a . The difference frequency between the beat signals at f_a and f_b is immune to common phase variations $\delta\phi$ and can provide the required adaptive clock signal, which compensates for timing variations.

3.4.2 Mathematical description

Following the Subsection.3.3.2, now we use a second adaptive signal $AS_b(t)$:

$$AS_b(t) = B_b \exp[-i2\pi\{f_b(t + \delta t(t)) + \Delta\phi + \delta\phi(t)\}] + c.c. \quad (3.7)$$

where B_b is the amplitude of the adaptive signal which is approximately constant in time, and f_b is the frequency of the adaptive signal. In order to cancel the phase jitter $\delta\phi(t)$, complex conjugate of one of the adaptive signal ($AS_a^*(t)$) is multiplied to the interferogram $S_d(t)$:

$$\begin{aligned} S_{mix}(t) &= S_d(t)AS_a^*(t) \\ &\propto B\{t + \delta t(t)\}B_a^* \exp[-i2\pi(\Delta f_c - f_a)(t + \delta t(t))] + c.c. \end{aligned} \quad (3.8)$$

This operation, in practice, can be made by an electronic mixing and a low-pass filtering. The mixed interferogram $S_{mix}(t)$ does not have any term containing $\delta\phi(t)$ but timing fluctuation $\delta t(t)$. The timing jitter can be compensated by an adaptive sampling with a proper sampling clock which contains the same fluctuation as the interferogram. An electronic mixing of the two adaptive signals $AS_a(t)$ and $AS_b(t)$ generates such a clock signal:

$$\begin{aligned} AS_{clk}(t) &= AS_a(t)AS_b^*(t) \\ &= B_a B_b^* \exp[-i2\pi\{(f_a - f_b)(t + \delta t(t))\}] + c.c. \end{aligned} \quad (3.9)$$

which only contains the fluctuation due to $\delta t(t)$, which is the same situation as the mixed interferogram $S_{mix}(t)$. If one uses the zero-crossing points of the signal as a sampling clock,

the sampling timing τ_N obeys the equation:

$$(f_a - f_b)(t + \delta t(t)) = N \quad (3.10)$$

where $N (= 0,1,2,\dots)$ is the sampling points number.

Aliasing

The discussion above describes the principle of the adaptive dual-comb spectroscopy with two adaptive signals, but it contains two issues both related to aliasing. The first possible aliasing can occur at the multiplication for the phase jitter correction (Equation.3.8). Because the frequency of the adaptive signal f_a is in the middle of the down-converted spectrum, Fourier transform of the mixed interferogram $S_{mix}(t)$ leads to aliasing. In order to avoid that, one can produce a new adaptive signal $AS_A(t)$ by combining the two initial adaptive signals ($AS_a(t)$, $AS_b(t)$) to keep the dependence on $\delta\phi(t)$ but change the frequency:

$$\begin{aligned} AS_A(t) &= AS_a(t)^p \{AS_b(t)^{p-1}\}^* \\ &\propto \exp[-i2\pi\{(pf_a - (p-1)f_b)(t + \delta t(t)) + \Delta\phi + \delta\phi(t)\}] + c.c. \end{aligned} \quad (3.11)$$

where p is an integer.

The second possible aliasing can occur during sampling. Due to the sampling theorem the observable spectral span (free spectral range) is limited by half of the sampling frequency. One can easily expand the spectral span by using higher sampling frequency which, in practice, can be made by an electronic multiplication:

$$\begin{aligned} AS_B(t) &= \{AS_a(t)AS_b^*(t)\}^q \\ &\propto \exp[-i2\pi q\{f_a - f_b\}(t + \delta t(t))] + c.c. \end{aligned} \quad (3.12)$$

Accuracy of adaptive dual-comb spectroscopy with two adaptive signals

Since the adaptive sampling corrects all the possible phase errors pulse-pair by pulse-pair, if molecular induction decays do not last till next pulse comes to the sample, interaction between the pulse and the sample can be treated independently. In this situation, the adaptive sampling does not lose any accuracy if the correction is perfect. To put it in another way, absorption linewidth of the molecular sample is broader than the comb line spacing, the phase correction of the pulses works perfectly and makes an accurate down-converted spectrum. The absolute frequency accuracy relies on reference frequency e.g. positions of continuous-wave lasers or molecular absorption lines.

3.4.3 Experimental setup

The experimental condition and the basic setup builds on the one presented in the previous section (Section.3.3).

For generation of adaptive signals, each femtosecond laser independently beats with two free-running continuous-wave erbium-doped fiber laser that emit at 6519 cm^{-1} (1534 nm) and 6423 cm^{-1} (1557 nm), respectively (Figure.3.6). Two beat notes $f_{cw} - f_{1,n}$ (AS_a) and $f_{cw} - f_{2,n}$ (AS_b) are produced, thus isolating one line of each of the two femtosecond lasers. The electric signals are filtered and a delay line adjusts the timing between the two beat signals. The two beat notes are electronically mixed so that the contribution of the continuous-wave laser cancels to generate the signal AS_a with the frequency of $f_a = f_{1,n} - f_{2,n}$. In this manner, two beat notes between individual comb lines from the two combs are produced, with frequencies $f_a = f_{1,n} - f_{2,n}$ and $f_b = f_{1,m} - f_{2,m}$. In this experiment, their values are 30 and 20 MHz, respectively. Detail description of the adaptive signals generation is shown in Figure.3.7.

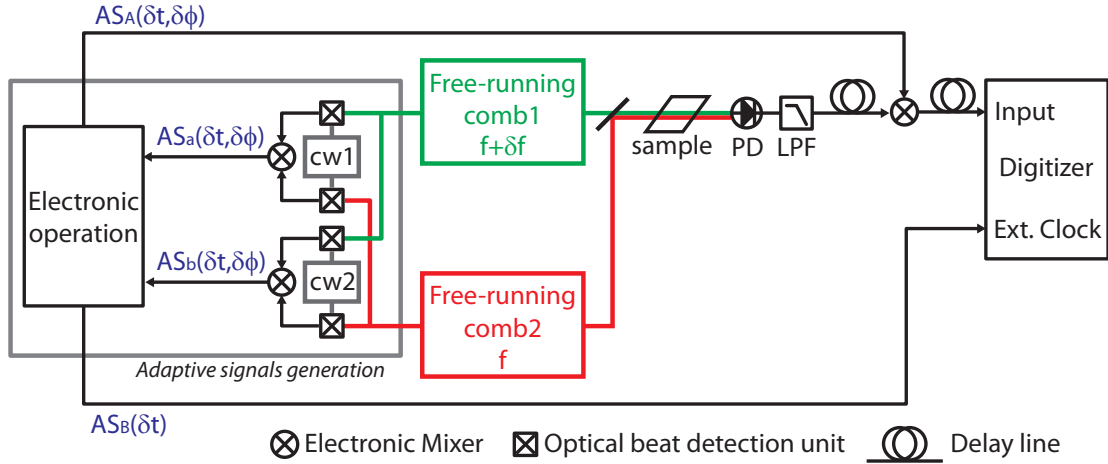


Figure 3.6: Experimental setup of the adaptive dual-comb spectroscopy with two adaptive signals. AS: adaptive signal. cw: continuous-wave laser. PD: photodiode. LPF: lowpass filter.

As the radio-frequency spectrum spans the free spectral range $0 - f/2$, i.e. 0-50 MHz, the signals at frequencies f_a and $f_a - f_b$ are not high enough to avoid aliasing. The first adaptive signal AS_A is fabricated from a signal at frequency $3f_a - 2f_b$ ($3AS_a - 2AS_b$) produced by a combination of frequency multipliers and mixers. The subsequent 50 MHz signal AS_A is mixed with the interferometric signal before digitalization by the data acquisition board. The second adaptive signal AS_B results from the frequency-multiplication by a factor ten of the beat signal at frequency $f_a - f_b$. A 100 MHz signal thus provides the adaptive clock

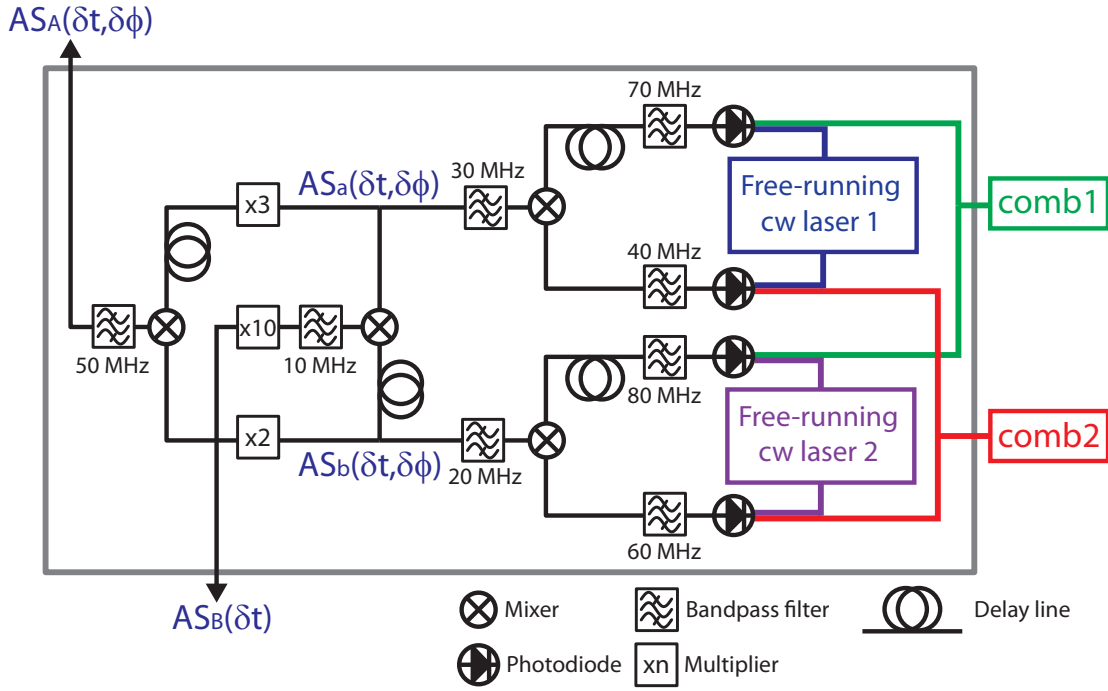


Figure 3.7: Detail of generation scheme of adaptive signals.

signal AS_B that is connected to the external clock input of the digitizing data acquisition board (14-bit, 65-MHz-bandwidth, up to 125 MSamples/s).

3.4.4 Results and discussion

The transmission spectrum by a 70-cm single-pass gas cell filled with 213 Pa of acetylene in natural abundance is recorded in the region of the $\nu_1 + \nu_3$ combination band. Figure.3.8 displays a 20 cm^{-1} zoomed part of a 480 cm^{-1} (14.5 THz) spectral span. Seven consecutive spectra are displayed. Each is measured within $467 \mu\text{s}$ with 0.037 cm^{-1} (1.1 GHz) apodized resolution at a refresh rate of 350 Hz. The reproducibility of consecutive adaptive spectra permits efficient averaging whereas free-running lasers without the adaptive sampling scheme produce strongly distorted spectra and do not allow for quantitative measurements or signal averaging. To make the excellent quality of the experimental adaptive spectra obvious, we compare (Figure.3.9, Figure.3.10) a spectrum resulting of 200 averaging with a spectrum computed from the HITRAN database [72]. The good signal-to-noise ratio in the experimental adaptive spectrum clearly reveals the rotational lines of the $\nu_1 + \nu_3$ cold band, the $\nu_1 + \nu_3 + \nu_4^1 - \nu_4^1$ and $\nu_1 + \nu_3 + \nu_5^1 - \nu_5^1$ hot bands of $^{12}\text{C}_2\text{H}_2$ and even of the $\nu_1 + \nu_3$ cold band of $^{12}\text{C}^{13}\text{CH}_2$ though its relative concentration is about a hundred times

smaller. The level of the residuals between the adaptive spectrum and the calculated one is below 1.5 %. Calibration against two molecular lines present in the adaptive spectrum sets the frequency accuracy on the other line positions to 0.00033 cm^{-1} (10 MHz) (relative accuracy: 5×10^{-8}) at 1 ms measurement time. The very good agreement between experimental and computed profiles shows the suitability of our technique for the measurement of line intensities or concentrations.

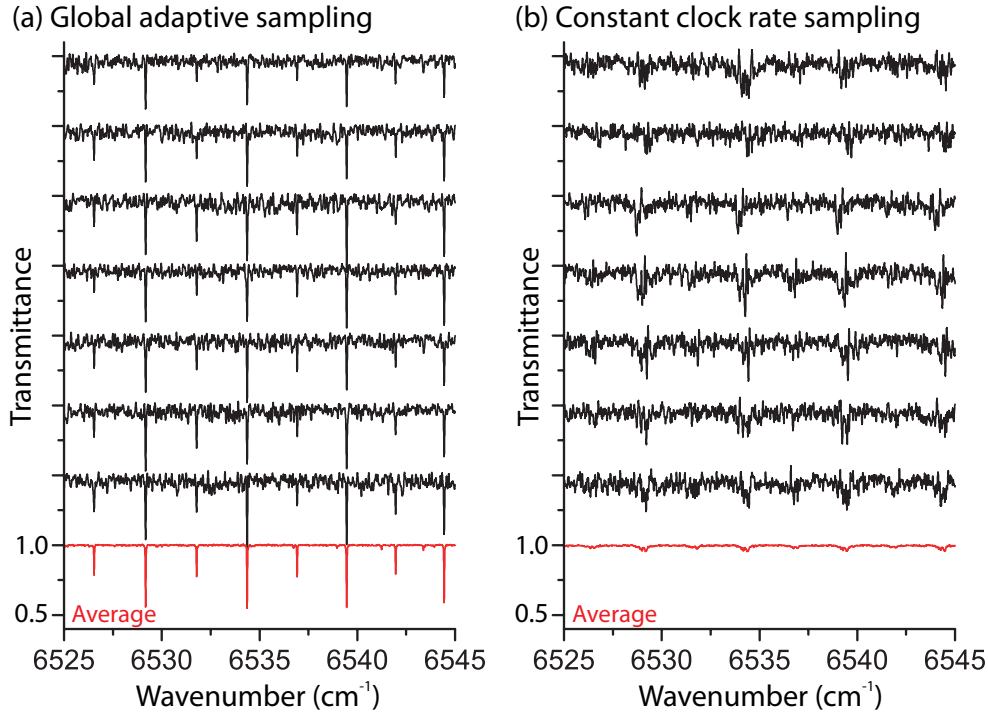


Figure 3.8: Portions of experimental and computed spectra of acetylene. (a) Zoom of a span of 20 cm^{-1} of seven consecutive adaptive individual spectra (in black) and the average of 200 spectra (in red). Each individual spectrum is measured over a 480 cm^{-1} span within $467 \mu\text{s}$. (b) Spectra digitized at the constant clock rate of the data acquisition board and identical conditions than in (a) otherwise. The acetylene line profiles are strongly distorted and the drifts in the frequency scale do not allow for averaging.

Rather than averaging over several spectra, one can reduce the difference of the laser repetition frequencies and record interferometric signals over a longer time period. In this way, it becomes possible to resolve the individual comb lines and to demonstrate that the coherence is maintained during the measurement time. Figure.3.11 shows a spectrum of acetylene spanning over 400 cm^{-1} (12 THz) recorded in 2.7 s with 268×10^6 samples. The 120,000 individual comb lines are resolved across the full spectral span and their

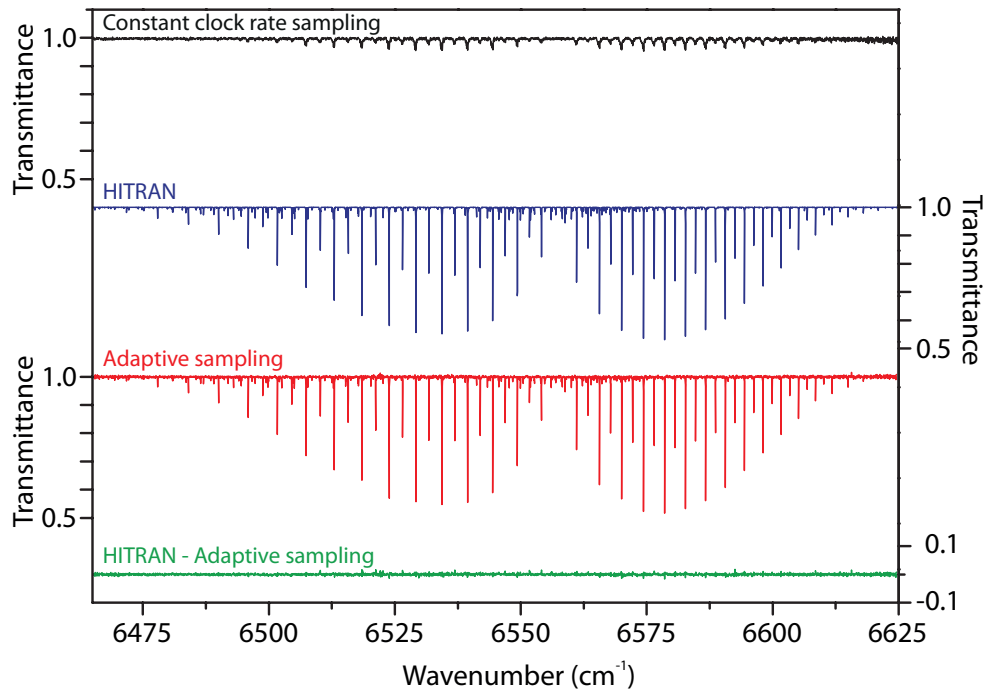


Figure 3.9: Illustration of the quality of the adaptive sampling spectra. Experimental absorption spectra of $^{12}\text{C}_2\text{H}_2$ and $^{12}\text{C}^{13}\text{CH}_2$ sampled at adaptive and constant clock rates, respectively, are compared to a spectrum computed from the line parameters available in the HITRAN database [72]. The 70 cm long cell is filled with 213 Pa of acetylene. Both experimental spectra are measured with free-running fs lasers in identical conditions except for the data acquisition clock. The difference in repetition frequencies between the two free-running fs lasers is set to 344.9 Hz. Two hundred consecutive spectra with an apodized resolution of 0.037 cm^{-1} (1.1 GHz), each measured within $467\text{ }\mu\text{s}$, are averaged, resulting in a total measurement time of 93 ms and a total experimental time of 580 ms. The agreement of the experimental adaptive spectrum with the computed spectrum from the $^{12}\text{C}_2\text{H}_2$ and $\text{H}^{12}\text{C}^{13}\text{CH}$ line parameters of the HITRAN database confirms the suitability of our technique for measurements with Doppler-limited resolution. When sampled at the constant clock rate of the digitizing data acquisition board, the spectrum is strongly distorted due to the relative fluctuations of the repetition frequency and carrier envelope phase slips of the fs lasers. This lowers the sensitivity and scrambles the spectral features.

apodized instrumental line-width is $6.7 \times 10^{-6}\text{ cm}^{-1}$ (202 kHz) in the optical domain (0.7 Hz in the radio-frequency domain). In comparison, a Michelson-based Fourier transform spectrometer would record a similar spectral domain, with 10^5 spectral elements and a resolution at best of the order of 0.0033 cm^{-1} (100 MHz), in several hours.

Our adaptive scheme sufficiently compensates for the short-term relative fluctuations of

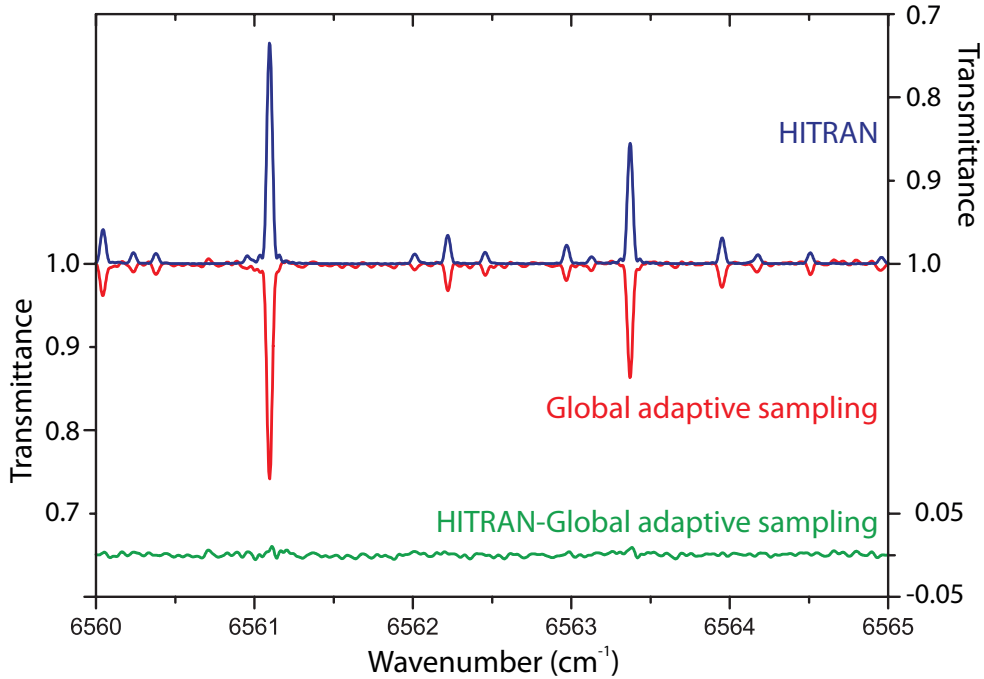


Figure 3.10: Zoom of a 5 cm^{-1} portion of the spectra shown in Figure.3.9. The adaptive experimental spectrum and the spectrum computed from the HITRAN data shown in Figure.3.9, together with the residuals, are expanded both in the x- and y-scales to give better appreciate the high resolution details.

the femtosecond lasers at any optical frequency. In this demonstration, all lasers are free-running but their relative coherence is reconstructed in real-time. In comparison to the width of molecular Doppler-broadened lines, the drift of the lasers is however negligible. We demonstrate that high-quality molecular spectra down to Doppler-limited resolution are recorded under such conditions. Importantly these spectra are fully suitable for line profile and line intensities measurements within a reasonable accuracy of about 5 %. Therefore, the instrument is suitable for optical diagnostics in a variety of applications. If absolute direct frequency calibration via the frequency combs or high accuracy in the measurements of narrow, e.g. sub-Doppler, line profiles is needed, the combs could be stabilized to a radio-frequency reference, as they often are in frequency metrology. This only avoids long-term drifts and enables self-calibration, but does not improve the quality of the individual spectra. The adaptive sampling scheme can still be applied to compensate for the laser short-term instabilities. Though radio-frequency locking of the combs alone is not a possible alternative for dual-comb spectroscopy, it would expand the range of applications of adaptive sampling to precision spectroscopy. The possibility of using commercial fem-

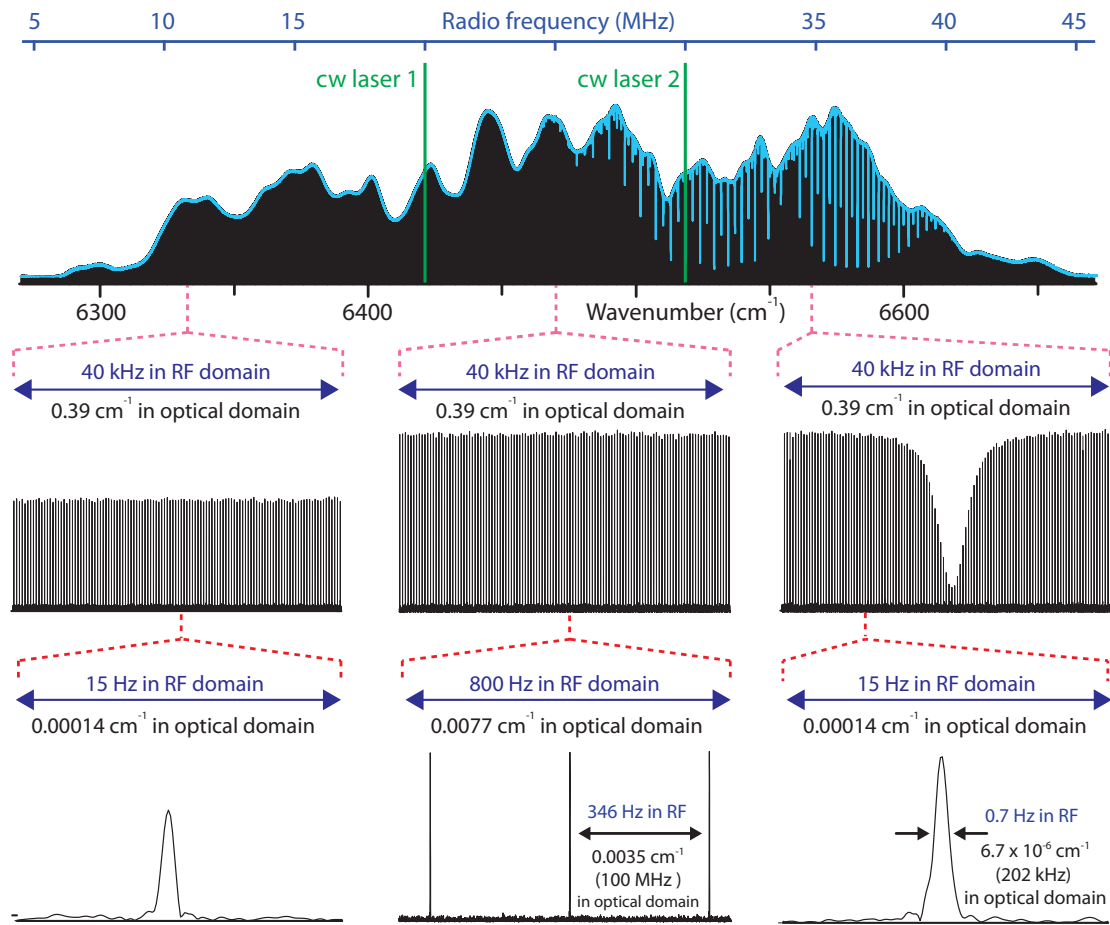


Figure 3.11: Adaptive spectrum spanning 400 cm^{-1} with resolved comb lines. The spectrum across the entire domain of emission of the erbium-doped fs fiber lasers exhibits 120,000 well-resolved individual comb lines. The measurement time is 2.7 s. It reveals several acetylene profiles shaping the discrete comb line intensities. The frequency of the continuous-wave lasers used in the production of the adaptive signals is indicated in green in the upper row of the figure. In the two lowest rows, different degrees of zooms in three different spectral regions well apart from these two frequencies isolate the individual comb lines and prove that the coherence between the two combs is maintained over the time of the measurement.

to second lasers or frequency comb systems without any sophisticated optical or electronic stabilization scheme considerably ease the implementation of a dual-comb spectrometer and should prompt new applications to real-time spectroscopy and sensing. The adaptive scheme and the averaging could also take advantage of digital sampling processors on-board the data acquisition system and would similarly bring suitable real-time processing, as demonstrated [51] after release of a preprint of the present work.

3.5 Adaptive dual-comb spectroscopy in the visible with nonlinear frequency conversion

The most convincing demonstrations of dual-comb spectroscopy have been undertaken in the near-infrared range, where frequency-comb oscillators are conveniently available. However, most of molecular transitions in this region are due to weak overtone bands. The visible region, where many molecules undergo strong rovibronic transitions, is complementary to the “molecular fingerprint” mid-infrared range. Moreover, advanced photonic technologies are readily available in this domain. However, dual-comb spectroscopy has not been implemented yet in the visible and ultraviolet regions. Here, we report on real-time dual-comb spectroscopy in the visible spectral region. Adaptive sampling makes it possible to record distortion-free dual-comb spectra with frequency-doubled free-running fs ytterbium-doped fiber laser systems. We investigate the dense rovibronic spectrum of iodine in the 19240 cm^{-1} region at Doppler-limited resolution.

Another important aspect of this experiment is that adaptive sampling in the frequency converted region works with the adaptive signal created in the fundamental frequency region of the lasers. This is especially important when spectroscopy is to be done in the extreme frequency such as VUV or XUV region where the generation of the adaptive signal is not easy.

3.5.1 Experimental setup

Figure.3.12 sketches the experimental setup. Two free-running Yb-doped fiber commercial mode-locked oscillators have a central wavenumber of 9620 cm^{-1} (1039.5 nm). They emit pulses of about 100 fs with an average power of 60 mW. Their repetition frequencies are about 100 MHz and they differ by 6.7 Hz. No active stabilization is used and the repetition frequencies are adjusted manually by tuning a piezo-electric actuator and a stepper motor changing the laser cavity lengths. The repetition frequencies drift quasi-linearly as a function of time with a slope of about 20 mHz/s. For the spectroscopy setup, the two laser beams are frequency-doubled with 2 mm-thick BBO (β -barium borate) crystals to generate a spectrum centered around 19360 cm^{-1} (516.5 nm). The average power of the frequency-doubled pulses is 3 mW. The beams are combined on a beam splitter and interrogate a 90 cm-long iodine cell at room temperature (vapor pressure: $\sim 40\text{ Pa}$). Their time-domain interference pattern is detected by a 250 MHz bandwidth Si

avalanche photodiode, filtered, amplified and digitized by a 16-bit data acquisition board synchronized by an adaptive clock.

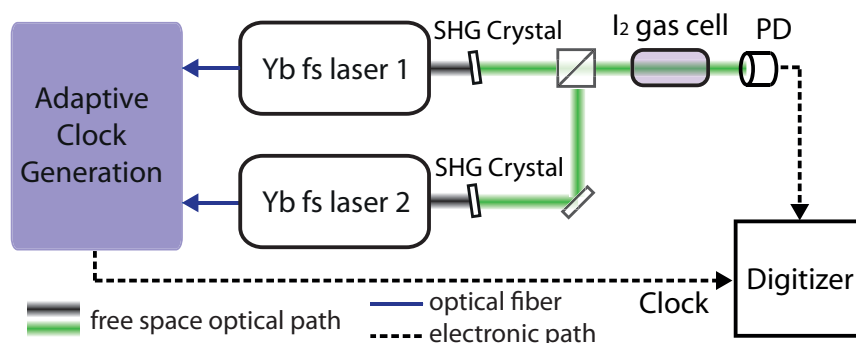


Figure 3.12: Experimental setup. Two free-running femtosecond Yb-doped fiber lasers with slightly different repetition frequencies are frequency-doubled with second-harmonic-generation (SHG) crystals and combined. The green beams probe the iodine sample. Their time-domain interference signal is recorded with a fast photodetector (PD) and digitized using the adaptive clock, described in Figure.3.13.

Figure.3.13 displays the details of the adaptive clock signal generation, represented by a box in Figure.3.12. Each of the two femtosecond ytterbium-doped fiber lasers beats with the same free-running narrow-linewidth continuous-wave (cw) ytterbium-doped fiber laser that emits at 9618 cm^{-1} (1039.7 nm). The beat notes between the femtosecond and cw lasers isolate, through proper electronic filtering, a single comb line of each comb. The two beating signals are then electronically mixed and the contribution of the cw laser vanishes. A signal at the frequency $f_1 - f_2 = 10.5 \text{ MHz}$ is thus produced. The timing and phase fluctuations between the interfering combs are directly imprinted onto this beating signal. Interference between pairs of optical comb lines image the optical absorption spectrum into the radio frequency region, ideally to cover the full free spectral range which is half of the repetition frequency of the fs lasers i.e. 50 MHz. Therefore, we frequency-multiply eight-fold the 10.5 MHz signal to avoid aliasing. The resulting $f_{clk} = 84 \text{ MHz}$ signal provides the adaptive clock signal that triggers the data acquisition. Not shown in the figures, the delays mostly induced by the various electronic components are compensated for. An electronic delay line is therefore inserted after the detector signal in the interferometric spectroscopy set-up and after one of the optical beat detection units in adaptive clock generation device.

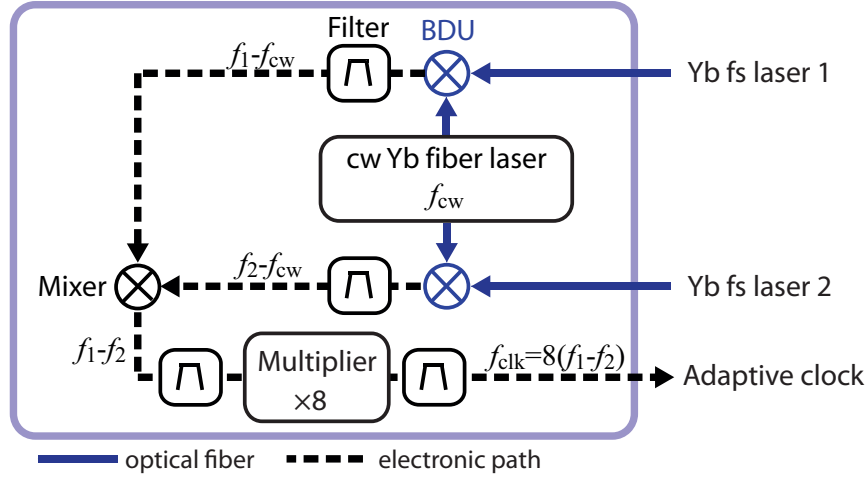


Figure 3.13: Adaptive clock generation scheme. Each fs oscillator beats with a cw free-running laser with a frequency f_{cw} in a beat detection unit (BDU) to isolate a single mode of each fs laser with a frequency of f_1 and f_2 , respectively. The two beating signals are electronically mixed in order to produce an electric signal $f_1 - f_2$ reporting the relative fluctuations between the two modes. This filtered and frequency-multiplied signal serves as the external clock to the digitizer.

3.5.2 Results and discussion

A portion of 15 cm^{-1} of the absorption spectrum of iodine around 19240 cm^{-1} is shown in Figure.3.14. The full spectrum spans 400 cm^{-1} and is measured within 12 ms, without averaging, at a Doppler-limited resolution of 0.02 cm^{-1} with triangular apodization. The signal to noise ratio is about 30. The spectrum is measured in the region of the center of the strong *B-X* 39-0 band [74]. Its wavenumber scale is calibrated against two iodine lines. The adaptive spectrum is compared to a spectrum resulting from an interferogram sampled at the constant clock rate of the data acquisition digitizer, and to the spectrum [75] of the ascii iodine atlas measured by Michelson-based Fourier transform spectroscopy. While the spectrum sampled at the constant clock rate of the data acquisition digitizer is strongly distorted, the adaptive spectrum shows good agreement with the reference data from the iodine atlas over a spectral span of 30 cm^{-1} of our spectral span, around twice the wavenumber of the cw laser used for generation of the adaptive clock. We indeed compensate for the fluctuations of the femtosecond lasers at a given optical frequency only. Therefore, phase errors scramble the spectral features over a span broader than 30 cm^{-1} . This could be overcome with the generation of a second adaptive signal, as recently reported with our results [53] around 6500 cm^{-1} . The adaptive scheme as performed

here around the fundamental wavelength of the lasers proves fully successful even when non-linear frequency conversion is implemented in the spectroscopy set-up. The spectrum reported in [75] spans 1400 cm^{-1} between 19100 and 20500 cm^{-1} and has been measured within 8 hours at a resolution of 0.02 cm^{-1} with a signal-to-noise ratio of the order of 60 around 19240 cm^{-1} . While a spectral span of 30 cm^{-1} is about 50 times narrower, our measurement time is 2×10^6 shorter. In high-resolution spectroscopy of atoms and molecules, iodine has been for decades a convenient frequency standard for calibration purposes due to its dense grid in a large part of the visible spectrum. Therefore, besides its interest as an appropriate test for our technique, the possibility to measure the highly-crowded iodine spectrum across 30 cm^{-1} within 12 ms offers an opportunity for frequency calibration of real-time spectroscopic data, as the free-running femtosecond lasers require calibration against molecular lines present in the spectrum.

We have demonstrated a dual-comb spectrometer capable of fully resolving the crowded Doppler-broadened spectrum of iodine in the green region over 30 cm^{-1} of spectral bandwidth within 12 ms. The spectrometer only requires free-running femtosecond laser oscillators and therefore the technique of dual-comb spectroscopy is dramatically simplified. As the adaptive clock generation can successfully compensate for the relative fluctuations of the laser systems when it is performed at the fundamental wavelength of the oscillators, our versatile scheme allows for straightforwardly reaching new spectral territories through nonlinear frequency conversion of near-infrared ultrafast laser sources. This may prove of particular relevance in the vacuum and extreme ultra-violet ranges where combs may be generated through high harmonic generation, as continuous-wave lasers are hardly available in these regions.

3.6 Conclusion

In this chapter, the potential of adaptive dual-comb spectroscopy is explored with free-running commercial mode-locked fiber lasers. This straight-forward technique without any comb-stabilization nor post data processing elegantly compensates for interferometric phase errors and shows very high quality dual-comb spectra (below 1.5 % residual error from calculated reference spectrum). Our demonstrations show the method can be used as a tool for precise quantitative spectroscopy measurements.

The adaptive sampling with a single adaptive signal (Section.3.3) is easy to implement but it compensates phase errors at a given optical frequency only. This can be utilized for

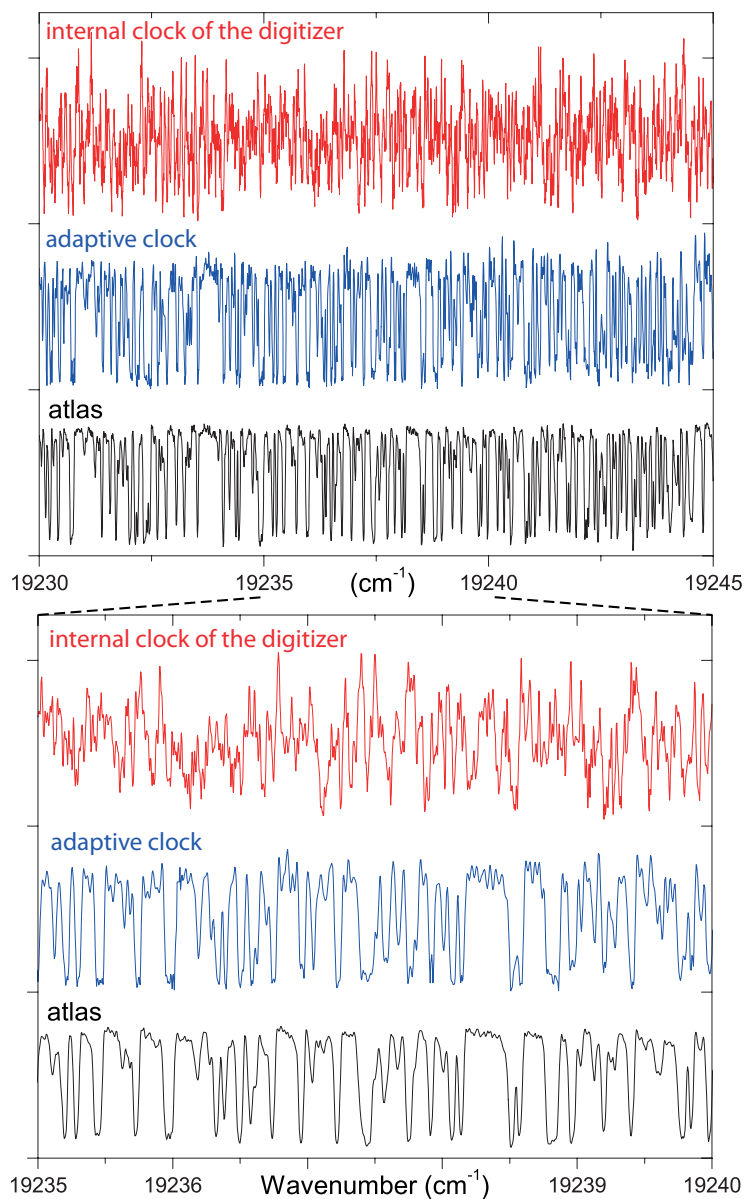


Figure 3.14: Iodine absorption spectra at a resolution of 0.02 cm^{-1} with two different degrees of zoom. For each inset: (upper) dual-comb spectrum with free-running lasers and sampled at the constant clock rate of the digitizer (middle) dual-comb spectrum with free-running lasers and with the adaptive clock, (lower) reproduced from the atlas of Ref. [75]. The dual-comb spectra are both measured within 12 ms in identical experimental conditions but the clock for digitization. The spectrum of [75] is measured with a 50 cm long I_2 cell, therefore the lines in our adaptive spectrum are more intense.

spectroscopy which focuses on relatively narrow spectral regions with high signal-to-noise ratio combined with narrow-band frequency combs or an optical bandpass filter.

The adaptive dual-comb spectroscopy with two adaptive signals (Section.3.4) provides full compensation of phase errors at small expense of the second adaptive signal generation. This automatic full compensation of phase errors not only releases users from complicated frequency comb stabilization but also provides opportunities to make highly quantitative spectroscopic measurement which cannot be achieved by radio-frequency stabilized frequency combs.

Dual-comb spectroscopy is anticipated to provide a variety of opportunities of direct frequency comb spectroscopy in broad spectral range from XUV to THz region. Frequency combs in such regions can most likely be generated by nonlinear frequency conversion started from technically sophisticated near-infrared frequency combs. The adaptive sampling proved to work in the frequency converted region with an adaptive signal generated from fundamental frequency combs (Section.3.5). This could be useful technique especially in the XUV or VUV region because it is very demanding to generate adaptive signals in these region due to lack of continuous-wave lasers.

Chapter 4

Development of a mid-infrared frequency comb

Since fundamental molecular vibrations are lying in the mid-infrared region from 500-5000 cm^{-1} (2-20 μm), direct frequency comb linear spectroscopy with mid-infrared frequency combs is a promising way to access vibrational transitions. However, mid-infrared frequency combs themselves are still relatively immature if these are compared to those in near-infrared region where most reports on direct frequency comb spectroscopy have been demonstrated. Therefore the development of mid-infrared frequency combs is an active research field at the time when this thesis is written. This chapter explores the development of broadband mid-infrared frequency combs aiming at mid-infrared dual-comb spectroscopy. We first describe the development of a synchronously pumped optical parametric oscillator (SP-OPO) generating a broadband spectrum with short pulse duration. In order to broaden the spectrum of the developed OPO, supercontinuum generation in the mid-infrared is demonstrated with a silicon waveguide on a chip.

The work in this chapter was made in collaborations. The synchronously-pumped optical parametric oscillator was developed with the group of Prof. Majid Ebrahim-Zadeh, ICFO in Barcelona, Spain. The experiment on mid-infrared supercontinuum generation in a silicon waveguide was made with the group of Prof. Roel Baets, Ghent University in Ghent, Belgium.

4.1 Background

The complicated spectra of fundamental molecular vibrational transitions have been investigated deeply and countless scientific achievements have been made by molecular scientists. Since every molecule has its own vibrational spectral pattern, it is also useful as a diagnostic method for identification of molecular samples in a variety of fields such as physical, chemical and biological analysis including environmental, medical analysis etc. The mid-infrared spectral region, $500\text{-}5000\text{ cm}^{-1}$ ($2\text{-}20\text{ }\mu\text{m}$), is the play ground of molecular fundamental vibrational transitions. Broadband mid-infrared spectroscopy has huge potential for these applications because of the availability of monitoring a variety of molecules simultaneously, especially when one deals with a complex sample. Fourier transform infrared spectrometer (FT-IR) has been a workhorse of broadband mid-infrared spectroscopy since long time ago back in 1969 when the first commercial device was introduced in to the market. The device brought a new methodology to investigate science and technology and nowadays it is used as a basic tool in a large number of chemical or biological research facilities on a daily basis. Although there has been a lot of technical improvements, the concept remained the same. In previous years, new concepts of mid-infrared broadband spectroscopy have caught attention triggered by the emergence of new mid-infrared broadband lasers. A mid-infrared frequency comb is one of the most promising lasers for such a molecular spectroscopy because of its high brightness and capability to be used for broadband, precise, accurate and rapid measurement.

4.1.1 Mid-infrared frequency combs

Mid-infrared frequency combs have been under development in a variety of ways, e.g. mode-locked lasers, microresonator-based Kerr combs, quantum cascade lasers (QCL), difference frequency generators (DFG), and optical parametric oscillators (OPO) [76]. Here we give an overview of these developments. **Mode-locked lasers** in the mid-infrared can be achieved with chalcogenide crystals such as ZnSe or ZnS doped with a transition metal such as chromium. Coupling of electronic transitions of a transition metal and phonon modes in a host crystal provides a broad gain bandwidth in the mid-infrared region. Kerr-lens mode-locking [77, 78] and saturable absorber mode-locking [79, 80] have been demonstrated and the coherence of the laser was indirectly proven by dual-comb spectroscopy [46]. Thulium-doped silica fiber mode-locked laser emitting around $1.9\text{ }\mu\text{m}$ has been developed in a variety of techniques [81–86]. Similarly to other fiber-based lasers,

powerful amplifiers can boost the power of these combs [86–88] so that it enables spectral broadening [86]. **A microresonator-based Kerr comb** is a newly appeared frequency comb source [89, 90]. Cascaded non-degenerate four-wave mixing results in phase-locking and even soliton mode-locking [91, 92] in the microresonator. Crystalline microresonators made of magnesium fluoride have ultra-high quality factor in the mid-infrared and generate Kerr combs covering 2.35-2.5 μm [93]. **A quantum cascade laser (QCL)** is a semiconductor-based mid-infrared source. Some experiments indicated possibility of mode-locking [94, 95], and recently the first frequency comb was demonstrated [96]. The newly developed semiconductor laser still has very limited bandwidth but has a promising potential for future practical applications.

Nonlinear frequency down-conversion is another route to achieve mid-infrared frequency combs. **Difference frequency generation (DFG)** is a second order nonlinear process which generates radiation at the difference frequency of two input light sources. A combination of a continuous-wave laser and a frequency comb can generate a mid-infrared frequency comb by the DFG process. A quasi-phase matching DFG by a periodically poled Lithium Niobate (PPLN) generates broadband mid-infrared frequency combs [45, 97]. Drawbacks of this method are weak output power (typically nanowatts per mode) and limited spectral width. While DFG with two actively synchronized pulses requires elaborate effort [98], DFG with a single pulse laser has advantage of passive phase stabilization. This method generates mid-infrared pulses in the 3-5 μm region with PPLN [71, 73, 99–102], and 3-17 μm region with gallium selenide [37, 38, 103–105]. Recent works showed high power per mode (>100 nW per mode), but the noise property was not appropriate for application toward sensitive dual-comb spectroscopy [102]. **Optical parametric oscillation (OPO)** is another way to generate mid-infrared frequency comb out of $\chi^{(2)}$ process with high photon conversion ratio. Synchronously pumped OPO opened up effective parametric oscillation for femtosecond ultrashort pulses [106, 107]. Tunable non-degenerate OPO in the mid-infrared region have been demonstrated with a PPLN crystal pumped by a solid-state laser [108–112] or a fiber laser [113]. Phase locking of comb modes of the signal and idler pulses have been demonstrated and showed potential as a frequency comb source in the mid-infrared [113–117]. Another trend is degenerate (subharmonic) OPOs which signal and idler degenerate at half of pump frequency. Near the degeneracy point, OPO gets high efficiency and broad spectrum. Several types of such OPOs have been demonstrated [118–121]. An advantage of the degenerate OPO is that the subharmonic signal (idler) is passively phase-locked to the pump, which makes easier to achieve a stable

frequency comb [122].

4.1.2 Direct mid-infrared frequency comb spectroscopy

Direct frequency comb spectroscopy (Section.2.1.2) is especially interesting in the mid-infrared because many strong fundamental molecular rovibrational transitions could be observed at once. In the mid-infrared region, several methods have been demonstrated including a mid-infrared VIPA spectrometer [123] and up-conversion through sum frequency generation [124]. Fourier transform spectroscopy seems to be a suitable method for the direct comb spectroscopy because it only requires a single detector. A Cr:ZnSe mode-locked laser around $2.4 \mu\text{m}$ [125] and an OPO-based frequency comb with a tuning range from 2.8 to $4.8 \mu\text{m}$ [33] have been used for the broadband spectroscopy combined with a Michelson interferometer. Cavity enhanced mid-infrared Fourier transform spectroscopy has also been demonstrated and showed its high sensitivity potential [126]. Dual-comb spectroscopy in the mid-infrared has also been demonstrated with Cr:ZnSe mode-locked lasers [46], with DFG combs [45], and with OPO combs [54]. These demonstrations were, however, proof-of-principle experiments and the measured spectra showed rather narrow bandwidth and poor quality (except for [45] which used combs stabilized by state-of-the art technique) because of the demanding comb stability (Chapter.3). For practical mid-infrared dual-comb spectroscopy, suitable frequency combs need to be developed.

4.2 Ultrashort synchronously pumped optical parametric oscillator

Although optical parametric oscillators (OPO) in nanosecond and continuous-wave regime had demonstrated in the late 1960s, picosecond and femtosecond OPOs awaited the development of suitable pump laser sources in the late 1980s [106,127]. Since such a short pulse has a limited spatial extent (e.g. $30 \mu\text{m}$ for 100 fs pulse), it is not possible for the down-converted light to travel in a nonlinear medium many times within the pulse duration. Therefore, synchronous pumping is necessary to build up such a ultrashort pulse OPO. In this technique, consecutive pump pulses hit the nonlinear crystal exactly at the same time that the circulating down-converted pulses in the OPO cavity comes back to the crystal. To put it in another way, the time interval of the adjacent pump pulses has to be the same as that of the down-converted pulses in the OPO cavity. Since OPO is a parametric nonlinear

process, the down-converted pulses can inherit the coherence of the pump pulses. In this sense, a frequency comb can be effectively down-converted through this process without losing the comb structure. Especially, the idler pulses of such OPOs are likely to be in the mid-infrared region, this technique is a very suitable way to have a mid-infrared frequency comb. Since our target application is direct frequency comb spectroscopy, broadband idler spectrum is attractive. OPO tends to be less noisy than the other nonlinear conversion processes such as DFG because of the OPO cavity which works as a sort of lowpass filter. This low noise capability is advantageous to the dual-comb spectroscopy. Here we develop a widely tunable ultrashort-pulse mid-infrared frequency comb through optical parametric oscillation.

4.2.1 Developed OPO system

Figure.4.1 shows the developed synchronously pumped optical parametric oscillator (SP-OPO) system. The pump source is a femtosecond mode-locked TiSa laser centered at 12658 cm^{-1} (790 nm) (Synergy20UHP: Femtolasers) with 20 fs pulse duration. The average power of the 100 MHz pulse train is up to 1.2 W. A pair of chirped mirrors pre-compensate the dispersion of the optics for pump pulse by -320 fs^2 so that the pulses are transform-limited when arriving at the OPO crystal. A lens (L1) with a focal length of 75 mm focuses the pump pulses onto the nonlinear crystal (MgO:PPLN; HC Photonics) (see below for details). The 150 cm long linear cavity consists of two concave mirrors with a radius of 100 mm (M1, M2) and three flat mirrors (M3, M4, M5). These are all coated with high reflection $>99 \%$ for the signal wavelength range, $6250\text{-}9804 \text{ cm}^{-1}$ (1020-1600 nm), with low reflection $<10 \%$ for the pump wavelength range, $11765\text{-}13333 \text{ cm}^{-1}$ (750-850 nm), and $<20 \%$ for the idler wavelength range, $1818\text{-}5405 \text{ cm}^{-1}$ (1850-5500 nm). A prism pair made of SF11 glass (PS857, Thorlabs) placed between the mirrors M4 and M5 compensates for intracavity dispersion mainly due to the PPLN crystal. One of the end mirrors (M5) sits on a translation stage so that the cavity length can be tuned. The idler pulses are transmitted through a mirror (M2) and are collimated with a CaF_2 lens (L2).

Design of the OPO system was conducted by S. Chaitanya Kumar (ICFO in Barcelona, Spain). Building the OPO cavity was done by S. Chaitanya Kumar, A. Esteban-Martin and T. Ideguchi at ICFO, Barcelona.

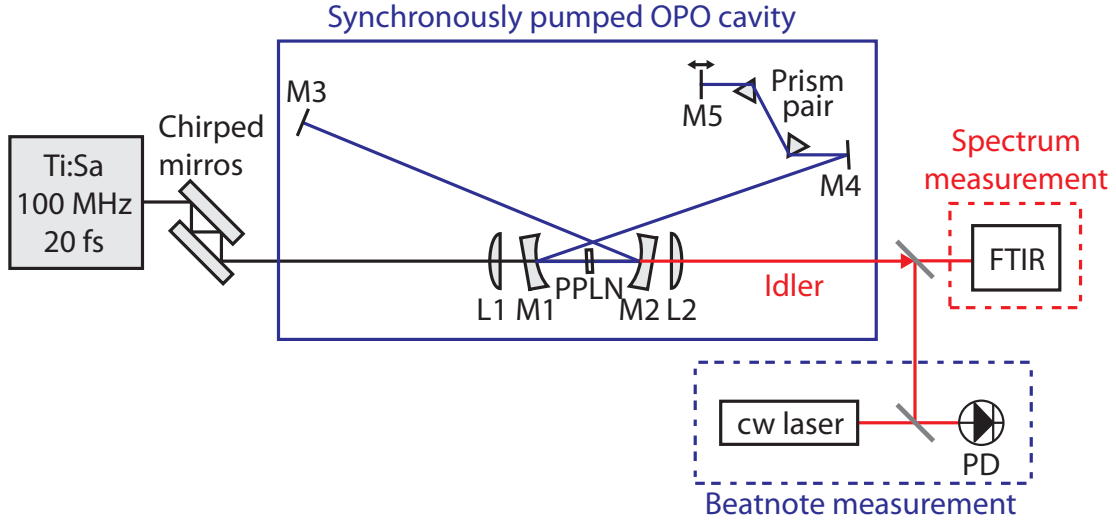


Figure 4.1: Layout of the developed synchronously-pumped optical parametric oscillator and diagnostics setup. PD: photodiode. FTIR: Fourier transform infrared spectrometer.

4.2.2 Nonlinear crystal

The nonlinear crystal is a MgO-doped periodically poled lithium niobate (MgO-PPLN) (HC photonics). The ferroelectric crystals which have opposite dipole moments are periodically poled, and the stacked crystal enables quasi-phase-matching for $\chi^{(2)}$ nonlinear effect. The MgO doping decreases the photorefractive effect that can damage the crystal and cause the output beam to be distorted. The crystal consists of 4 sections with different crystal length¹ of 250 μm , 500 μm , 750 μm , 1000 μm . Each section has a fan-out poling with a grating period of 19.0 - 21.3 μm . The temperature of the crystal is kept at 100 degree celsius with an oven to minimize the photorefractive effect and avoid fluctuations of refractive index of the crystal. The calculated phase-matching curve² is shown in Figure.4.2. The figure shows that the phase-matching condition allows to generate a broadband idler spectrum especially with a thinner crystal.

¹Here, crystal length indicates the length of PPLN grating section. The total crystal length including non-grating section is 1000 mm for all of them.

²The calculation is made by S. Chaitanya Kumar.

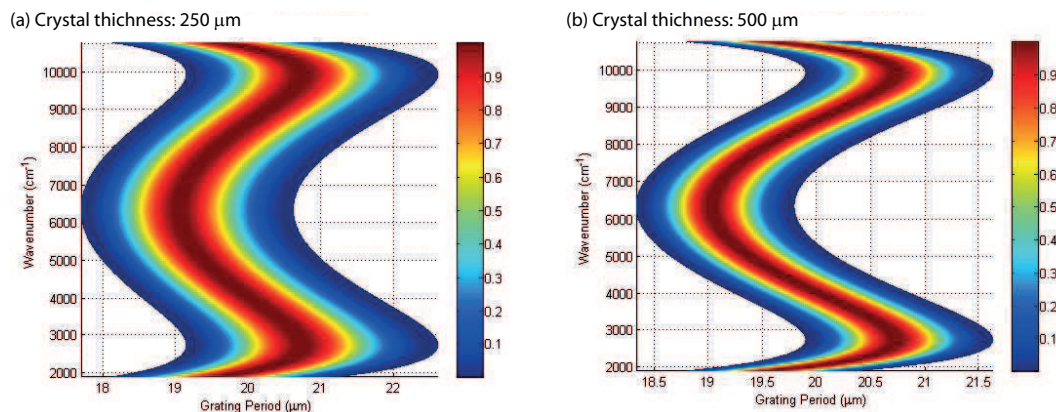


Figure 4.2: Calculated PPLN phase matching curves with (a) crystal thickness of 250 μm and (b) 500 μm . The pump wavenumber of 12658 (790 nm) and the temperature of 100 degree celsius are used for the calculation. Refractive index of the PPLN crystal is calculated with the temperature dependent sellmeier equation [128].

4.2.3 Characterization of the mid-infrared idler pulse

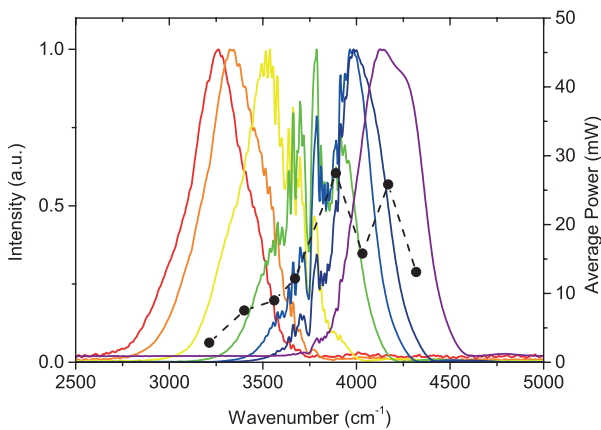
Spectra and average power

The idler spectra are measured with a commercial FT-IR spectrometer (VERTEX70, Bruker). Figure.4.3 shows the spectra over the tuning range generated with crystals which thickness of (a) 250 μm , (b) 500 μm . The wavenumber tuning is easily made only by changing the OPO cavity length [127]. The mechanism owes to the OPO intracavity dispersion. In order to keep the synchronous pumping condition, cavity round-trip time of the signal pulse must be the same as the pump pulse interval. Since the OPO cavity has dispersion, the round-trip time of the signal depends on the wavenumber. Therefore one can shift the wavenumber of the synchronously pumped signal pulses by changing the cavity length. This mechanically changeable OPO wavenumber could be useful for some applications which require rapid wavenumber tuning. A fast piezo-electric transducer may be used for such quick cavity tuning. Spectra with the 250 μm crystal covers from 2750 to 4600 cm^{-1} (2174-3636 nm) while those with 500 μm covers broader span from 2400 to 5500 cm^{-1} (1818-4167 nm) (Figure.4.3). The average power is plotted in the same figure. A few to tens of milliwatts idler output power is obtained. This plot shows the tuning range and power in the same cavity condition optimized to around the center of the tuning range.

The characterizations were done by S. Chaitanya Kumar, A. Esteban-Martin, T. Ideguchi, S. Holzner and M. Yan at Max-Planck Institut für Quantenoptik, Garching.

The cavity can be optimized to get higher power in a given region. For example, one can get above 30 mW around 2700 cm^{-1} (3704 nm) with the $500\text{ }\mu\text{m}$ crystal if the cavity is optimized at this point. Figure.4.4 shows a spectrum centered around 3250 cm^{-1} (3077 nm). As expected with the phase matching condition, the thinner $250\text{ }\mu\text{m}$ crystal provides a larger bandwidth, 360 cm^{-1} of FWHM (1000 cm^{-1} from edge to edge), while that of the $500\text{ }\mu\text{m}$ crystal provides 230 cm^{-1} FWHM (500 cm^{-1} from edge to edge). This broadband spectrum in the mid-infrared, to the best of our knowledge, is the broadest mid-infrared OPO source in this wavenumber region.

(a) Crystal thickness: $250\text{ }\mu\text{m}$



(b) Crystal thickness: $500\text{ }\mu\text{m}$

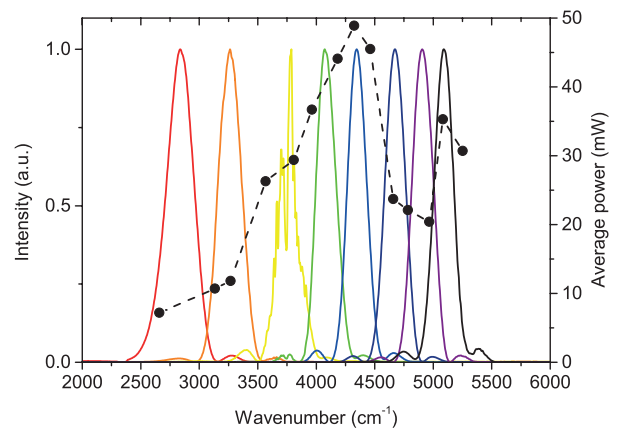
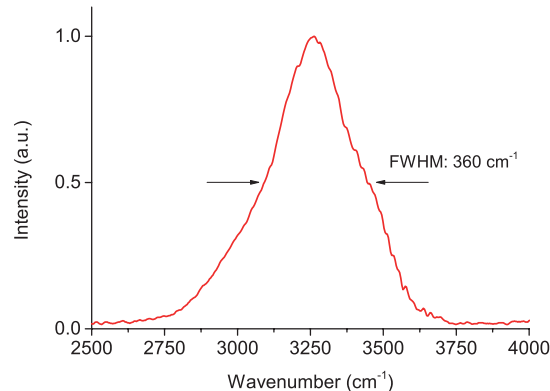


Figure 4.3: The OPO idler spectra with (a) $250\text{ }\mu\text{m}$ PPLN, (b) $500\text{ }\mu\text{m}$ PPLN. The black dots shows average power.

(a) Crystal thickness: $250\text{ }\mu\text{m}$



(b) Crystal thickness: $500\text{ }\mu\text{m}$

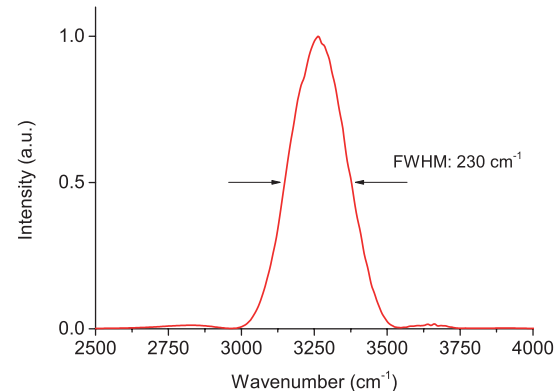


Figure 4.4: The idler spectrum around 3250 cm^{-1} (3077 nm) with (a) $250\text{ }\mu\text{m}$ PPLN, (b) $500\text{ }\mu\text{m}$ PPLN. The FWHM bandwidth is (a) 360 cm^{-1} , (b) 230 cm^{-1} .

Pump power dependence: OPO threshold

The idler power is measured as a function of the pump power (Figure.4.5). The central wavenumber of the idler is set to 2686 cm^{-1} with $500\text{ }\mu\text{m}$ crystal. The OPO oscillation threshold is 700 mW and the slope efficiency is 14.5% .

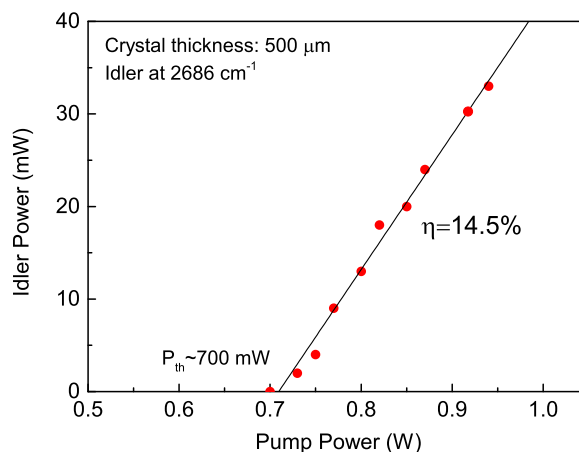


Figure 4.5: The idler power at 2686 cm^{-1} with $500\text{ }\mu\text{m}$ crystal measured as a function of the pump power. The OPO oscillation threshold (P_{th}) is 700 mW and the slope efficiency (η) is 14.5% .

Autocorrelation

Autocorrelation traces are measured with a home-made Michelson interferometer and a two-photon InGaAs photodetector (PDA10CF, Thorlabs). Since the water absorption band around $3000\text{-}4000\text{ cm}^{-1}$ ($2500\text{-}3333\text{ nm}$) distorts the waveform of the idler pulse, good autocorrelation trace enough for estimation of the pulse duration can only be taken outside of the absorption band. The Figure.4.6 shows the autocorrelation traces at 4460 cm^{-1} (2242 nm). Very short pulse duration of 33 fs , which corresponds to 4.3 cycle, is observed with the $250\text{ }\mu\text{m}$. The pulse duration is estimated with the fringe counting method assuming a sech^2 pulse shape. This is, to the best of our knowledge, the shortest and fewest cycle mid-infrared pulse out of a synchronously pumped OPO³. The time-bandwidth product is 0.39 (pulse duration of 33 fs and bandwidth of 390 cm^{-1} (11.7 THz)).

³The best report was 51 fs (4.9 cycles) around $3.1\text{ }\mu\text{m}$ generated by a degenerate OPO [121].

for the pulse at 4460 cm^{-1}), which is close to the value for transform limit pulse (0.315 for a sech^2 shaped pulse), but there is still room for improvement of dispersion compensation.

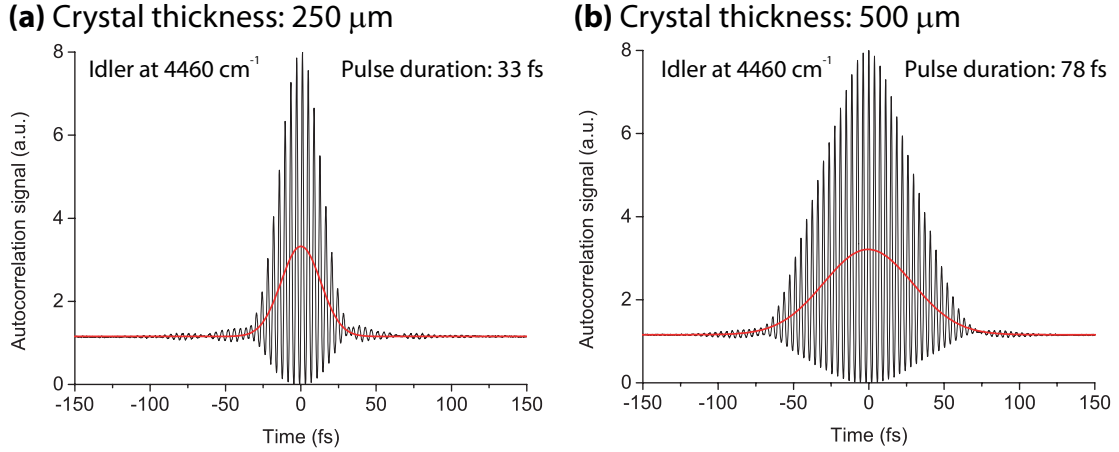


Figure 4.6: Autocorrelation trace of the idler pulse at 4460 cm^{-1} with the PPLN crystal of (a) $250\text{ }\mu\text{m}$, and (b) $500\text{ }\mu\text{m}$.

Power stability

The average power of the idler beam at 2725 cm^{-1} (3670 nm) with the $500\text{ }\mu\text{m}$ is measured over 10000 seconds (Figure.4.7). During the measurement, the repetition frequency of the pump laser is stabilized to 100 MHz to evaluate stability of the OPO system itself, e.g. the mechanical stability of the OPO cavity or the refractive index instability due to air flow in the cavity. The data shows good long-term stability with 0.4 mW standard deviation.

Coherence

In order to check the coherence of the idler pulse train, a beat note measurement is made with a free-running continuous-wave OPO (Argos, Aculight). The beat note is measured with a 100-MHz-bandwidth extended InGaAsSb photodiode (D124, Redwave Labs). The measured radio frequency spectrum shows a clear single beat note which indicates the OPO idler inherits the coherence of the pump pulse train (Figure.4.8). At this stage, the beat note jitters around by a few MHz/s because the pump and the OPO cavity are not stabilized. In order to capture the free-running beat note, the measurement conditions of the spectrum analyzer such as the sweep time (ST) or the resolution bandwidth (RBW) are set for a quick measurement, ST: 20 ms and RBW: 10 kHz, and this limits linewidth of the

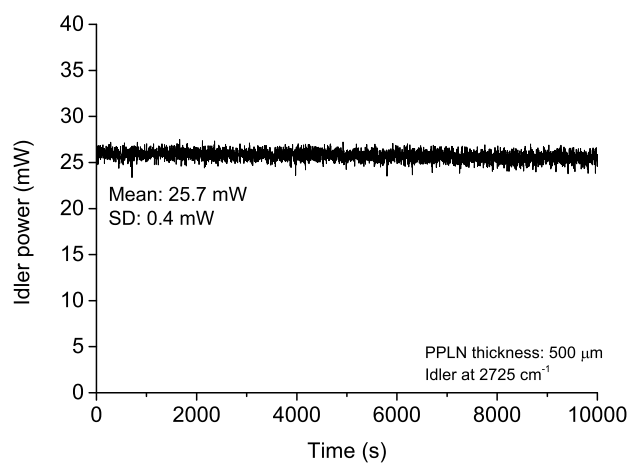


Figure 4.7: Average power of the idler beam at 2725 cm^{-1} (3670 nm) with the $500\text{ }\mu\text{m}$ crystal over 10000 s .

beat notes. The stabilization of the comb can be done by either against continuous-wave lasers or by a scheme utilizing non-phase-matched OPO radiations such as sum-frequency generation of the pump and signal etc. [113–117]. A $f\text{-}2f$ interferometer for stabilizing the offset frequency of the idler comb can also be possible if the idler pulses are broadening over an octave.

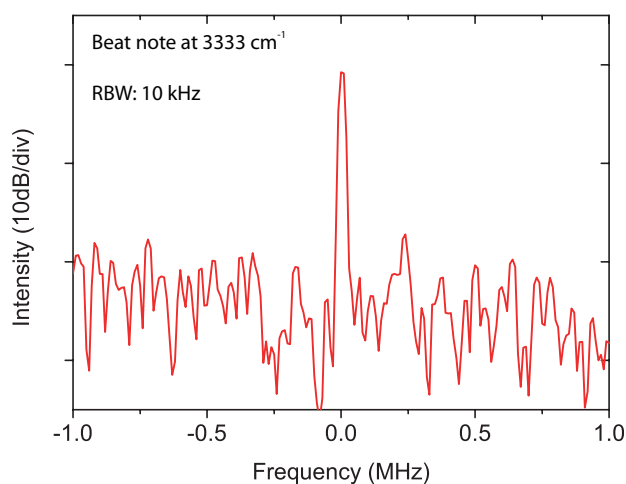


Figure 4.8: A beat note between the idler pulse train and a continuous-wave OPO at 3333 cm^{-1} . RBW: Resolution bandwidth

4.3 Mid-infrared supercontinuum generation in Silicon waveguide

Supercontinuum generation (SCG) is a widely used technique to generate broadband light sources. In the mid-infrared region, SCG have been demonstrated mostly with specialty materials: chalcogenide glasses containing chalcogen elements such as sulfide, selenide and telluride [129,130]. These materials show good specifications for mid-infrared supercontinuum but there would encounter a wall for practical usages in a variety of fields because of the unusual materials. In this context, another promising material is silicon. Silicon has been a basic material of chip scale electronics, and recently the optical properties of the material have been investigated mostly in the telecommunication region, thus developing the field of silicon photonics [131]. Thanks to highly sophisticated CMOS fabrication processes, fine photonic circuits can be integrated on a chip. Silicon, on the other hand, has potential to be a good optical material in the mid-infrared region because of the transparency from $1250\text{-}9090\text{ cm}^{-1}$ ($1.1\text{ - }8\text{ }\mu\text{m}$). Additionally, this material has large nonlinearities (e.g. $n_2=6.23\times 10^{-18}\text{ m}^2/\text{W}$ at $2.2\text{ }\mu\text{m}$), therefore the combination of the small-size-material fabrication, which leads to tight confinement of light in a small volume, and the high nonlinearity make silicon a good candidate for nonlinear optics. Silicon nano-wire is a simple waveguide and it has been investigated as a nonlinear material [132]. Supercontinuum generation in the silicon waveguide has been demonstrated in the mid-infrared to telecom-band, $3960\text{ - }6515\text{ cm}^{-1}$ ($1535\text{ - }2525\text{ nm}$) [133].

In the context of frequency comb, supercontinuum generation by a photonic crystal fiber [134] provided the last piece of realization of a self-referenced frequency comb synthesizer through octave-spanning spectral broadening for the f-2f interferometer [31]. A key of the success was that the spectral broadening process deterministically produced the broadened spectra [135]. Hence, if one injects an ultrashort pulse train, the output of the supercontinuum generation inherits the coherence property of the input pulse train and produces a broadband frequency comb. However, supercontinuum generation does not always keep the coherence of the input pulse train because there are several noise-driven broadening processes which cause decoherence [136]. An important conclusion of the investigations about coherence in supercontinuum generation process is that with an input pulse in the anomalous-dispersion regime, a temporally short input pulse (typically less than 100 fs, although it depends on the other conditions) induces a coherent broadening while a longer input pulse does not. In the short pulse regime, self-phase modulation dominantly drives

the broadening and the parametric process keeps coherence. In the longer pulse regime, on the other hand, a main broadening is driven by so called modulation instability which is highly sensitive to input pulse noise and causes the decoherence [137]. In the previous demonstration of supercontinuum generation with a silicon waveguide in the mid-infrared to telecom-band [133], picosecond pulses lead to supercontinuum but the mechanism was experimentally shown to be background noise driven, therefore one could not expect a coherent output.

This section explores supercontinuum generation in a silicon waveguide for the realization of a broadband mid-infrared frequency comb. Our demonstration shows a broadband SCG spectrum over an octave spanning range in the mid-infrared, and the coherence is preserved. This broadband frequency comb has the potential to be used as a source of dual-comb spectroscopy⁴ and for a f-2f interferometer in the mid-infrared.

4.3.1 Silicon waveguide

Silicon waveguides were designed by Bart Kuyken (Ghent University in Ghent, Belgium) and processed in a cleanroom of imec (Interuniversity Microelectronics Centre) in Belgium. Details of the fabrication process of the silicon-on-insulator (SOI) can be found in literature [138]. Since the fabrication process is standardized for waveguides in the 1550 nm region, the height (thickness) of the waveguide is usually fixed to 220 nm which does not cause substrate leakage in the telecom region but for longer wavelengths, it does cause the leakage. Here, our waveguide is fabricated with 400 nm height by specialized fabrication parameters in order to minimize the leakage at around 3000 nm region. Schematic geometry of the silicon waveguide is depicted in Figure.4.9. The silicon waveguide with 400 nm (Height), 1600 nm (Width), and 10 mm (Length) is on a 2 μm layer of silicon oxide (SiO_2). Beneath the SiO_2 layer, there is a 750 μm of silicon layer. At the facets on both sides, the waveguide is tapered to 3000 nm in width. The transparency window of the silicon is 1.1 - 8 μm while that of the silicon oxide is up to 4 μm . Therefore the SOI waveguide has the potential to be a photonic circuits in 2500-9090 cm^{-1} (1.1 - 4 μm).

The calculated second-order dispersion for TE polarization mode of the silicon waveguide⁵ is shown in Figure.4.10. The waveguide has anomalous dispersion ($\beta_2 < 0$) from 2100 to 4700 cm^{-1} (2128-4762 nm) including wavenumber of input pulse at 4360 cm^{-1} (2.29 μm),

⁴The intensity distribution of the spectrum has to be improved in order to use it for dual-comb spectroscopy.

⁵The calculation is made by B. Kuyken.

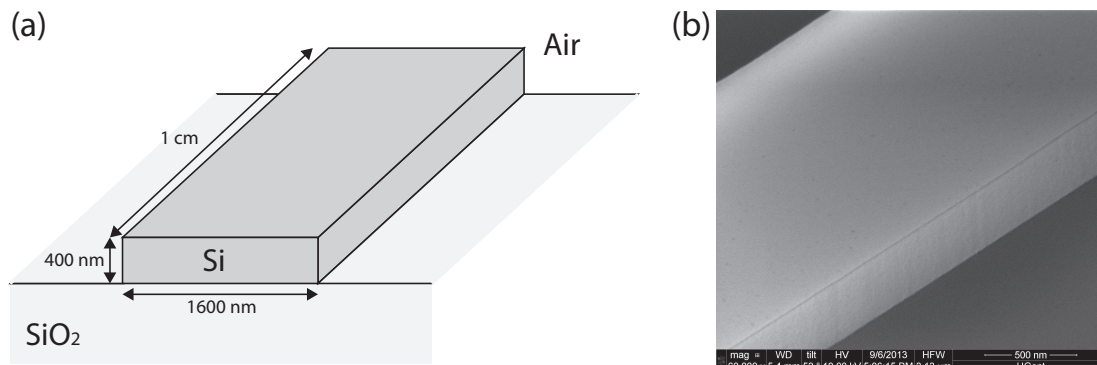


Figure 4.9: (a) Sketch of the silicon waveguide on a chip. (b) A scanning electron microscope image of the silicon waveguide.

which supports broadband supercontinuum generation.

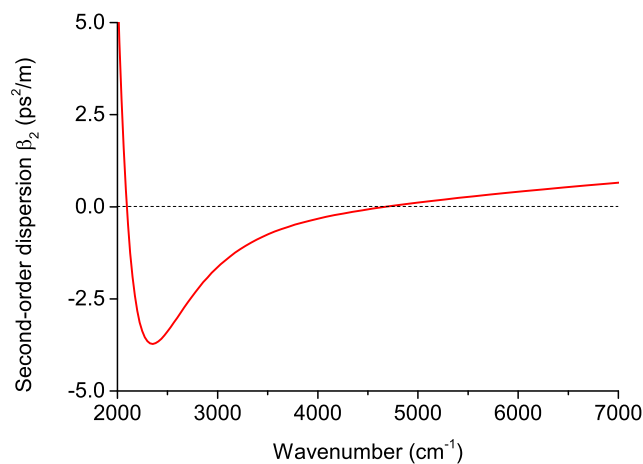


Figure 4.10: Group velocity dispersion of the silicon waveguide for TE polarization mode.

4.3.2 Experimental setup

The idler pulse that is emitted from a home-made synchronously pumped OPO (Section 4.2), 72 fs at 4360 cm^{-1} ($2.29 \mu\text{m}$) with a repetition frequency 100 MHz, is injected into the Si waveguide by a lens made of Black Diamond-2 with an effective focal length of 1.873 mm (0.85 NA) (C037TME-D, Thorlabs). In order to avoid strong two photon absorption in silicon, which limits the efficiency of nonlinear processes in the telecom region [139], the input wavenumber is chosen below threshold 4545 cm^{-1} (2200 nm). The

beam-diameter of the input pulse is adjusted with a telescope for an effective injection. The polarization of the input pulse is set to TE mode. The output of the waveguide is collimated by the same type of lens as for the injection. The input pulse has 25 mW average power before lens, therefore the pulse has 225 W of peak power assuming 12 dB coupling loss. The total loss through the chip and lenses is about 20 dB.

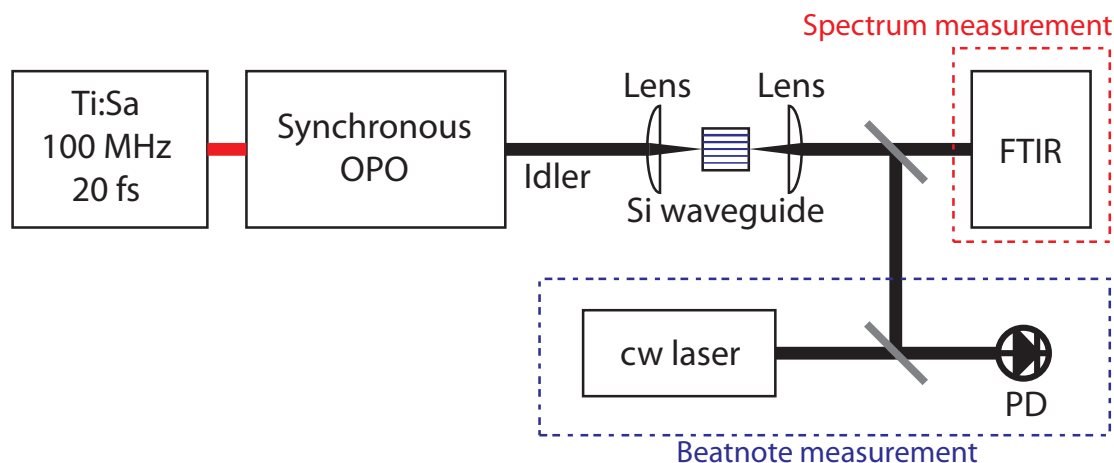


Figure 4.11: Setup of the mid-infrared supercontinuum generation in silicon waveguide. FTIR: Fourier transform infrared spectrometer. PD: photodiode.

4.3.3 Mid-infrared supercontinuum spectrum

A spectrum of supercontinuum generation is measured by a commercial FT-IR spectrometer (VERTEX70, Bruker). Figure.4.12 shows the input spectrum in the black line and the supercontinuum spectrum in the red line. Significant broadening is observed ranging from 3070 cm^{-1} to 6480 cm^{-1} ($1543 - 3257\text{ nm}$) at -30 dB level, which exceeds an octave spanning. The dotted lines indicate the position where beat note measurements were made for confirming the coherence property.

4.3.4 Coherence

The coherence property is examined by beat note measurements in several spectral regions. For the measurement at 3876 cm^{-1} (2640 nm) and 4132 cm^{-1} (2420 nm), a free-running continuous-wave OPO (Argos, Aculight) is used as a local oscillator. The linewidth of the continuous-wave OPO is less than 60 kHz in $500\text{ }\mu\text{s}$ measurement time. Each beatnote is measured with a 100 MHz bandwidth extended InGaAsSb photodiode (D124, Redwave

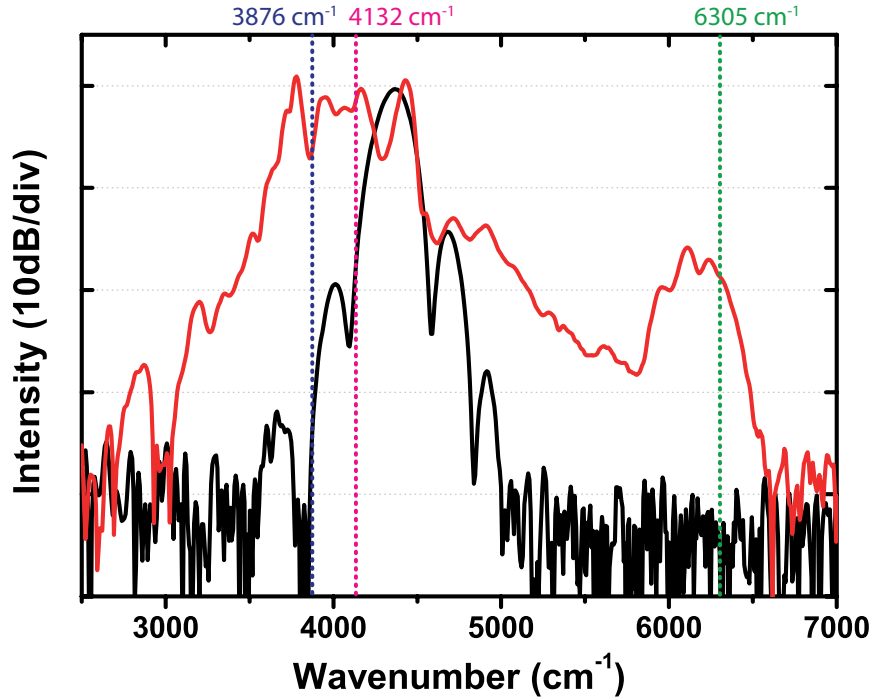


Figure 4.12: Supercontinuum spectrum in the Si waveguide. The black and red lines indicate the input and output spectra of the Si waveguide. The dotted lines are the positions where the beatnotes with cw lasers are measured.

Labs). For the measurement at 6305 cm^{-1} (1586 nm), a free running Er-doped fiber laser (Koheras, NKT Photonics) is used. The linewidth of the laser is less than 1 kHz in 100 μs measurement time and a beatnote is measured with a balanced InGaAs detector (Thorlabs). The measured beat notes are shown in Figure.4.13. Each of beat notes at different spectral positions shows a clear single peak which indicates the SCG process preserves the coherence over the spectrum. Since the input OPO pulses are not stabilized at all, the comb structure fluctuate and this fluctuation limits the measurement condition and thus limits the linewidth of the beat notes. This experiment is the first observation of the coherence property of the SCG by a silicon waveguide in the mid-infrared.

4.4 Conclusion

This chapter explored the development of a mid-infrared frequency comb. A broadband frequency comb was developed through a synchronously pumped optical parametric oscillator with a MgO-PPLN crystal and the laser showed ultrashort (33 fs at best) temporal

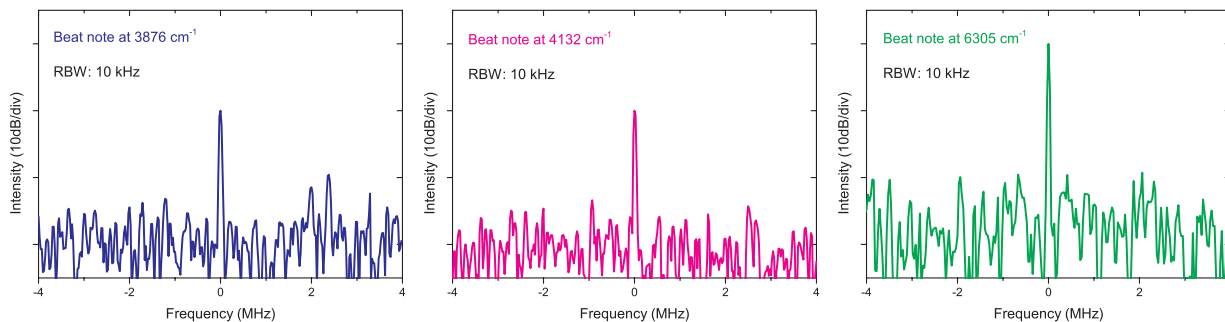


Figure 4.13: The beatnotes between the supercontinuum spectrum and cw lasers at 3876 cm^{-1} (left), 4132 cm^{-1} (center), and 6305 cm^{-1} (right).

pulse duration and broadband (FWHM of 360 cm^{-1}) spectrum. The laser also showed a broad tuning range from 2400 to 5500 cm^{-1} (1818 - 4167 nm) with a few to tens of mW average power. These specifications are appropriate for broadband dual-comb spectroscopy. Moreover the 4.3 cycle ultrashort pulse in the mid-infrared region could be used for other applications such as attosecond science where few cycle pulses in the mid-infrared region is advantageous.

Supercontinuum spectral broadening of the OPO was demonstrated in silicon waveguide. The CMOS compatible on-tip waveguide successfully broadened the mid-infrared pulse over octave-spanning range. The coherence property was examined over a wide spectral range and the preserved coherence was confirmed experimentally. This octave spanning mid-infrared frequency comb could be used for broadband dual-comb spectroscopy. Also the octave spanning comb could be utilized for a f - $2f$ self referenced frequency comb in the mid-infrared region. Although the other supercontinuum generations, e.g. with chalcogenide fibers, demonstrated much broader spectra [130], the silicon waveguide holds promising future because of the basic material and already existing sophisticated fabrication.

Part II

Nonlinear dual-comb spectroscopy

Nonlinear dual-comb spectroscopy

Dual-comb spectroscopy has proved to have a great potential in broadband molecular spectroscopy in terms of measurement speed, precision, and accuracy. All the demonstrations of dual-comb spectroscopy, so far, had been conducted in the linear light-matter interaction regime. In linear absorption spectroscopy, high peak intensity of the frequency combs: the temporal nature of the ultrashort pulse, does not bring any advantage to dual-comb spectroscopy but causes limitation of the dynamic range of the interferometric signal by saturation of a detector or a digitizer. On the other hand, the high intensity of the pulse brings huge benefit if it is harnessed for nonlinear processes. Hence, dual-comb spectroscopy inherently has the potential to be applied to nonlinear spectroscopy.

Nonlinear spectroscopy provides us a variety of useful aspects on atoms or molecules which cannot be obtained by linear spectroscopy. For example, saturated absorption spectroscopy and counter-propagating two photon absorption spectroscopy enable to measure Doppler-free molecular spectra, and coherent Raman spectroscopy makes it possible to visualize biological molecules non-invasively by accessing the molecule's inherent vibrational nature. Moreover, 3D sectioning capability comes together with all the nonlinear processes, which is of huge interest to microscopic bio-imaging.

Coherent Raman dual-comb spectroscopy

Every molecule vibrates in its own way at particular frequencies. The vibrational spectrum is called "Molecular fingerprint" which is analogous to the human fingerprints used for detective purpose, because it is useful for identification of the molecules. The molecular identification is particularly useful for bio-imaging applications because of the non-invasive nature. Since the frequency of the molecular fingerprint vibrations are sitting in $500\text{-}1500\text{ cm}^{-1}$ which corresponds to wavelength of $6.7\text{ - }20\text{ }\mu\text{m}$, mid-infrared light sources are required to acquire linear absorption molecular spectra. Molecular fingerprinting linear dual-comb spectroscopy is promising, but a properly designed frequency comb is not commercially available yet. Several types of mid-infrared frequency combs have been demonstrated [76], and their development still provides on-going scientific research field (Chapter.4).

Raman spectroscopy is another way to access molecular vibrational bands. Especially, nonlinear coherent Raman scattering is suitable process for molecular vibrational spectroscopy because the scattering efficiency is orders of magnitude higher than the spontaneous Ra-

man scattering. This high efficiency allows us to measure the molecular oscillations in short acquisition time. Also, such a process gets benefit of 3D sectioning capability by tight focusing due to the general feature of nonlinear effect. Moreover, since Raman transition allows us to use any short-wavelength light sources, from ultra-violet to near-infrared, tight focusing on an imaging sample increases the spatial resolution, which is determined by the diffraction limit.

Many demonstrations have been reported aiming at high speed molecular vibrational spectroscopy and microscopy in the last decade, mostly only with one spectral element by picosecond lasers [140, 141]. Very recently, broadband spectroscopic capability has been investigated to be combined with the high speed imaging [142–145].

In this part of the thesis, we investigate new broadband coherent Raman spectroscopy with a dual-comb scheme. The high speed and broadband dual-comb spectroscopy meets nonlinear coherent Raman effects and shows promising potentials which could surpass the other techniques demonstrated so far.

Chapter 5

Raman-induced Kerr-effect dual-comb spectroscopy

5.1 Background

5.1.1 Stimulated Raman spectroscopy

Stimulated Raman scattering (SRS) is one of the coherent Raman scattering processes [146]. This third order nonlinear process occurs when the frequency difference between two beams with different frequencies, pump frequency (f_p) and Stokes frequency (f_S), matches a molecular Raman vibrational frequency ($f_p - f_S = f_{vib}$). In the quantum mechanical photon picture, a molecular vibrational state is excited through photon conversion from a pump to a Stokes photon in a process which obeys the energy conservation law. Since the molecule gets energy from photons through the process, SRS is a non-parametric process that probes the excited vibrational population instead of vibrational coherence detected by CARS which is categorized in parametric process (see Chapter 6 for details). The resulting intensity loss of the pump beam is called stimulated Raman loss, and the intensity gain of the Stokes beam is called stimulated Raman gain. In the semiclassical picture, SRS can be described as a heterodyne phenomenon between the incident fundamental electric fields and the induced nonlinear polarizations. Following the condition of $f_p - f_S = f_{vib}$, two third-order nonlinear polarizations, P_p and P_S are generated at the frequency of the

The contents in this chapter is published in [59]

fundamental frequencies of pump (f_p) and Stokes (f_s):

$$\begin{aligned} P_p &\propto \chi^{(3)} E_p E_S^* E_S \\ P_S &\propto \chi^{(3)} E_p E_p^* E_S \end{aligned}$$

where $\chi^{(3)} = \chi_R^{(3)} + \chi_{NR}^{(3)}$ is the third-order susceptibility, E_p and E_S are the incident fundamental pump and Stokes electric fields. $\chi_R^{(3)}$ and $\chi_{NR}^{(3)}$ represent the resonant and nonresonant part of the susceptibility. The induced polarizations P_p and P_S propagate in the forward direction and interfere with the incident fundamental pump and Stokes fields with their corresponding phases. The pump field destructively interferes with the polarization P_p and the pump intensity experiences losses:

$$\Delta I_p \propto -2\text{Im}[\chi_R^{(3)}] I_p I_S$$

where I_p and I_S represent the intensity of the pump and probe beams, and ΔI_p is intensity difference of the pump beam before and after the SRS process. Since $\chi_{NR}^{(3)}$ is a real value, the non-resonant process doesn't appear in the Raman loss. The Stokes field interferes constructively with the induced polarization P_S and the Stokes intensity results in acquiring the gain:

$$\Delta I_S \propto 2\text{Im}[\chi_R^{(3)}] I_p I_S$$

where ΔI_S is intensity difference of the Stokes beam before and after the SRS process. Comparing the Stokes beam (pump beam) intensity with and without the pump beam (Stokes beam) reveals ΔI_S (ΔI_p) which indicates the existence of a resonant Raman vibration in the molecule at the frequency f_{vib} . This can be used for spectroscopy by scanning one of the colors of either the pump or Stokes beam. The energy diagram and the spectral change is described in the Figure.5.1.

High-speed SRS

Ultrashort pulse lasers are suitable light sources for SRS because of their high peak power and many demonstrations with picosecond lasers have been reported. A picosecond laser, e.g. 10 ps pulse duration, behaves as a single color beam for most of liquid samples because the intrinsic linewidth of vibrational transitions of liquids (typical value is about 100 GHz) are comparable to or broader than the linewidth of the picosecond laser (44 GHz, assuming transform limited 10 ps Gaussian pulse). Combining SRS based on picosecond lasers with scanning microscopy enables high-speed vibrational imaging. The method is

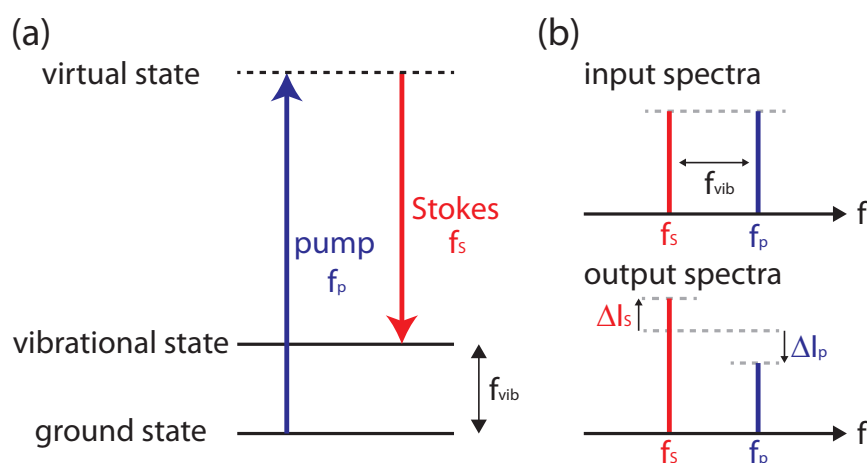


Figure 5.1: (a) Energy diagram of SRS. (b) Input and output spectra of SRS.

promising especially for *in vivo* imaging because of its non-invasive nature. In the field of bio-molecular imaging, fluorescent imaging has been the workhorse because of its high sensitivity. However, staining the target molecules with such fluorescent label molecules perturbs the system, especially when the target molecule is smaller than the label molecule. Label-free vibrational imaging overcomes this issue [147]. Sensitive single-color microscopic imaging was reported with high-frequency modulation transfer method [148–150], and afterwards, ultrafast video-frame-rate imaging was demonstrated [141] by improving this scheme. With one-color SRS imaging, however, only a single target Raman vibrational mode is imaged. Recently, multi-color imaging were demonstrated either by scanning the laser frequency frame-by-frame [142, 143, 151], by using chirped pulse [145], or by spectral tailoring technique [152–154]. The chemical specificity of multicolor spectroscopy expands the potential of such kind of vibrational method.

Broadband femtosecond lasers can also be used for multi-color spectroscopy as a Stokes beam combined with a picosecond pump laser¹. The broadband Stokes pulse can see several Raman vibrational modes within the spectral bandwidth simultaneously. Many experiments have been reported with amplified femtosecond laser systems with high pulse intensities [155, 156]. However, such amplified lasers usually have a low repetition rate (typically kHz level) which results in slow measurements. Fast measurements with high repetition rate femtosecond laser system have been demonstrated with a grating spectrometer to obtain the Stokes spectra [157]. The limitation of the speed is set by the read-out time of the detection system. High repetition rate SRS is promising not only be-

¹A combination of a femtosecond pump and a picosecond Stokes beams also works.

cause of the fast measurement but also of the low pulse intensity per pulse which reduces the possibility of damaging the biological samples. SRS with a single femtosecond laser has also been demonstrated with slow amplified kHz system combined with pulse shaping technique [158].

5.1.2 Raman-induced Kerr-effect spectroscopy

Raman-induced Kerr-effect spectroscopy (RIKES) is a similar process to SRS except for the polarization configuration [159, 160]. There are two different beam geometries: one uses a circularly polarized pump beam and a linearly polarized Stokes beam (circular RIKES), and the other uses a linearly polarized pump beam at a 45 degree angle with respect to a linearly polarized Stokes beam (linear RIKES). The pump and Stokes beams in these geometries induce birefringence and generate Raman signals with a polarization orthogonal to that of the incident Stokes beam. Since only the small amount of the orthogonal component can be detected by blocking the fundamental Stokes beam with a cross polarizer, this is a background free detection scheme, which can lead to improvement of detection signal-to-noise ratio. Figure.5.2 shows the typical polarization configurations of SRS and RIKES. RIKES have been widely used in spectroscopy [159]. Recently, demonstration of RIKES using ultrashort pulses have been reported with amplified systems [161, 162] and with high repetition rate oscillators [163, 164].

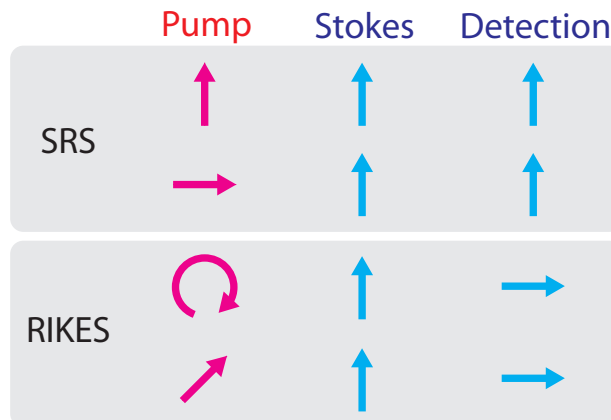


Figure 5.2: Polarization configuration of SRS and RIKES

5.2 Principle

Figure.5.3 is the conceptual description of the dual-comb RIKES. In dual-comb SRS and RIKES, a pump picosecond laser and a Stokes femtosecond frequency comb both emitting pulses at a repetition frequency of f are spatially and temporally overlapped onto the sample. Photons are transferred from the intense pump beam to the weak Stokes beam when the energy difference between the pump and the Stokes comb lines coincide with a Raman resonance of the sample. Since the generated Raman signal inherits the periodicity of the Stokes pulse train, the Raman lines also have frequency comb structure. These Raman lines are multi-heterodyned against a local oscillator comb which repetition frequency, $f + \delta f$, is slightly different from that of Stokes comb f . The multi-heterodyne detection magnifies the weak signal field and downconverts the comb of Raman signals to the radio frequency domain, where it is easily accessible by fast digital processing. This scheme without moving parts enables highly multiplexed fast measurements over a spectral span as broad as the bandwidth of the Stokes femtosecond optical comb, with simultaneous access to the real and imaginary parts of the nonlinear susceptibility.

In the case of SRS, the pump and Stokes pulses are linearly polarized and the transferred photon has the same polarization as the Stokes pulse. On the other hand, in RIKES, a circularly polarized pump pulse and a linearly polarized Stokes pulse are used, and this results in the transferred photon having an orthogonal polarization with respect to that of the Stokes pulse due to the birefringence in the interacting matter with the pulses. Detection of the changes in the polarization provides sensitivity enhancement and reduction of artifacts like cross-phase modulation and parasitic interference patterns [163].

5.3 Experimental setup

The experimental setup of dual-comb RIKES is displayed in Figure. 5.4. A femtosecond Yb-doped fiber femtosecond laser/amplifier system (details in 5.3.1) with a repetition frequency of 100 MHz serves as the Raman pump. Its emission is centered at a wavelength of $1.04 \mu\text{m}$, with a full width at half-maximum (FWHM) of 37 cm^{-1} after spectral filtering, and the pulses are chirped. Therefore, not all spectral components of the pump interact with the probe, leading to an improved spectral resolution. The pump beam is circularly

A configuration of a femtosecond pump and a picosecond Stokes lasers also works. In this case, Raman loss of the pump femtosecond comb is measured.

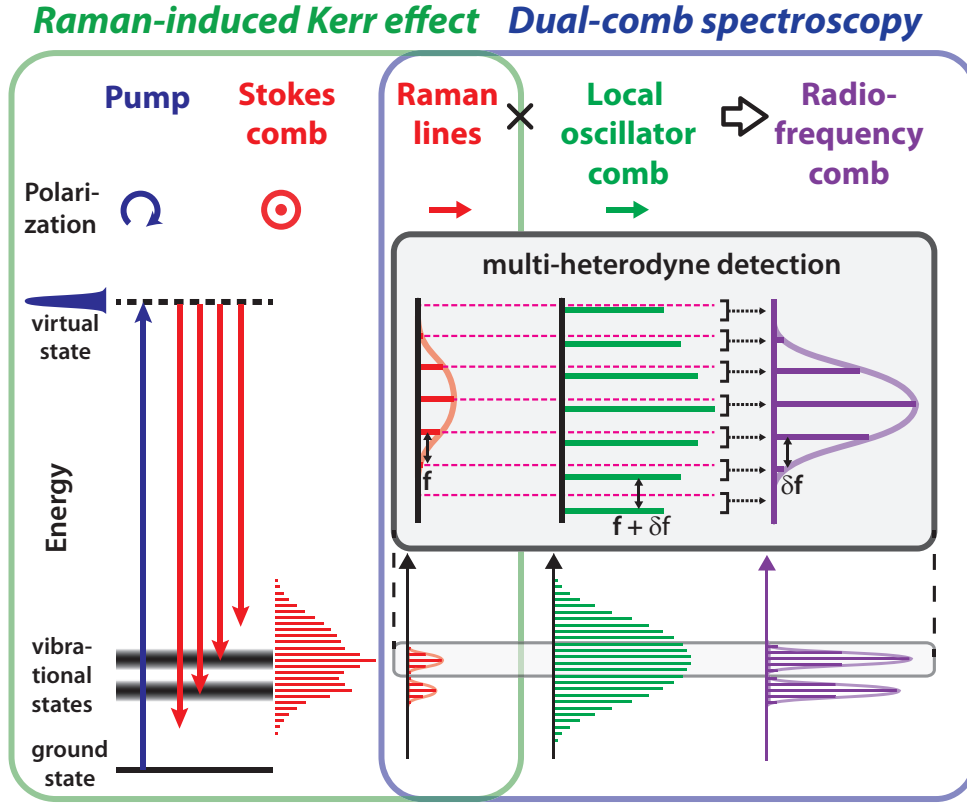


Figure 5.3: Conceptual description of the dual-comb RIKES.

polarized. The Stokes probe laser is a linearly polarized Er-doped fiber frequency comb emitting about 20 mW of average power and centered at $1.55 \mu\text{m}$ with an FWHM of 340 cm^{-1} . The pulse duration is about 60 fs. The repetition frequency of the Yb pump laser is actively synchronized to the Er comb using a scheme similar to the ones reported in [165–168] (details in 5.3.2). The output of the Er fiber oscillator is split to generate a pulse that is temporally overlapped with the Raman pump and a reference pulse used to measure the spectrum of the Stokes laser without pump. The two pulses are separated by about 250 ps. An infinity-corrected objective (20X Plan Apo NIR, Mitutoyo) focuses the pump (diameter: $6 \mu\text{m}$, Rayleigh length: $28 \mu\text{m}$) and Stokes beams (diameter: $7 \mu\text{m}$, Rayleigh length: $22 \mu\text{m}$) into a 1 mm thick cuvette containing the liquid sample. The positions of the focal points of the pump and Stokes beams are located about $40 \mu\text{m}$ apart due to chromatic aberrations of the microscope objective, and this reduces the efficiency of the stimulated Raman process. At the sample, the pump and Stokes beams have an average power of 960 mW (energy of 9.6 nJ) and 1.9 mW (energy of 9.5 pJ), respectively. After recollimation of the beams, the pump light is rejected by a long-wavelength-pass optical

filter. A cross-polarizer is aligned to block the Stokes beam in the absence of a pump. The optical birefringence induced in the initially isotropic medium by the anisotropic Raman resonant third-order polarization enables transmission of the background-reduced comb of Raman resonances. The extinction ratio of the Stokes probe through the entire optical setup is 10^{-4} , mostly limited by the microscope objectives and the sample cell. A second femtosecond Er-fiber comb, with a repetition frequency detuned by 301 Hz and an average output power of 20mW, optically samples the trains of pulses transmitted by the polarizer. It is filtered to 150 cm^{-1} to limit the spectral range in this proof-of-principle experiment to the stimulation of Raman signals with shifts around 3000 cm^{-1} , i.e., in the C-H stretch region. The amplitude of this local oscillator for multiheterodyne detection is controlled by the combination of a half-wave plate and a polarizing beam splitter to optimize the signal-to-noise ratio in the interferogram. The time-domain interference signal is monitored with a balanced InGaAs photodetector (PDB150C-AC, Thorlabs), which collects the two outputs of the interferometer. The balanced detection reduces intensity noise of the local oscillator [169, 170]. After electronic filtering, the interferometric pattern only contains the Raman gain signal, allowing for efficient amplification. The dynamic range issues associated with dual-comb spectroscopy are therefore partially overcome. Two interferograms, time-delayed by $83 \mu\text{s}$, are sequentially sampled at 100 MSamples/s by a 14 bit data acquisition board. Their complex Fourier transform reveals the phase and amplitude spectra in the presence and absence of the pump laser. Calibration of the wavenumber scale is achieved with the help of an optical spectrum analyzer. The ratio of the spectra with and without pump simultaneously provides the Raman gain spectrum of the dispersive (real part) and resonant (imaginary part) tensor elements of the third-order nonlinear susceptibility, similar to other techniques of heterodyne RIKE [163].

5.3.1 Yb fiber laser and power amplifier (Pump laser)

A commercial Yb-doped fiber oscillator (Orange, Menlo Systems) emits a femtosecond pulse train at a repetition rate of 100 MHz with an average power of 100 mW. The spectral span is about 80 nm centered at 1030 nm. The pulses emitted by the oscillator are coupled into a 3 m long stretcher fiber (HNDS1582BA-4-2-2, Sumitomo Electric) to be stretched to 15 ps. The stretched pulses go through an isolator for protection of the stretcher fiber and the oscillator against back-reflections, and injected into a 1.8 m long Yb-doped double-clad polarization maintained fiber (DC-200/40-Pz-Yb-01, NKT Photonics). The Yb-doped fiber is pumped in the backward configuration by a powerful laser diode at 976

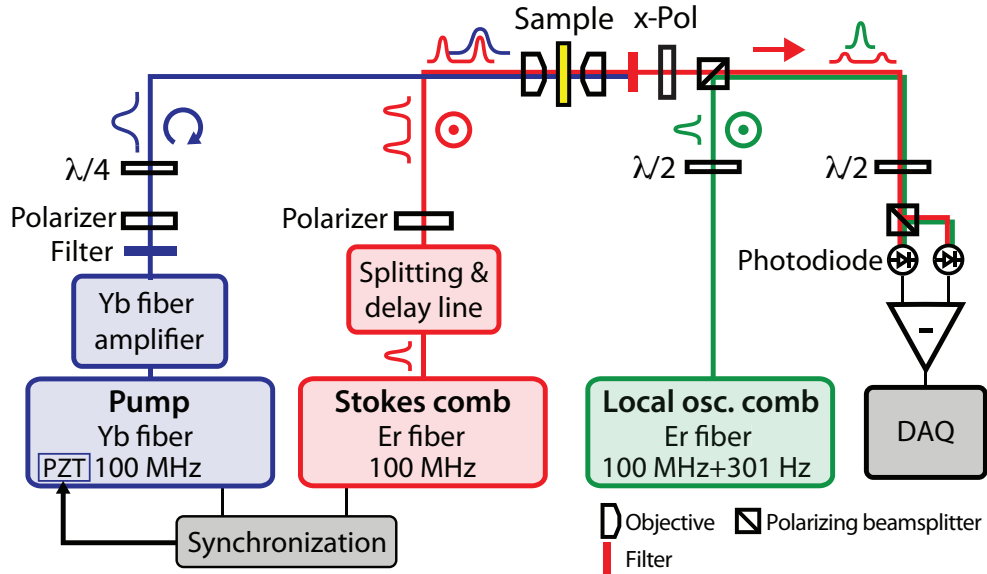


Figure 5.4: Experimental setup of dual-comb RIKES.

nm (JENA). Maximum pump power is about 75 W which amplifies the beam up to 14 W after compressing optics. This home-made power amplifier system is the same as that used in [70].

5.3.2 Synchronization of the pump and Stokes lasers

In order to synchronize the pump and Stokes pulse trains in time, an all-electronic synchronization scheme is implemented. The scheme is similar to the ones described in the literature [165–168]. The system consists of two phase detectors which provide coarse and fine synchronization. The coarse synchronization provides large delay tuning-range but poor stability. The fine synchronization provides short delay tuning-range but high stability. The synchronization follows two steps: first, coarse synchronization of the two pulse trains with the coarse phase detector, and second, tight synchronization with the fine phase detector. Figure 5.5 depicts the scheme. The pulse train emitted from the Yb-doped fiber laser (Pump laser) is detected by a 10 GHz bandwidth InGaAs fast photodiode (UPD35-IR2-P, ALPHALAS). The detector generates a radio frequency signal which contains frequency components at the repetition frequency of 100 MHz and at its harmonic frequencies within the bandwidth of the detector. The filtered fundamental repetition frequency at 100 MHz is sent into the coarse phase detector and the filtered 100th harmonic frequency signal at 10 GHz is sent into the fine phase detector. Exactly the same

procedure is applied to the Er fiber laser (Stokes laser). The phase detectors are analog double-balanced mixers, which generates the phase-error signals between the two input signals at radio-frequency. The error signals are sent into a potentiometer so that one can smoothly switch the error signals from coarse to fine. The selected phase error goes into a loop gain and the amplified signal is fed back to the piezo electric transducer on a cavity mirror of the Yb-doped fiber laser. An electric phase shifter is inserted in one of the signal line which is compared with the phase detector and controls the electrical delay between the signals to synchronize the pulse timing. If a 360 degree phase shifter is used, the delay tuning-range is 10 ns with the 100 MHz signal, and 100 ps with the 10 GHz signal. On the other hand, the sensitivity of the error signals to phase mismatch is 100 times better with the 10 GHz signal than the 100 MHz signal.

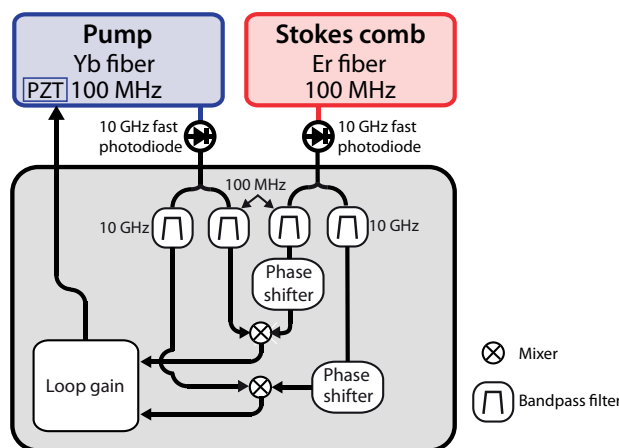


Figure 5.5: Schematics of synchronization between pump and Stokes pulse trains. PD: Photodiode.

Characterization of the synchronization

In order to characterize the synchronization, sum frequency generation (SFG) between the pump and Stokes pulses are used as an indicator of the space- and time-overlap. The synchronized pulses are focused onto a BBO crystal and the SFG radiation around 620 nm is detected by a Si photodiode. Figure.5.6(a) shows the intensity of the SFG radiation as a function of the delay between the pump and Stokes pulses. Since the pulse duration of the pump is 1.06 ps, which is much longer than 60 fs of the Stokes pulse, the intensity trace mimics the envelope of the pump pulse. To evaluate the timing jitter, the delay is set to the position which generates half the intensity of the maximum SFG and the fluctuation of the

signal is measured. Then, multiplying the slope factor, which is evaluated by the intensity trace of figure.5.6(a), shows the timing jitter. Putting a lowpass filter before sampling sets the upper limit of frequency of the jitter. The measured timing jitter is 26.8 fs with a 1 MHz lowpass filter (Figure.5.6(b)), and 12.0 fs with a 160 Hz lowpass filter (Figure.5.6(c)). Compared to 1.06 ps duration of the pump laser, this amount of timing jitter does not affect significantly the intensity of stimulated Raman scattering.

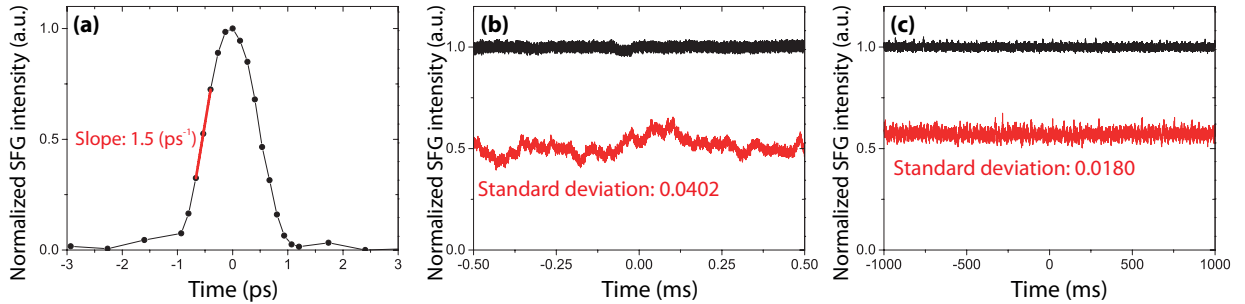


Figure 5.6: Characterization of the synchronization between the pump and Stokes pulses. (a) Normalized SFG intensity as a function of the delay between the pump and Stokes pulses. The red line is a linear fit around full width at half maximum (FWHM) of the curve. The slope is 1.5 ps^{-1} . (b) Residual instability of the synchronization with a 1 MHz lowpass filter over 1 ms. Standard deviation of the fluctuation is 0.0402, which corresponds to 26.8 fs root mean square (RMS) jitter. The black curve shows the intensity fluctuation at the SFG maximum. (c) Residual instability of the synchronization with a 160 Hz lowpass filter over 1 s. Standard deviation of the fluctuation is 0.0180, which corresponds to 12.0 fs RMS jitter.

5.4 Results and discussion

Two liquid samples are measured with the dual-comb RIKES experiment. In this proof-of-principle experiment, the target vibrational modes are aromatic C-H stretches around 3000 cm^{-1} . The first sample is neat Benzonitrile. An interferogram is measured within $2.93 \mu\text{s}$, which corresponds to a resolution of 6.7 cm^{-1} and 23 spectral elements, and the acquisition rate of the interferograms is the difference in repetition frequency of the two erbium lasers, 301 Hz, chosen according to the free spectral range span and the comb line spacing. To get a reasonable signal-to-noise ratio, one hundred interferograms are averaged, resulting in an effective measurement time of $293 \mu\text{s}$ and a total experimental time of 332 ms. Averaging and Fourier transforming may be accomplished in real time with the use

of field-programmable gate arrays. Figure.5.7(a) displays a portion of the amplitude and phase spectra of neat benzonitrile around 3100 cm^{-1} . The observed linewidth (about 27.5 cm^{-1}) of the band is narrower than the width of the Raman pump laser, as the pulses of the latter are chirped. In this spectrum, the stimulated Raman gain experienced by the Stokes beam at the sample is 10^{-5} and the relative noise level is 10^{-6} .

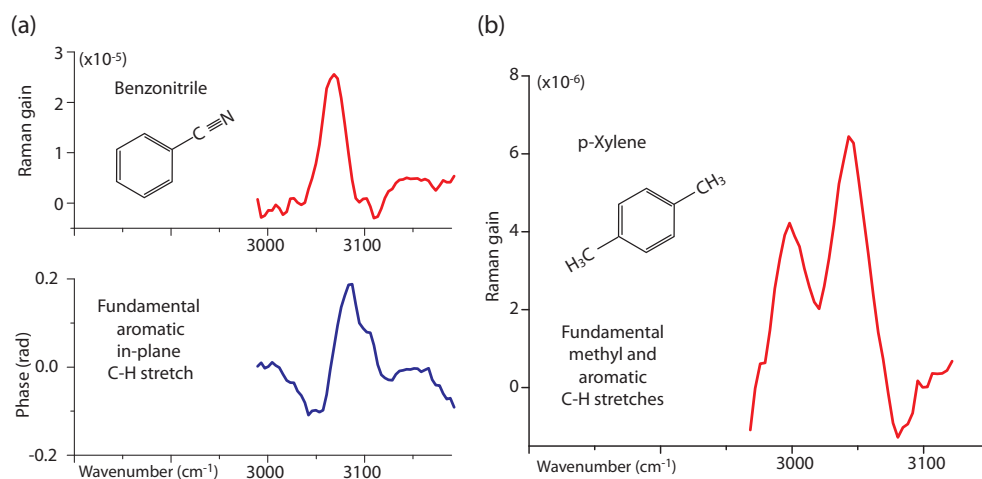


Figure 5.7: (a) Experimental Raman gain amplitude and phase spectra of benzonitrile. (b) Experimental Raman gain spectrum of p-Xylene.

The weaker bands of p-Xylene (Figure.5.7(b)) are recorded with the same experimental setup. 1062 interferograms, each measured within $2.99\text{ }\mu\text{s}$, are averaged, leading to an effective measurement time of 3.2 ms and an experimental time of 3.5 s. The noise level in our experiment already represents an excellent figure for real-time femtosecond stimulated Raman spectroscopy. Differential detection of the interferometric signal in the radio frequency domain is one of the causes that lead to such results. Sensitivities better than 10^{-8} have been reported in video-rate imaging [152] with lock-in detection, but these only allow for multiplex detection of three spectral elements, whereas dual-comb RIKES potentially allows for broad spans and high resolution. Most femtosecond stimulated Raman experiments (e.g., [161]) use complex amplified laser systems with kilohertz-to-hertz repetition frequencies and long measurement times, although promising alternatives with MHz systems have already been demonstrated [157]. Our low-intensity setup and our very short measurement time contribute in opening intriguing opportunities for real-time spectrally resolved Raman chemical labeling. Significant sensitivity improvement of our experiment could be achieved through a better spatial overlap between the pump and Stokes beams,

either with reflective objectives or with laser systems that emit in spectral regions (e.g., 800 nm) where microscopy instrumentation is more advanced.

Pump polarization dependence

Since the cross-polarizer does not reject the Stokes beam entirely in the condition of absence of the pump beam, the Stokes beam leaks through the polarizer. As a consequence, what is heterodyned with the local oscillator field is summation of the Raman field and the leaked Stokes field. This is the reason why one has to take spectra with and without the pump beam and compare them to get the Raman gain. Since the phase of the RIKES field is determined by the polarization of the pump beam (right or left circularly polarized beams), the sign of the Raman gain (loss) can be changed. Here, the Raman gain (loss) means positive (negative) variation with respect to the spectrum without pump. The Figure.5.8 clearly shows that the right and left circularly polarized pump beam induces the RIKES field with 180 degree phase difference, and the linearly polarized pump along with the Stokes polarization doesn't induce any RIKES field at all. The dependence supports that the observed line is not an artifact.

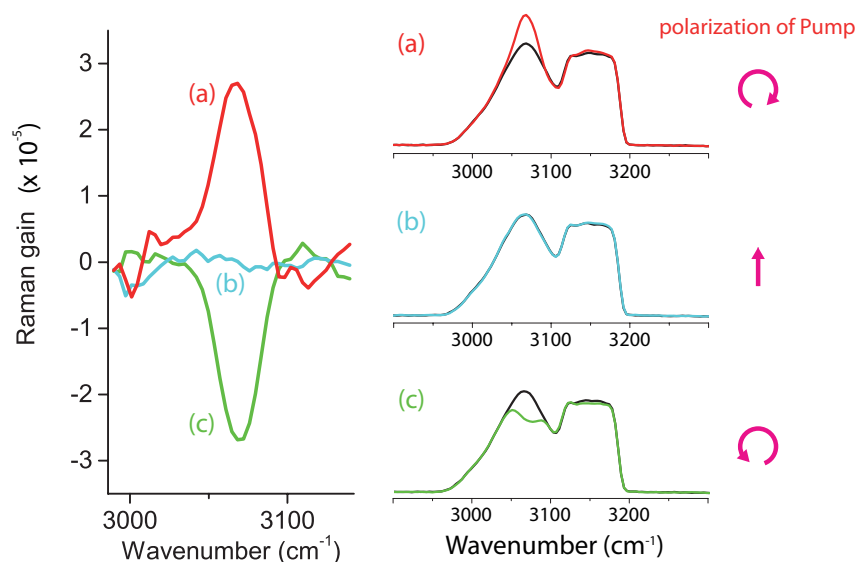


Figure 5.8: (Left-hand side) RIKES gain (loss) when the pump beam polarization is as described in the right column. (Right-hand side) Spectra with and without the pump at the polarization of (a)right circle, (b)linear, (c)left circle. Black curve shows the spectra without pump.

5.5 Conclusion

This chapter demonstrated Raman-induced Kerr-effect dual-comb spectroscopy. This was the first demonstration of nonlinear dual-comb spectroscopy as well as the first Raman dual-comb spectroscopy. The nonlinear Raman spectra over 150 cm^{-1} around 3100 cm^{-1} was measured within $2.93\text{ }\mu\text{s}$ and a C-H stretching Raman signal in Benzonitrile was observed with a spectral resolution of 27.5 cm^{-1} . Averaging over 100 spectra, effective measurement time of $293\text{ }\mu\text{s}$ (experimental measurement time of 332 ms), clearly displayed the Raman gain and its dispersive phase spectrum. The observed Raman gain experienced by the sample was estimated to 10^{-5} , and the relative noise level was 10^{-6} . The weaker bands of p-Xylene was also measured with averaging of 1062 spectra within 3.2 ms of effective measurement time (experimental measurement time of 3.5 s). Two Raman gain peaks of fundamental methyl and aromatic C-H stretches were clearly observed. The polarization dependence of pump laser confirmed the results that these peaks were not artifacts but the Raman gain signals.

Chapter 6

Coherent anti-Stokes Raman dual-comb spectroscopy and microscopy

6.1 Background

6.1.1 Coherent anti-Stokes Raman spectroscopy

Coherent anti-Stokes Raman scattering (CARS) is a third order nonlinear optical process [146]. As shown in Figure.6.1, a pump and a Stokes fields with frequencies f_p and f_S , respectively, excite a molecular vibrational coherence and a probe field with frequency f_{pr} , reads out the coherence by generating a blue-shifted anti-Stokes field at frequency f_{AS} . In this parametric process, the photon energy (frequency) difference between the pump and Stokes light is transferred to the scattered anti-Stokes light, so that the blue-shifted energy (frequency) from that of probe light indicates the molecular vibrational energy (frequency). Since the blue-shifted frequency of the anti-Stokes light can be apart from the frequency of the pump, Stokes and probe light, a proper optical filtering makes the process background-free. The induced polarization P_{CARS} may be written:

$$P_{CARS} = (\chi_R^{(3)} + \chi_{NR}^{(3)})E_p E_S^* E_{pr} \quad (6.1)$$

The contents in this chapter is published in [60]

where $\chi_R^{(3)}$ and $\chi_{NR}^{(3)}$ are the third-order nonlinear susceptibility of the resonant part and the non-resonant part, E_p , E_S , E_{pr} are the electric field of the pump, Stokes and probe light. The intensity of the CARS signal I_{CARS} is proportional to the square modulus of the polarization:

$$I_{CARS} \propto |P_{CARS}|^2 = (|\chi_R^{(3)}|^2 + |\chi_{NR}^{(3)}|^2 + 2\chi_{NR}^{(3)}\text{Re}[\chi_R^{(3)}])I_p I_S I_{pr} \quad (6.2)$$

Where I_p , I_S , I_{pr} are the intensity of the pump, Stokes and probe light. As a consequence, the CARS intensity has a cubic dependence on the total input light intensity. Also, since the susceptibility is proportional to the number of molecules, the CARS intensity has a square dependence on the concentration of the sample molecules.

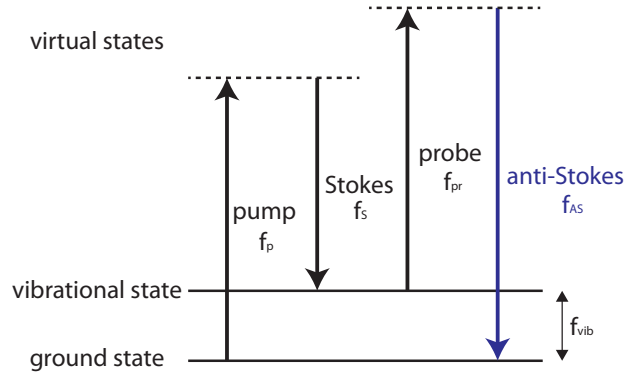


Figure 6.1: Energy diagram of CARS process.

Non-resonant background

As it appears in Equation.6.2, the non-resonant processes play a significant role in the CARS. These are four-wave-mixing parametric processes shown in Figure.6.2. Since these processes are due to the electronic motion mediated through virtual states, these are instantaneous phenomena. The non-resonant fields are detected interferometrically with the resonant CARS field and this makes the observed CARS spectrum distorted in a dispersive way. This spectral distortion is always cumbersome in most of the applications of CARS and requires complicated analysis. Moreover, the non-resonant signal adds broadband noise and decreases the sensitivity of CARS measurements.

In the last decade, many kind of methods of CARS have been demonstrated aiming at suppressing the non-resonant background, including epi-detection CARS [171, 172], polarization CARS [173, 174], time-resolved CARS [175], interferometric/heterodyne CARS

[176–181], pulse-shaping CARS [182–185], phase-retrieval CARS [186, 187], and frequency modulation CARS [188, 189]. These methods are effective to suppress the non-resonant background at the expense of complexity of the instruments or the data-analysis.

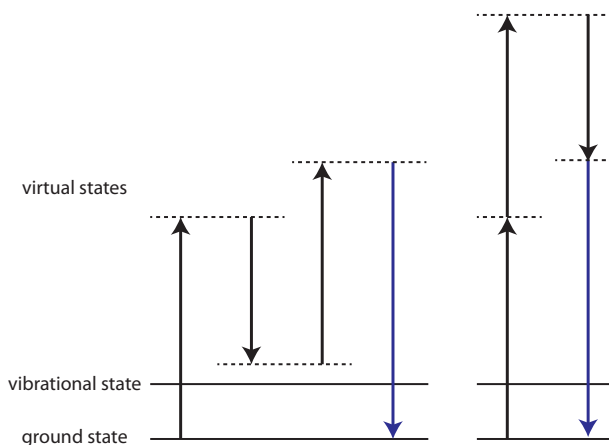


Figure 6.2: Energy diagram of non-resonant processes.

6.2 Principle

6.2.1 Impulsive stimulated Raman scattering

When an ultrashort laser pulse passes through almost any molecular sample, coherent vibrations are likely to be excited by impulsive stimulated Raman scattering (ISRS) [190, 191]. The criterion for the coherent excitation by a single pulse is that the pulse duration (τ_p) is shorter than the oscillation period (T_{vib}) of a single cycle of a molecular vibration. To put it in another way, the bandwidth of the pulse must be larger than the vibrational frequency (f_{vib}).

$$\tau_p < T_{vib} = 1/f_{vib}$$

Under such condition, the femtosecond pulse kicks the molecules and they start oscillating at their particular vibrational frequencies. These coherent oscillations can be monitored by ultrashort probe pulses with a varying time delay. If the duration of the probe pulse is also shorter than the oscillation periods, the vibrational oscillations can be clearly observed in time domain through some detection methods.

In the first ISRS demonstration, optical phonons in a α -perylene crystal up to 200 cm^{-1} were excited with a pulse which duration was less than 100 fs emitted from a colliding

pulse mode-locked (CPM) ring dye laser [192]. The phonon oscillations were monitored through scattering of the probe pulse by the transient-grating generated by crossed excitation pulses. The collinear geometry pump-probe scheme (Forward ISRS) was proposed [190] and demonstrated [193,194] afterwards. In this configuration, modulation of the spectrally dispersed probe pulses are detected. This pump-probe ISRS is the basic concept of the dual-comb CARS.

Since, nowadays, ultrafast lasers are readily available, molecular vibrations in the fingerprint region, where are lying at higher frequencies than the optical phonons, can be good targets for the impulsive excitation. For example, an ultrashort pulse of 20 fs duration can excite the molecular vibrations up to 1500 cm^{-1} , which covers the fingerprint region.

6.2.2 Fourier transform CARS

The concept of the Fourier transform CARS was proposed and demonstrated in 1985 [195]. Two different color picosecond pulses excite molecular vibrations and the delayed probe pulse is scattered off and generates the anti-Stokes radiation. The vibrational modulation was observed on the intensity of the anti-Stokes radiation and Fourier transform of the modulation reveals the Raman vibrational spectrum. The concept of Fourier transform CARS has been extended to a single femtosecond pulse excitation combined with a Michelson interferometer [175,196] or a pulse-shaping method [182] instead of two picosecond pulses excitation.

Theoretical description

Here, we follow the semiclassical description of Fourier transform CARS by femtosecond lasers discussed in the literature [197,198]. Following the third order perturbation theory, the resonant polarization $R_R^{(3)}$ created by a single femtosecond pulse with the electric field $E(\nu)$ may be written as a function of frequency ν :

$$P_R^{(3)}(\nu) \propto \int_0^\infty d\nu' \frac{1}{\nu' - f_{vib} - i\Gamma_{vib}} E(\nu - \nu') A(\nu') \quad (6.3)$$

$$A(\nu') = \int_0^\infty d\nu'' E^*(\nu'') E(\nu' + \nu'')$$

where f_{vib} and Γ_{vib} are the Raman vibrational frequency and its dephasing rate. The equation describes all the possible pair of frequencies which difference frequency is equal to the

vibrational mode induce the polarization. The nonresonant polarization may be described:

$$P_{NR}^{(3)}(\nu) \propto \int_0^\infty d\nu' \frac{E(\nu - \nu')A(\nu')}{\nu'} \quad (6.4)$$

The factor $1/\nu'$ is inserted by hand to reflect the fact that the finite pulse duration induces non-instantaneous response.

In femtosecond Fourier transform CARS, the electric field which induces the nonlinear polarization consists of two pulse fields $E_1(t)$ and $E_2(t - \tau)$ with delay τ :

$$E(\tau, t) = E_1(t) + E_2(t - \tau) \quad (6.5)$$

The third-order polarization induced by the field $E(\tau, t)$ is written:

$$\begin{aligned} P_{FT-CARS}(\tau, t) &= (\chi_R^{(3)} + \chi_{NR}^{(3)})E(\tau, t)E^*(\tau, t)E(\tau, t) \\ &= P_R^{(3)}(\tau, t) + P_{NR}^{(3)}(\tau, t) \end{aligned} \quad (6.6)$$

where $P_R^{(3)}(\tau, t)$ and $P_{NR}^{(3)}(\tau, t)$ are the Fourier transform of $P_R^{(3)}(\nu)$ and $P_{NR}^{(3)}(\nu)$ described in the Equation.6.3 and 6.4. The total FT-CARS signal is described as a function of delay τ :

$$S_{FT-CARS}(\tau) \propto \int_0^\infty dt |P_{FT-CARS}(\tau, t)|^2 \quad (6.7)$$

The polarization $P_{FT-CARS}(\tau, t)$ consists of a number of different processes. What we are interested in here are the processes which depend on the delay τ and those which interfere with them. Therefore, the processes we investigate can be described:

$$P_{FT-CARS}(\tau) \approx P_{R,1,2}^{(3)}(\tau) + P_{NR,1,2}^{(3)}(\tau) + P_{R,2}^{(3)} + P_{NR,2}^{(3)} \quad (6.8)$$

where the first term $P_{R,1,2}^{(3)}(\tau)$ represents the process where the pulse 1 excites the vibrational coherence and the pulse 2 probes it. This process corresponds to the pump-probe impulsive stimulated Raman scattering (Section.6.2.1). The second term $P_{NR,1,2}^{(3)}(\tau)$ represents the non-resonant processes both pulse 1 and 2 contribute to but the processes only happen when $\tau \approx 0$. This can be easily ignored by not looking at the signal at $\tau \approx 0$. The third and fourth terms $P_{R,2}^{(3)}$ and $P_{NR,2}^{(3)}$ represent the processes only pulse 2 contributes. These processes don't depend on the delay τ but may interfere with the the first term $P_{R,1,2}^{(3)}(\tau)$ because they are all generated at the same time. Note that we can ignore the processes

governed only by the pulse 1 because such induced polarizations don't interfere with the first term $P_{R,1,2}^{(3)}(\tau)$.

Finally, the modulated part of the FT-CARS signal which depends on the delay τ is described by:

$$\begin{aligned} S_{FT-CARS}(\tau) &\approx \text{Re}[P_{R,1,2}^{(3)*}(\tau)P_{R,1,2}^{(3)}(\tau) + P_{R,1,2}^{(3)*}(\tau)P_{R,2}^{(3)} + P_{R,1,2}^{(3)*}(\tau)P_{NR,2}^{(3)}] \\ &\propto \chi_R^{(3)2}I_1^2I_2 + \chi_R^{(3)2}I_1I_2^2 + \chi_R^{(3)}\chi_{NR}^{(3)}I_1I_2^2 \end{aligned} \quad (6.9)$$

where I_1 and I_2 are the intensity of the pulse 1 and 2. The three processes are detected at the same time. All of them share the feature that the pulse 1 excites the vibrational coherence and the pulse 2 probe it. The second and third terms are sort of heterodyne signals. The contribution of these processes depends on the sample and the condition of the pulses. If, for example, the sample generates strong non-resonant radiation, the third term may be the dominant process among them.

6.2.3 Dual-comb CARS

In the technique of dual-comb CARS, we harness two femtosecond lasers with repetition frequencies $f + \delta f$ and f to irradiate a sample. In the time domain (Figure. 6.3(a)), a pulse from the first laser coherently excites a molecular vibration of period $1/f_{vib}$ that is longer than the pulse duration and the coherently vibrating molecules give rise to an oscillating refractive index modulated at the vibrational frequency (ISRS process) (Figure.6.3(b)). A pulse of the second laser probes the sample with a time separation Δt that increases linearly from pulse pair to pulse pair. If this second pulse (for simplicity also taken to be short compared with the molecular vibration period) arrives after a full molecular period $1/f_{vib}$, the vibration amplitude is increased and the back-action on the probe pulse is a spectral shift towards lower frequencies (Coherent Stokes Raman scattering, CSRS). If it arrives after half a period, the vibration amplitude is damped and the pulse experiences a shift towards higher frequencies (Coherent anti-Stokes Raman scattering, CARS). As long as the pulse separation Δt remains shorter than the coherence time of the molecular oscillation, an intensity modulation of frequency $f_{vib}\delta f/f$ is thus observed in the transmitted probe radiation after a spectral edge filter. The two femtosecond lasers have a symmetrical function: the sign of time separation Δt between the pulses changes every $1/(2\delta f)$. In the frequency domain (Figure.6.3(c),(d)), the two frequency comb generators produce an

optical spectrum consisting of several hundred thousand perfectly evenly spaced spectral lines. Their frequencies may be described by

$$\begin{aligned} f_m^{(1)} &= m(f + \delta f) + f_{ceo} \\ f_{m'}^{(2)} &= m'f + f'_{ceo} \end{aligned}$$

where m and m' are integers, and f_{ceo} and f'_{ceo} are the carrier-envelope offset frequencies. The frequency differences within each comb form regular combs themselves with vanishing carrier-envelope offset frequencies and line spacings of $f + \delta f$ and f , respectively. For instance, for comb 1 all pairs of lines with $m - n = k$ contribute to the same difference frequency $k(f + \delta f)$. Each of the difference frequency combs resonantly excites a molecular level of frequency f_{vib} by means of Raman-like two-photon excitation whenever a difference frequency comes close to f_{vib} ; that is, when $k \approx f_{vib}/f$. The excitations by the two combs interfere and modulate the molecular vibration at a beat note frequency $k\delta f = f_{vib}\delta f/f$. The two-photon excitation leads to a resonant enhancement of the third order nonlinear susceptibility observed by means of the anti-Stokes radiation. The intensity of the generated broadband anti-Stokes radiation is modulated at the beat note frequency $f_{vib}\delta f/f$. When several vibrational levels ($f_{vib1}, f_{vib2}, \dots$) are excited, the composite modulation contains all the beating frequencies ($f_{vib1}\delta f/f, f_{vib2}\delta f/f, \dots$) representative of the involved levels. The Raman excitation spectrum is revealed by Fourier transformation of the intensity recorded against time. The spectrum is mapped in the radio frequency domain by the downconversion factor $\delta f/f$ (typically of the order of 10^{-7} to 10^{-6}). This permits rapid measurement time and efficient signal processing. Absolute calibration of the Raman shifts is achieved by dividing the radio frequencies by the downconversion factor, which is easy to measure accurately. The carrier-envelope offsets cancel and do not have to be measured or controlled. This notably simplifies the experimental implementation and the calibration procedure. Similar modulation transfer phenomena have been exploited in experiments using a single femtosecond laser and a phase-modulation pulse shaper [182] or a Michelson interferometer [175, 196, 199], but measurement times were fundamentally limited either by the sweep period of the phase modulation or by the mechanical motion in the Michelson interferometer. Our motionless frequency comb-based technique enables more than 1000-fold shorter acquisition times, and a spectral resolution and spectral span only limited by the measurement time and the spectral bandwidth of the femtosecond lasers.

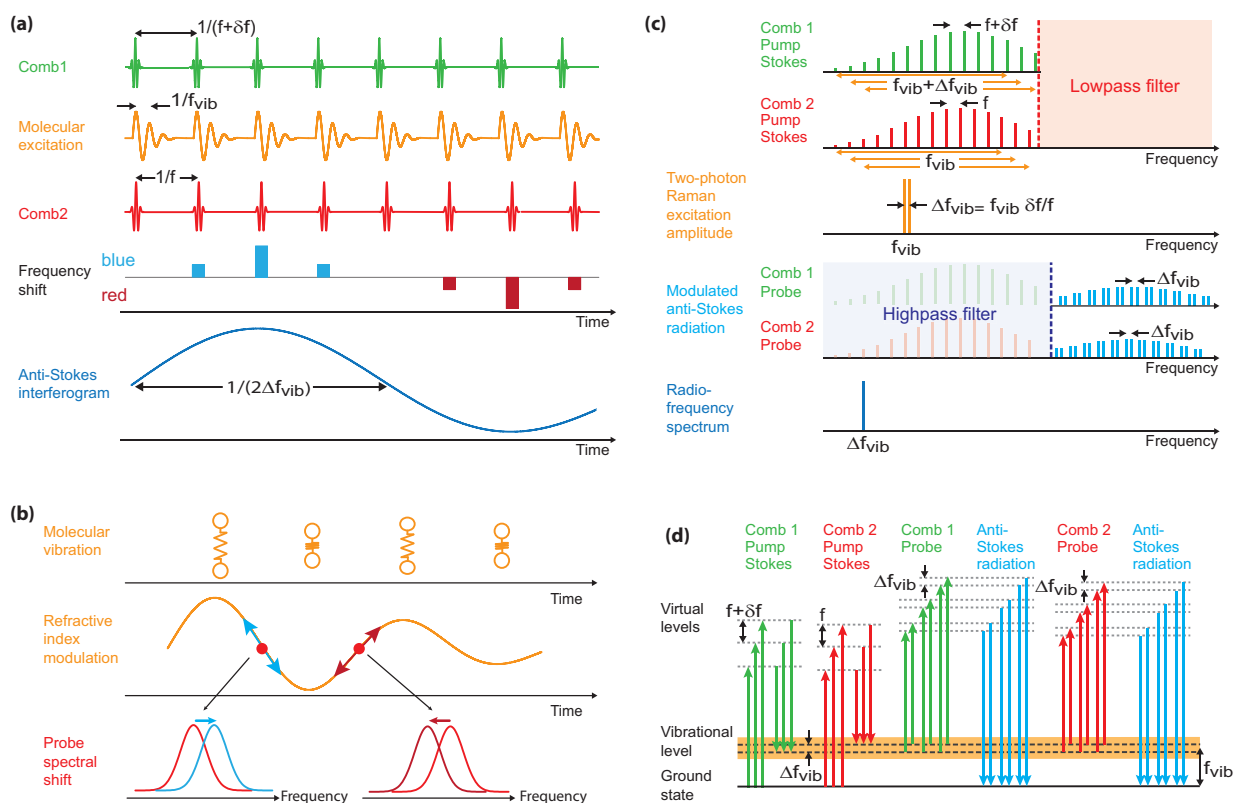


Figure 6.3: Principle of dual-comb CARS. Δf_{vib} stands for $f_{vib}\delta f/f$. (a) Time-domain representation in the limit of a molecular decoherence time that is shorter than the time interval between two laser pulses. The train of pulses of laser frequency comb 1 periodically excites the molecular vibration, which is probed by the pulses of laser frequency comb 2 with a linearly increasing time delay. The resulting filtered anti-Stokes radiation provides the interferogram. The two combs have a symmetric function. In the figure, only the situation in which the delay between the pulses of comb 2 and those of comb 1 is positive is displayed. (b) When the probe pulse is short compared with the molecular oscillation (impulsive stimulated Raman scattering), the refractive index modulation of the sample-induced by the pump and Stokes beam-shifts the probe spectrum alternatively towards lower and higher frequencies. (c) Frequency-domain representation in the limit of a comb line spacing that is larger than the resonant Raman excitation bandwidth. The two frequency combs modulate the excitation amplitude of the molecular vibration with a frequency Δf_{vib} . This modulation is then transferred by the combs to the anti-Stokes radiation. For simplicity, the Raman excitations are represented as narrow lines. (d) Energy-level diagram, illustrating the four-wave mixing that leads to intensity-modulated anti-Stokes radiation.

6.3 Spectroscopy

6.3.1 Experimental setup

Figure 6.4 sketches the experimental setup, which is similar to that used in dual-comb absorption spectroscopy except for dispersion management and spectral filtering to isolate the CARS signal from the comb beams. As the Raman-like two-photon excitation involves virtual energy levels, dispersion decreases both the spectral span and the excitation efficiency. Two titanium-sapphire lasers (Synergy20 UHP; Femtolasers) emit 20 fs pulses centred at 12580 cm^{-1} (795 nm) with energies up to 13 nJ. Titanium-sapphire lasers are chosen because of their capabilities to generate ultra-short pulses in a spectral region where most samples have no or only weak absorption and where advanced photonics tools are available. Both oscillators have repetition frequencies of about 100 MHz, which can be adjusted by moving a cavity mirror mounted on a motorized translation stage and a piezoelectric transducer. The repetition frequencies are monitored with fast silicon photodiodes connected to frequency counters (53131A; Agilent). To prevent long-term drifts, the repetition frequency of each laser comb is stabilized against a radiofrequency clock by means of a mirror of the laser's cavity mounted on a piezoelectric transducer. This does not affect the quality of an individual spectrum but improves the reproducibility of the wavenumber scale of a sequence of spectra. The laser beams are linearly polarized. The pulse energy available for the spectroscopy experiments is adjusted for each laser beam individually with a combination of a half-wave plate and a polarizer. The beams of the two lasers are combined on a pellicle beamsplitter, and a chirped mirror compressor (Layertec) compensates for the second-order dispersion induced by the optical components of the setup. Spectral filtering is applied to improve the signal-to-background ratio. A low-frequency-pass optical filter (ET750LP, cutoff 13330 cm^{-1} (750 nm); Chroma Technology) before the sample and a high-frequency-pass optical filter (3RD740SP, cutoff 13510 cm^{-1} (740 nm); Omega Optical Inc.) after the sample isolate the CARS signal that is generated by the sample after proper focusing with a lens or a microscope objective. The spectral span is thus limited on the low-energy side by the optical filters and on the high-energy side by the spectral bandwidth of the femtosecond lasers. The anti-Stokes radiation is forward-collected and focused on a single silicon photodiode with a frequency bandwidth of the order of 100 MHz. The electric signal is low-pass filtered to 50 MHz to avoid aliasing. The non-interferometric signal, which occurs at the pulse repetition frequency, is also filtered out. This non-interferometric signal (CARS and non-resonant signal within a sin-

gle laser pulse) is the main source of undesired background. The interferometric signal is then amplified with a wideband variable-gain voltage amplifier (DHPVA-100; FEMTO Messtechnik GmbH) and digitized with a 16-bit data acquisition board (1.8×10^8 samples s^{-1} , ATS9462; AlazarTech). Apodization and Fourier transformation may be accomplished in real time with the use of field-programmable gate arrays or a posteriori with a basic desktop computer.

The data of Figure.6.5(a) were recorded with orthogonal linear polarizations of the two laser beams. This decreased the interferometric non-resonant background, while the fast depolarization of the sample maintained the strength of the anti-Stokes signal. For the spectra of Figure.6.5(b),(c), the focusing optics consisted of lenses with a focal length of 20 mm and required an amount of dispersion compensation of -600 fs^2 . The pulse energy at the sample was 3 nJ. The spectrum of Figure.6.5(d) was measured with a focusing lens with a focal length of 8 mm, a pulse energy of 0.5 nJ and an avalanche photodetector (APD Module C4777; Hamamatsu).

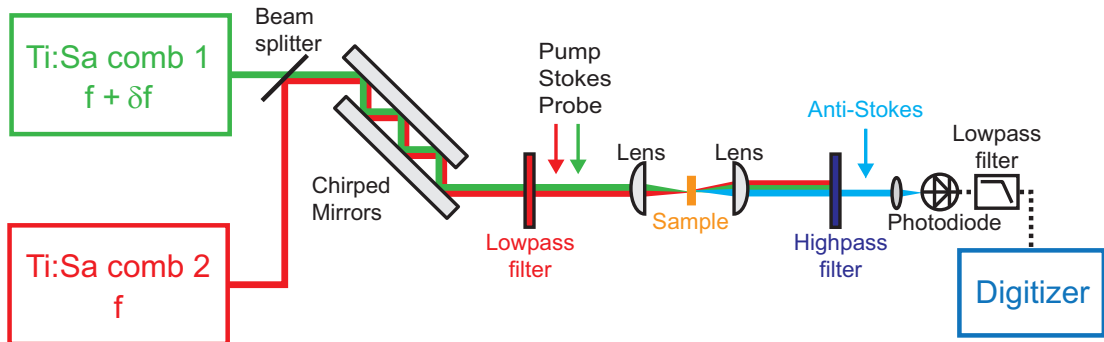


Figure 6.4: Experimental setup of CARS spectroscopy.

6.3.2 Recording parameters

In the experiments of coherent anti-Stokes Raman spectroscopy with two laser frequency combs, the vibrational levels that are excited in a Raman two-photon process have an energy f_{vib} that matches a frequency difference between pairs of lines of one comb. The vibration is modulated by the interference between the excitation by the two combs and is thus downconverted to the frequency $f_{vib}\delta f/f$. The energy $f_{vib,max}$ (in hertz) of the higher-lying vibrational level that can be observed is about the spectral bandwidth of the combs ΔF (in hertz), roughly twice the full width at half-maximum of the laser spectrum:

$$f_{vib,max} = \Delta F$$

The difference δf in repetition frequencies between the two lasers must be adjusted to image the domain $0 - \Delta F$ into a radio frequency free spectral range of $0 - f/2$ at most. Thus, to avoid aliasing, one has to choose $\delta f \leq f^2/(2\Delta F)$. For the faster recording times, δf should be chosen equal to $f^2/(2\Delta F)$. However, for signal-to-noise ratio improvement, it may be advantageous to set δf to a lower value, as illustrated in Figure.6.5(c), (d). The Fourier transform of the interferometric signal provides a radiofrequency spectrum with a free spectral range equal to $\Delta F\delta f/f$ (and less than or equal to $f/2$). The Raman-shift scale is retrieved by dividing the measured radiofrequency scale by the downconversion factor $\delta f/f$. The resolution $\delta\nu_{rf}$ (in hertz) in the radio frequency domain, in a magnitude spectrum with triangular apodization, is given by the inverse of the measurement time T :

$$\delta\nu_{rf} = 1.8/T$$

The optical resolution $\delta\nu_{opt}$ (in hertz) of the Raman spectrum is retrieved by dividing the radiofrequency resolution $\delta\nu_{rf}$ by the downconversion factor $\delta f/f$:

$$\delta\nu_{opt} = 1.8f/(\delta fT)$$

The instrumental resolution is fundamentally limited by the line spacing f of the comb. For most mode-locked lasers the line spacing is within the range 50 MHz to 1 GHz. Thus this limitation is not an issue in most liquid-phase studies, because the width of the vibrational bands is generally broader than 100 GHz (3.3 cm^{-1}). It is, however, possible to improve the resolution by interleaving successively acquired spectra recorded with slightly different radio frequency line spacings. The difference δf in repetition frequencies between the two lasers also determines the interferogram refresh rate. Every $1/\delta f$ the pulse train of one laser scans the entire pulse period of the second laser comb to generate a single interferogram, which is afterwards time-windowed to provide the desired resolution. This refresh rate limits the speed of successive acquisitions and thus is currently the main limitation for fast hyperspectral imaging experiments. A detailed discussion in Section.6.5 elaborates on this difficulty and shows that frequency combs of a relatively large line spacing (1 GHz) hold promise to overcome it. In our experiment we use lasers with a repetition frequency of about $f = 100 \text{ MHz}$. When the difference of repetition frequencies of the two lasers is set to $\delta f = 100 \text{ Hz}$, the downconversion factor $\delta f/f$ is 10^{-6} . The radiofrequency free-spectral range is 50 MHz and the optical free spectral range ΔF is 50 THz (1668 cm^{-1}). Recording

time of 15 μs leads to a radiofrequency resolution $\delta\nu_{rf}$ of 120 kHz, which converts to an optical resolution $\delta\nu_{opt}$ of 120 GHz (4 cm^{-1}). The refresh time of the interferograms is 10 ms.

6.3.3 Results and discussion

The time-domain interference signal -the interferogram- is periodic. Every $1/\delta f$, a strong burst mostly contains the non-resonant four-wave mixing signal resulting from the interference between the overlapping pulses of the two combs. A reproducible modulation (Figure. 6.5(a)), due to the CARS signal only, follows the burst and has a duration proportional to the coherence time of the sample transitions. A time-windowed portion of the interferogram, which excludes the interferometric non-resonant contribution, is Fourier transformed. The width of the window is chosen according to the desired spectral resolution. The resulting spectra (Figure.6.5(b)-(d)) span Raman shifts from 200 cm^{-1} to 1400 cm^{-1} . The non-resonant background, which strongly lowers the sensitivity of CARS, is entirely suppressed, as in other specific CARS schemes [175, 182, 196, 199]. We illustrate acquisition times with three spectra at an apodized resolution of 4 cm^{-1} and recorded with $\delta f = 100\text{ Hz}$ (Figure.6.5(b)) or 5 Hz (Figure.6.5(c),(d)) for a mixture of hexafluorobenzene, nitrobenzene, nitromethane and toluene in a cuvette 5 mm long. The spectra involve no averaging and were measured in 14.8 μs (Figure.6.5(b)) and 295.5 μs (Figure.6.5(c),(d)); the number of individual spectral elements (defined as the spectral span divided by the resolution) for all three spectra is 300. The signal-to-noise ratio culminates at 1000 for the most intense blended line of toluene and nitrobenzene in Figure.6.5(c). Recorded under different experimental conditions, the three spectra show great similarities in line position and relative intensity.

Comparison with the other techniques

The achievements of the several relevant spectroscopic techniques are shown in the Table.6.1. A significant point of this work is achieving very good values for all the measurement-parameters including spectral span, resolution, number of spectral elements, measurement time and signal-to-noise ratio. Compared to the work [200], which achieves fast and broadband CARS, the dual-comb CARS acquires 3.75 times more spectral elements with 21 times better signal-to-noise ratio in 1000 times shorter measurement time.

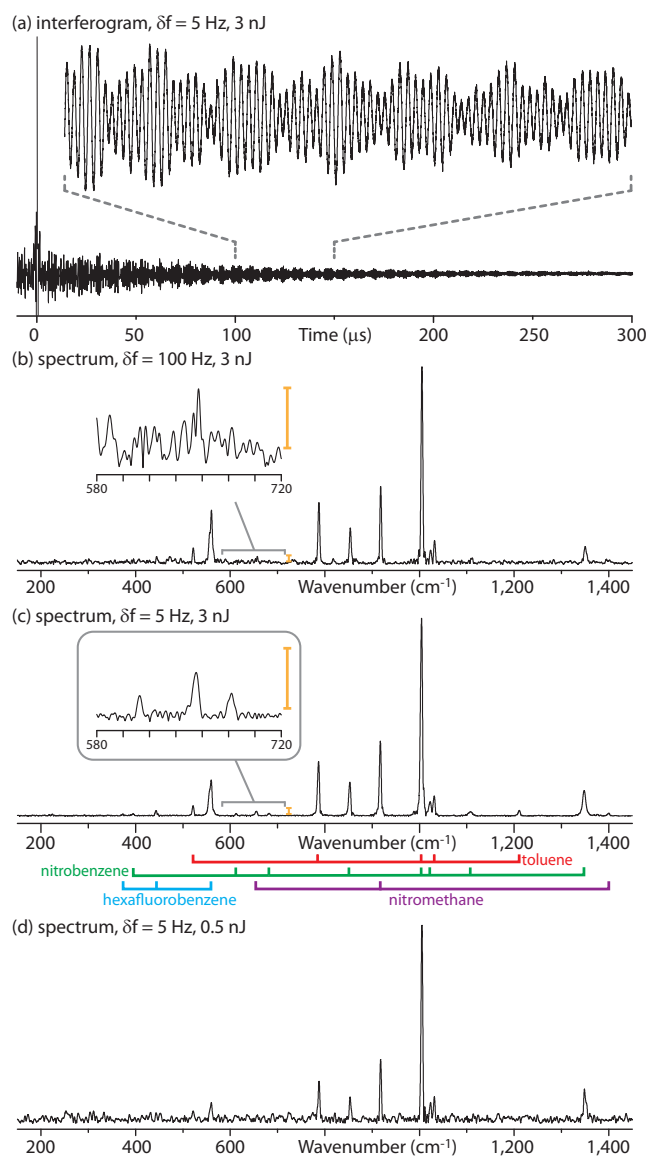


Figure 6.5: High-resolution dual-comb CARS of a mixture of liquid chemicals. (a) Unaveraged interferogram showing the non-resonant interference signal around the zero time delay and the interferometric modulation of the vibrational transitions shown in (c) ($\delta f = 5$ Hz; energy per pulse 3 nJ). (b) Dual-comb CARS unaveraged spectrum ($\delta f = 100$ Hz; measurement time $14.8 \mu\text{s}$; apodized resolution 4 cm^{-1} ; energy per pulse 3 nJ). (c) Dual-comb CARS unaveraged spectrum ($\delta f = 5$ Hz; measurement time $295.5 \mu\text{s}$; apodized resolution 4 cm^{-1} ; energy per pulse 3 nJ). (d) Dual-comb CARS unaveraged spectrum ($\delta f = 5$ Hz; measurement time $295.5 \mu\text{s}$; apodized resolution 4 cm^{-1} ; energy per pulse 0.5 nJ). The insets in (b) and (c) magnify the vertical scale tenfold.

Reference	Spectral span (cm^{-1})	Resolution (cm^{-1})	Number of spectral elements	Measurement time	SNR
This work, Fig.3(b)	1200	4	300	14.8 μs (dc: 3×10^{-3})	210
This work, Fig.3(c)	1200	4	300	285.5 μs (dc: 3×10^{-3})	1000
[201]	300	6	50	4 s	800
[200]	400	5	80	20 ms	~ 10
[202]	800	20	40	$\geq 80\text{s}$	~ 50

Table 6.1: Comparison of the achievements of a selection of broadband CARS experiments. The number of spectral elements is defined as the spectral span divided by the resolution. SNR: signal-to-noise ratio. When the SNR is preceded by a sign \sim , it has been estimated from a spectrum in a figure of the quoted publication. dc: duty cycle (see Chapter.6.5 in detail)

6.3.4 Time-resolved spectroscopy

Since the consecutive interferograms can be measured in every $1/\delta f$, time-resolved spectroscopy is possible with time resolution of the cycle. In order to demonstrate such capability, a quick test is made with a simple experiment which monitors kinetics of mixing of two chemical liquids. Figure.6.6 shows a spectrogram over 2.3 ms with 3.3 cm^{-1} of spectral resolution. At the beginning of the measurement, only neat toluene is in the cuvette. After starting the measurement, another liquid, neat benzene, is injected into the cuvette and the two liquid start being mixed. The spectrum at the beginning of the measurement shows only the Raman spectrum of toluene which has peaks at 787, 1005, 1031 cm^{-1} , but at around 900 ms, the peak at 995 cm^{-1} , which corresponds to the Raman peak of benzene, suddenly appears and, since then, the intensity of the peaks are varying. Figure.6.6(b) shows the variation of the normalized intensity of the Raman peaks at 1005 cm^{-1} and 995 cm^{-1} , which correspond to toluene and benzene, respectively. The two intensity curves behave in a complementary way, and it indicates that the two chemicals are in a mixing process. The time resolution is 10 ms in this demonstration, which is limited by a long dead time due to the poor duty cycle (see Section 6.5 in detail).

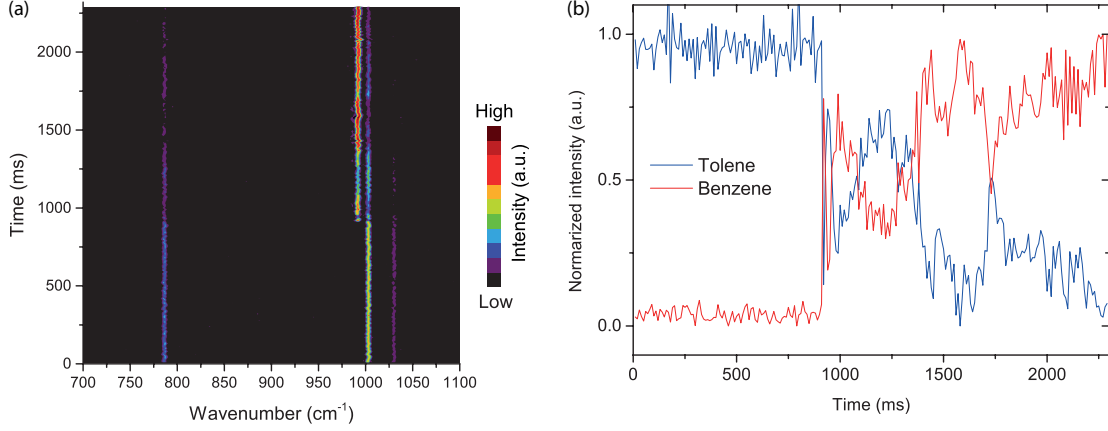


Figure 6.6: (a) Time-resolved spectra of mixing process of toluene and benzene over 2.3 ms with a time resolution of 10 ms. (b) Time-resolved behavior of Raman line intensity of toluene (1005 cm^{-1}) and benzene (995 cm^{-1}).

6.3.5 Heterodyne detection

Heterodyne detection is a useful technique in coherent Raman spectroscopy to enhance the weak signal by a strong local oscillator field [179].

As described in the Subsection.6.2.2, the induced polarizations in the Fourier transform CARS are described (Equation.6.8):

$$P_{FT-CARS}(\tau) \approx P_{R,1,2}^{(3)}(\tau) + P_{NR,1,2}^{(3)}(\tau) + P_{R,2}^{(3)} + P_{NR,2}^{(3)}$$

These polarizations are the origin of generation of the resonant and non-resonant electric fields.

Considering a situation where a local oscillator field (E_{LO}) has the same optical frequency as the anti-Stokes field, the additional FT-CARS signal intensity ($S_{Heterodyne-FT-CARS}(\tau)$) may be written:

$$\begin{aligned} S_{Heterodyne-FT-CARS}(\tau) &\approx \text{Re}[P_{R,1,2}^{(3)*}(\tau)E_{LO}] \\ &\propto \chi_R^{(3)} I_1 \text{Re}[E_2^* E_{LO}] \end{aligned} \quad (6.10)$$

If a small portion of the second pulse is transmitted through the optical filters which, in principle, is supposed to be rejected entirely, the blue part of the second pulse itself can be the local oscillator and in such case it becomes,

$$S_{Heterodyne-FT-CARS}(\tau) \propto \chi_R^{(3)} I_1 I_2 \quad (6.11)$$

Since the $\chi_R^{(3)}$ is proportional to the number of molecules, the heterodyne signal is proportional to the molecular density, while the normal CARS shows quadratic dependence on molecular density. This linear dependence of the concentration simplifies the analysis of quantitative measurement. Another feature of the heterodyne detection is that the intensity of the weak CARS signal is enhanced by a strong local oscillator and it can improve the signal-to-noise ratio. This particular heterodyne method using the second pulse as a local oscillator has an additional benefit that the phase between the two interfering fields is passively stabilized.

One can achieve this condition by tuning the cutoff frequency of the optical filters. Since we use interferometric optical filters, tilting the filters shifts their cutoff frequency. Instead of blocking the fundamental laser beam entirely, a small portion of transmission of the fundamental beam, which contains blue part of the second pulse, enables the heterodyne detection. Figure.6.7(a) shows pulse energy dependence of the Raman signal. The Raman spectrum of neat benzene was measured with several pulse energy where the energies of the first and second pulses are set to the same. The data shows square dependence on the pulse energy instead of cubic, which confirms the situation described by the Equation.6.11. Figure.6.7(b) shows molecular concentration dependence of the Raman signal intensity. Toluene diluted with ethylacetate is measured with several concentration ratio and it shows linear dependence. This also follows the Equation.6.11.

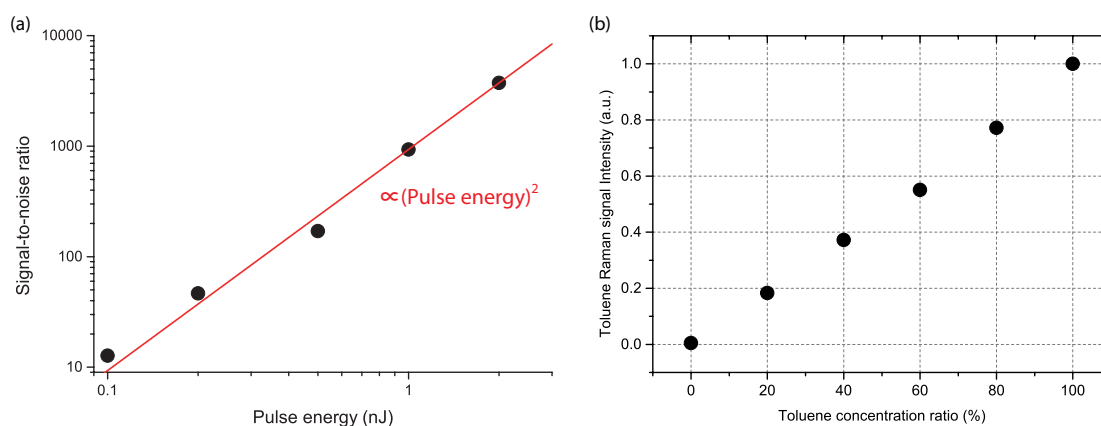


Figure 6.7: Heterodyne CARS signal intensity dependence on (a)pulse energy, and (b)concentration. Both data (a)square dependence on the pulse energy, and (b)linear dependence on the concentration support the Equation6.11.

6.4 Hyperspectral imaging

One of the applications of label-free vibrational spectroscopy is imaging. Broadband spectrum on each image pixel adds a strong feature of chemical specificity, and this capability enriches the imaging. This 2-D spatial image with spectral information is called “Hyperspectral image”. Here, fast and broadband dual-comb CARS hyperspectral imaging is demonstrated.

6.4.1 Experimental setup

Figure.6.8 describes the experimental setup. To record the hyperspectral images (Figure.6.9), the difference in repetition frequencies of the two combs is set to 50 Hz and a microscope objective (LCPLN20XIR; Olympus) focuses the beams on the sample, with a beam diameter of $1.9 \mu\text{m}$ and a Rayleigh length of $3.4 \mu\text{m}$. The pulse energy at the sample is 3.8 nJ and a second-order dispersion of -3000 fs^2 is compensated for. The sample is mounted on a motorized x-y platform (MLS203, Thorlabs) to raster scans across the sample in $1 \mu\text{m}$ steps.

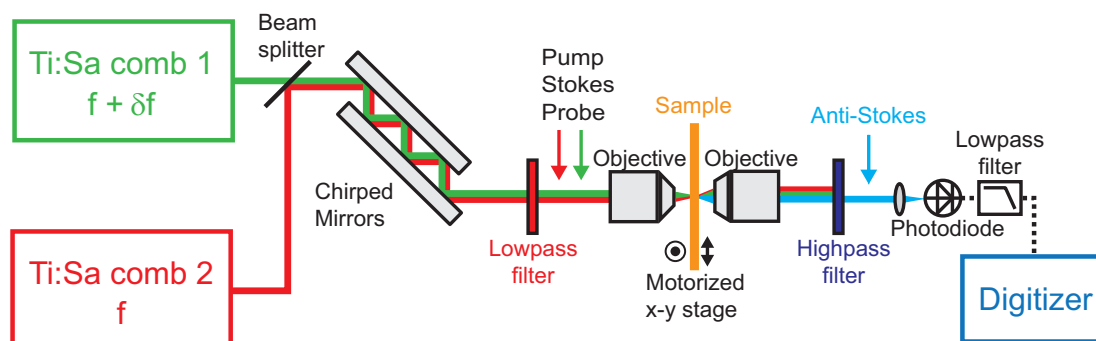


Figure 6.8: Experimental setup of CARS imaging.

6.4.2 Results and discussion

Imaging capabilities are illustrated with a capillary plate ($25 \mu\text{m}$ diameter holes, thickness $500 \mu\text{m}$) filled with a mixture of hexafluorobenzene, nitromethane and toluene. For each pixel, we measure an interferogram within $12 \mu\text{s}$ to obtain a spectrum at an apodized resolution of 10 cm^{-1} . The total measurement time of 40.5 s for the $45 \times 45 \mu\text{m}^2$ hyperspectral image corresponds to an acquisition rate of 50 pixels s^{-1} ; it is limited by the refresh rate

of the interferograms, although the entire sampling time of the interferograms -which are Fourier transformed to give the spectral hypercube in Figure.6.9 -lasts only 24.3 ms.

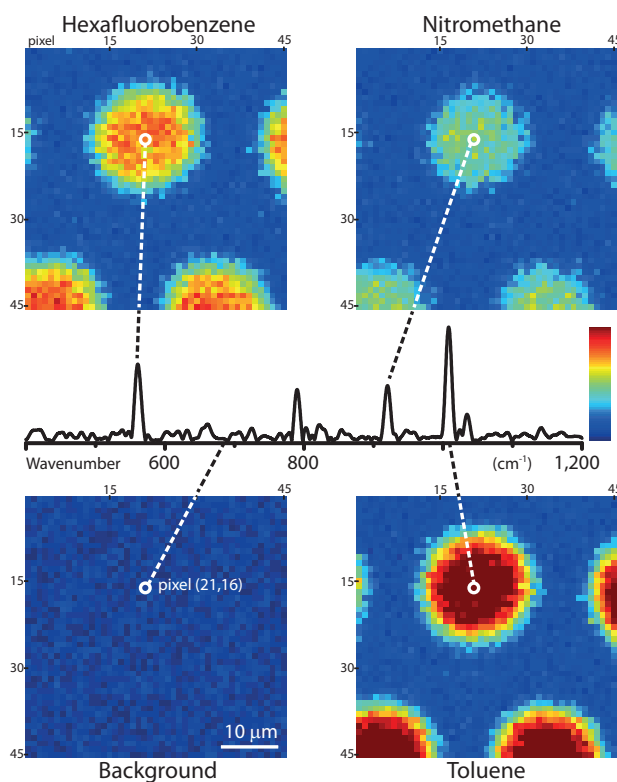


Figure 6.9: Hyperspectral image of a capillary plate with holes filled with a chemical mixture. Each of the 2025 pixels of the hyperspectral cube corresponds to a spectrum at 10 cm^{-1} apodized resolution measured within $12\ \mu\text{s}$ at a fixed spatial location and provides the spectral signature of compounds present in this part of the sample. Scale numbers on the images indicate pixels; the spectrum shown in the centre corresponds to pixel (21,16). Each spectral element of the cube may be plotted as an image (that is, intensity for all pixels at a fixed wavenumber) similar to the four that are shown and provides the spatial quantitative distribution of a given compound with a distinguishable spectral signature at that wavenumber.

Comparison with other techniques

The achievements of the several relevant imaging techniques are shown in the Table.6.2. As described in the spectroscopy part, dual-comb CARS achieves good figures for all the measurement parameters including spectral span, spectral resolution, number of spectral elements, measurement time and signal-to-noise ratio. Compared to the best report concerning the measurement speed of an image, a single color CARS [203], the measurement

time per pixel of the dual-comb CARS is comparable but the number of spectral elements is over 100 times larger. In order to get a spatial image, one needs to scan the measurement point in space, and the dead time due to the low duty cycle limits the total measurement time at the moment. Improvement of the duty cycle, however, is easily implementable and a reasonable strategy for achieving no dead time is proposed in the Section.6.5. The single color CARS [203] could make a hyper-spectral image by tuning the frequency of the laser frame by frame as demonstrated with SRS [151], but the tuning the frequency of the laser over the broad spectral span is not technically trivial. Dual-comb CARS does not require demanding technique to acquire broadband spectra. The multiplex character is another particular feature of dual-comb CARS: all spectral elements are simultaneously measured by a single photodetector within a short time. The technique is thus free of artifacts that would involve temporal change of the chemical nature of the sample at one pixel position, sample motion, irreproducibility of the sample or laser beams positioning. Replacing the single photodetector by a camera would allow multi-channel spectro-imaging.

Reference	Spectral span (cm^{-1})	Resolution (or bandwidth of the single color) (cm^{-1})	Number of spectral elements	Measurement time per pixel (for the entire spectrum)	SNR
This work, Fig.4	1200	10	120	$12 \mu\text{s}$ (dc: 6×10^{-4})	42
[196]	600	13	46	10 min for 1 line (estimated around 20 pixels)	~ 30
[182]	Single color	30	1	30 ms	-
[203]	Single color	3.5	1	$6.4 \mu\text{s}$	-
[204]	180	5	36	50 ms	~ 25

Table 6.2: Comparison of the achievements of a selection of broadband CARS experiments. The number of spectral elements is defined as the spectral span divided by the resolution. SNR: signal-to-noise ratio. When the SNR is preceded by a sign \sim , it has been estimated from a spectrum in a figure of the quoted publication. dc: duty cycle (see Chapter.6.5 in detail)

6.5 Duty cycle

The interferogram reproduces with a time period of $1/\delta f$. This repetition period determines the effective acquisition time of a set of interferograms, as required in time-resolved spectroscopy or hyperspectral imaging experiments. To express the issue in a clear manner, one can introduce the duty cycle of the acquisition, defined as the ratio of the time spent for an interferogram measurement and the time between two interferograms. Following the derivation of the experimental parameters presented in the Section.6.3.2, the measurement time $T(\delta\nu)$ of an interferogram for a chosen optical resolution $\delta\nu$ is given by:

$$T(\delta\nu) = 1.8f/(\delta f\delta\nu)$$

As our interferograms are double-sided (the signal shown in Figure.6.5(a) is symmetric across the burst at zero optical delay), the measurement time of an interferogram should ideally be $1/(2\delta f)$ for the duty cycle to be equal to 1. The optical resolution is then equal to $\delta\nu = 3.6f$. One can thus express the duty cycle dc as:

$$dc = T_{\delta\nu}/T_{3.6f} \quad (6.12)$$

$$dc = 3.6f/\delta\nu \quad (6.13)$$

For this first proof-of-principle experiment, we employed Ti:sapphire femtosecond lasers of a relatively low repetition frequency of 100 MHz, as available in our laboratory. Useful spectral information is only gathered while the pulse separation is shorter than the coherent molecular ringing time. In our spectra (Figure.6.5), this time is 15 ps, corresponding to a resolution of about 120 GHz - 4 cm^{-1} . The duty cycle is thus about 3×10^{-3} . As can be seen from Equation.6.13, the duty cycle is optimal -equal to 1- when the comb line spacing is equal to the desired resolution divided by 3.6. Thus the duty factor can be improved by using frequency combs of higher repetition frequency. However, the scaling of the interferometric signal to noise ratio with the pulse energy and the repetition frequency needs to be considered. Table.6.3 summarizes the experimental conditions of the spectra displayed in Figure.6.5. To explore how these experimental data might be scaled, we consider practical laser systems, commercially available or described in the literature. Titanium-sapphire laser oscillators with a 1 GHz repetition frequency, a pulse duration shorter than 15 fs and an energy per pulse of 2 nJ are commercially available. They would allow, for instance, for dual-comb CARS measurements in similar conditions (pulse energy, down-conversion factor, measurement time, resolution) as in Figure.6.5(d). The difference in repetition frequency for 1 GHz systems would be set to 50 Hz (refreshing time: 20 ms). A spectrum

would have a ten-fold improved signal due to the ten-fold increase in number of events. The duty cycle would be improved ten-fold to reach 3×10^{-2} . We observe that the signal to noise ratio under our experimental conditions decreases ten-fold when the pulse energy is decreased six-fold (Figure. 6.5(c) and 6.5(d)). Thus, under the conditions of Figure. 6.5(b) (down-conversion factor $\delta f/f = 10^{-6}$, measurement time: $14.8 \mu\text{s}$, resolution: 4 cm^{-1}), the use of 1 GHz systems with a pulse energy of 0.5 nJ at the sample should lead to a signal to noise ratio higher than 20. The refreshing time of the interferograms would be 1 ms. Another technique to improve the duty cycle of the interferograms consists in rapidly changing the difference of the repetition frequencies between the two lasers immediately after one interferogram is recorded. Such approach offers the possibility to maintain a high energy per pulse while increasing the duty cycle. This technique has been implemented in [38] for linear absorption dual-comb spectroscopy. In [38], the cavity length of one of the lasers is changed by a piezo-electric transducer. The authors achieve an improvement of about 34 fold in their duty cycle, while maintaining in each spectrum a down-conversion factor $\delta f/f = 10^{-7}$. Preliminary tests in our laboratory with our 100 MHz laser systems equipped with slow piezo-electric transducers that have not been designed for this purpose, indicate that we can reproduce such improvement in the duty cycle. With a down-conversion factor $\delta f/f = 1.5 \times 10^{-7}$, we increase the duty cycle (and shorten the refreshing time) by about 50 when switching the difference in repetition frequencies δf between $\pm 15 \text{ Hz}$. Further progress is feasible with optimized piezo-electric transducers [205] or with exploring other techniques (e.g. using intra-cavity electro-optic modulators [206]) to achieve fast switching of the repetition frequency of one of the lasers. The needed mechanical motion becomes smaller for oscillators with higher repetition frequencies. We note that a realistic approach to reach a duty cycle near one could combine oscillators of 1 GHz repetition frequency and down-conversion factors ranging between 10^{-6} and 10^{-8} (leading to a duty cycle of 3×10^{-2}) with rapid change of the repetition frequency of one of the lasers, leading to an additional improvement of a factor 50 in the duty cycle. Further investigations will be undertaken in the future to characterize the signal-to-noise ratio scaling under various experimental conditions. Other alternatives for increasing the acquisition duty cycle by using frequency comb generators with a high repetition frequency and a low energy per pulse will also be considered. Such alternatives include heterodyning the coherent anti-Stokes interferometric signal with a local oscillator. Heterodyne coherent anti-Stokes Raman spectroscopy has been reported in a variety of implementations (see e.g. [179, 207, 208]) and is expected to render possible the use of oscillators [209] with 10 GHz repetition. This would represent

another way to achieve duty cycles close to unity. Another possibility for improving the data acquisition rate does not involve improving the duty cycle of the acquisition but replacing the single photodetector by a camera or a detector array. In such case, multiple spectra corresponding to different spatial locations in the sample would be simultaneously measured within a single acquisition sequence. Currently the fastest cameras provide a rate higher than one megafame per second. Such solution would benefit from laser systems with a reduced repetition frequency (e.g. 1 MHz) and higher energy per pulse.

Figure	Difference in repetition frequency δf (Hz)	Down-conversion factor $\delta f/f$	Pulse energy (nJ)	Recording time T (μ s)	S/N
3(b)	100	10^{-6}	3	14.8	210
3(c)	5	5×10^{-8}	3	295.5	1000
3(d)	5	5×10^{-8}	0.5	295.5	100

Table 6.3: Summary of the experimental parameters of the spectra shown in Figure.6.5. In all spectra, the oscillators have 100 MHz repetition frequency, the apodized resolution is 4 cm^{-1} and the spectral span of Raman-shifts is 1200 cm^{-1}

6.5.1 Demonstration of duty cycle improvement

Rapid repetition rate switching is a technique to improve the duty cycle, which was demonstrated in the linear dual-comb spectroscopy [38]. Here, we follow this scheme and explore the duty cycle improvement for the dual-comb CARS. The figure.6.10(a) describes concept of the repetition frequency switching technique. When the difference in repetition frequency between two combs (δf) is constant (in the case of left-hand side of the figure), delay between pulses linearly increases and the cycle of the interferograms is $(1/\delta f)$. When the (δf) is modulated with rectangular function (the right-hand side of the figure) at the frequency of (f_{mod}), delay between pulses goes linearly back and forth and the cycle of the interferogram becomes $(1/f_{mod})$.

The experimental setup of the repetition rate modulation is shown in the Figure.6.10(b). A dual-comb interferogram is monitored at the other port of the beam splitter in the setup, which is usually damped by an optical block, and used as an trigger source of the digital delay pulse generator (DG535; Stanford Research Systems). The pulse generator send

modulated voltage with rectangular function to the piezo-electric transducer of one of the laser cavity and modify the repetition frequency. Figure.6.11 shows the interferograms and the corresponding spectra of neat toluene measured by the technique. In this demonstration, the difference in repetition frequency (δf) is switched forth and back between 12.8 Hz and -15.4 Hz with 1.15 ms interval. The spectra show similar spectral shapes. This proof of principle demonstration already shows improvement of the duty cycle about 50. Even faster modulation is feasible with a small and light cavity mirror on a high bandwidth piezo-electric transducer. A feasible plan for the unity of duty cycle is proposed in the previous section.

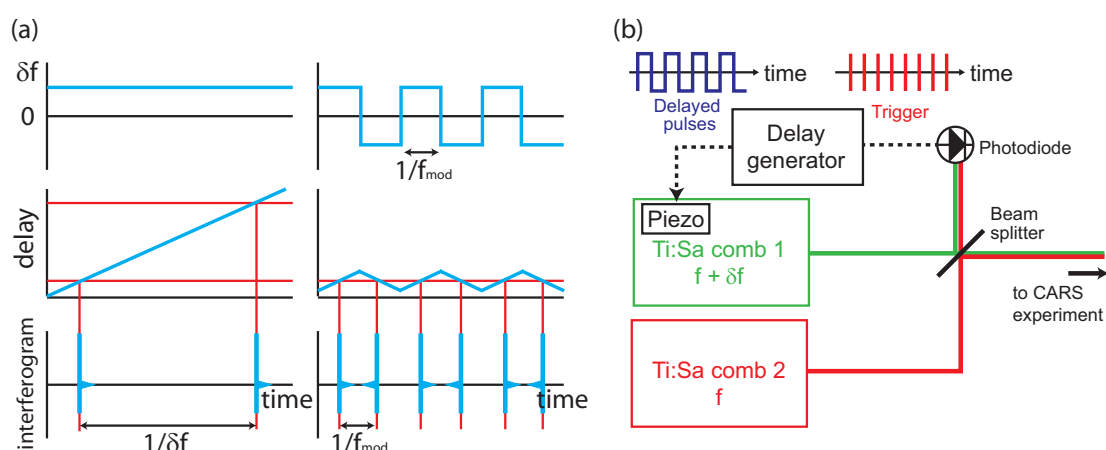


Figure 6.10: (a) Schematics of repetition rate modulation. Left-hand side: the case of constant difference in repetition frequency, Right-hand side: the case of repetition frequency modulation. (b) Experimental setup of repetition rate modulation.

6.6 Differential detection of CARS and CSRS

Fourier transform coherent Raman scattering spectroscopy with differential detection of coherent Stokes and anti-Stokes Raman scattering is demonstrated. The balanced differential detection improves signal-to-noise ratio of the coherent Raman spectrum with enhancement of the signal intensity by a factor of two and with reduction of the noise by canceling out the common-mode noise. The signal-to-noise ratio improvement would play an important role for rapid and sensitive spectroscopy and microscopy.

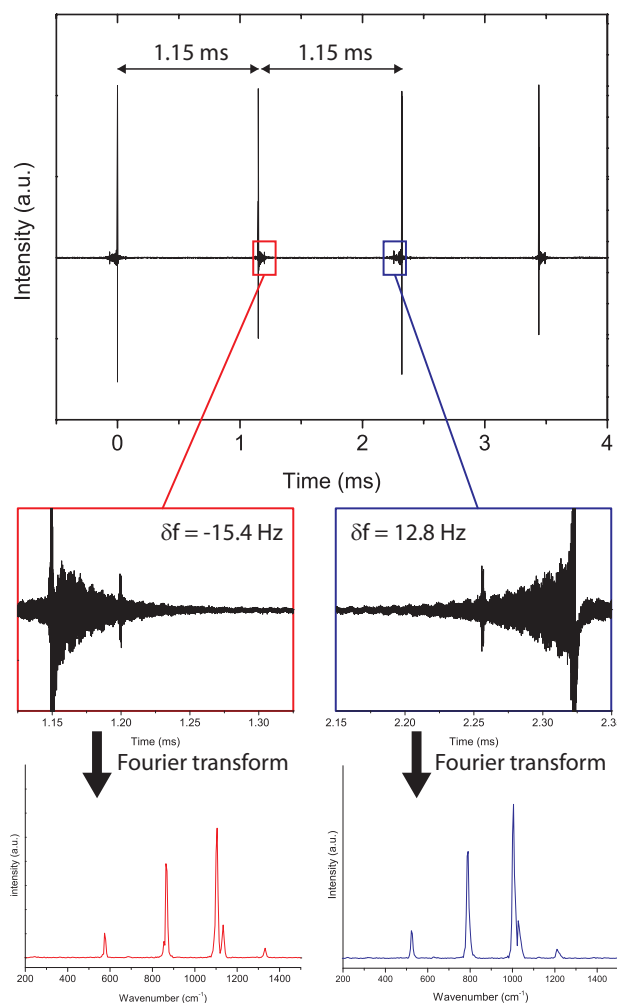


Figure 6.11: Experimental data of interferogram and spectra measured with the repetition rate switching method.

6.6.1 Principle

As explained in the Subsection.6.2.3, the coherent anti-Stokes Raman scattering (CARS) and coherent Stokes Raman scattering (CSRS) are alternately generated in time, and the amount of delay between the first (pump) and the second (probe) pulses determines which radiation generates (Figure.6.3(b)). Since the two radiations have different colors, one can simultaneously detect them with two independent detectors. Due to the alternate radiation, the interference patterns of CARS and CSRS have π phase shift. Thanks to the π phase shift, differential detection of the Stokes and the anti-Stokes signals enhance the signal intensity and cancel out the common-mode noise.

6.6.2 Experimental setup

Figure.6.12 shows the experimental setup. A Ti:Sa mode-locked laser emits 20 fs pulse train with a repetition frequency of 100 MHz. The pulses go through a Michelson interferometer which creates time delayed pulse pairs. The delay between the pulses of the pulse pair is scanned by the moving arm of the interferometer. A pair of chirped mirrors and glass wedges pre-compensate the second-order dispersion of the optics coarsely and finely respectively. The pulses are focused on the liquid sample, neat hexafluorobenzene, in a 1-mm long cuvette by a lens with 8 mm focal length and are collimated by another lens. The total incident average power at the sample is 260 mW. In order to collect the blue-shifted anti-Stokes radiation, the combination of a low-frequency-pass filter and a high-frequency-pass filter, which cutoff wavelengths are 750 nm, are placed before and after the sample respectively. The transmitted anti-Stokes light beam is focused onto one of the Si photodiodes of a 125 kHz bandwidth auto-balanced photodetector (Nirvana, Newport). The beam reflected by the highpass filter after the sample contains red-shifted Stokes component and it is filtered out by a lowpass filter at 835 nm. In order to collect the Stokes signal efficiently by rejecting the fundamental beam, a highpass filter at the same cutoff frequency is placed before the sample. The collected Stokes light is focused onto the second diode of the balanced photodetector. By changing the angle of the filters to the beams, the cutoff wavelengths of the filters are optimized to balance the Stokes and the anti-Stokes signals. The photodetector signal is lowpass filtered and sampled by a data acquisition board. To sample the interferometric signal at evenly-spaced optical retardation, a continuous-wave Yb fiber laser at 1040 nm goes into the interferometer collinearly with the TiSa pulses and the zero crossing of its interference signal is used as a sampling clock. The clock frequency is about 100 kHz. Although this proof-of-principle demonstration uses a Michelson interferometer because only one laser was available when this experiment was made, the same principle works with the dual-comb scheme as well.

6.6.3 Results and discussion

The measured interferograms are shown in Figure.6.13. Similar vibrational interference waveforms are observed in both (a) Stokes and (b) anti-Stokes parts. Since the two signals are generated alternately in time, the waveforms of the interferogram are out of phase ((d) and (e)). Therefore the differential signal shows enhanced signal intensity but low noise because of suppression of the common-mode noise. A single interferogram is measured

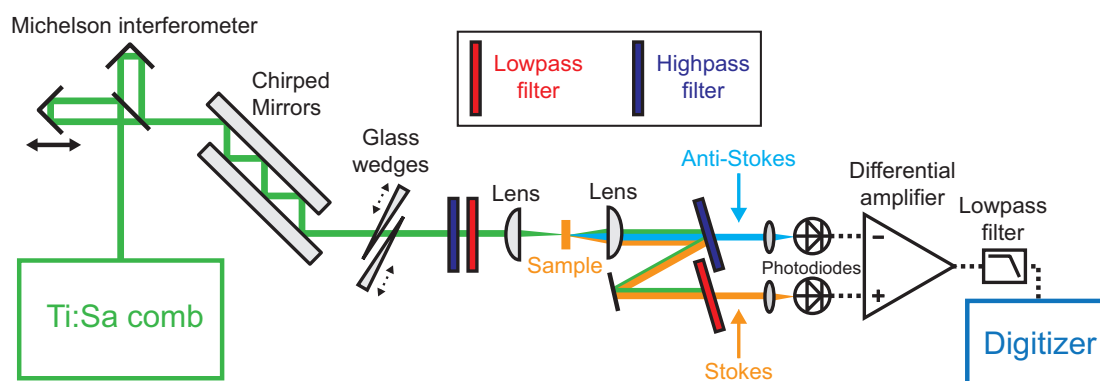


Figure 6.12: Experimental setup of the differential coherent Raman Stokes and anti-Stokes spectroscopy with a Michelson interferometer

in 40 ms and the interferograms are averaged one-hundred-fold to show the clear waveforms. We observed phase shift mismatch from π between the Stokes and the anti-Stokes interferograms by changing the dispersion of the pulses with a pair of glass wedges. This phenomenon can be explained by the optical chirp (second-order dispersion) of the probe pulses. In the frequency domain, the entire probe spectrum experiences equal blue-shift or red-shift, but only part of them are detected by the photodiodes because of the optical filtering, i.e. only the blue-part of the blue-shifted spectrum is detected for the CARS. In this experiment, a portion of the spectrum which wavelength is shorter than cutoff wavelength of the high-frequency-pass optical filter at 750 nm is detected. For the CSRS, only the red part of the spectrum is detected. If the probe pulse is chirped, the high-frequency components (blue part) is either forward or backward to the lower frequency components (red part) within a pulse in the time domain. Therefore the highpass or lowpass optical filtering makes timing difference between CARS and CSRS signals which come to the detectors. Since the pulse duration 20 fs under the condition of transform limit corresponds to $2\pi/3$ of the molecular vibration cycle of 60 fs (assuming Raman frequency at 559 cm^{-1} of hexafluorobenzene), slight optical chirp makes a non-negligible effect for the phase shift. In the experiment, fine tuning of the phase difference is done by dispersion management with a pair of glass wedges. Figure.6.14 shows spectra which correspond to Fourier transform of the interferograms in the Figure.6.13. The broadband spectrum spans over 1300 cm^{-1} with a resolution of 4 cm^{-1} with triangular apodization. The spectral coverage is limited by the spectral bandwidth and the resolution is set to about the intrinsic width of the lines of the liquid sample. In each spectrum three Raman lines of hexafluorobenzene are observed at $369, 442, 559\text{ cm}^{-1}$. The signal-to-noise ratios, which determined by (the

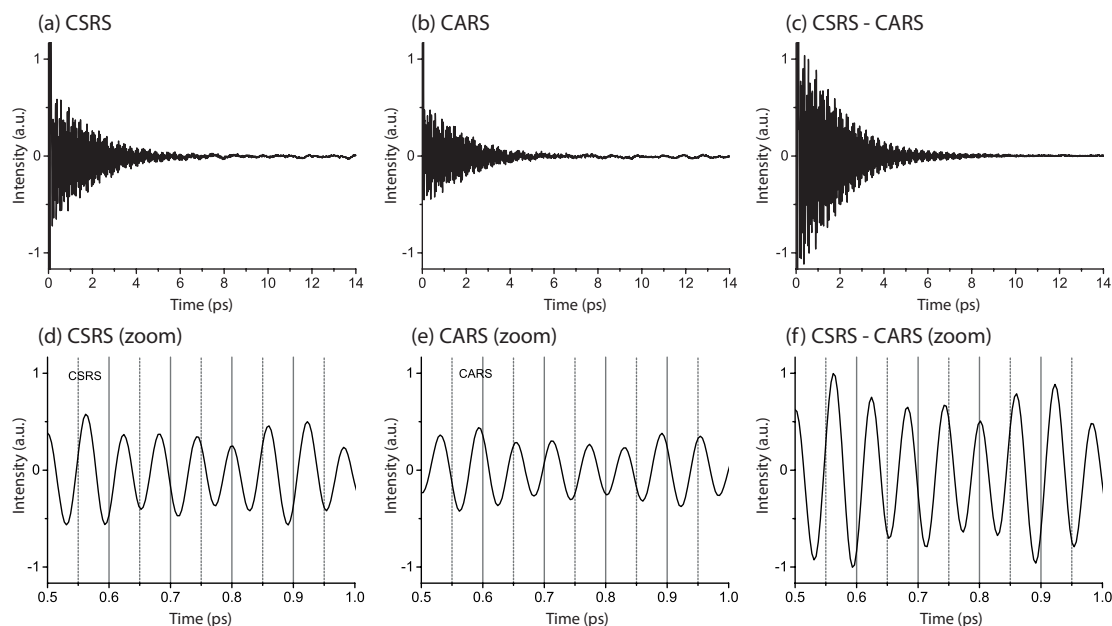


Figure 6.13: Interferograms of (a) Stokes signal (CSRS), (b) anti-Stokes signal (CARS), (c) differential signal of CSRS and CARS signals. (d)-(f) are zoom of a part of the interferograms (a)-(c).

peak intensity at the 559 cm^{-1} Raman line)/(standard deviation of the noise floor from $200\text{-}350\text{ cm}^{-1}$ for low frequency region, and $800\text{-}1000\text{ cm}^{-1}$ for high frequency region), of them are 150 (770) for CSRS, 70 (470) for CARS, 530 (1520) for differential detection in the low frequency region (in the high frequency region). The signal-to-noise ratio is improved both with signal enhancement and noise reduction. Especially in the low Raman frequency region, CARS and CSRS spectra have spiky noises but the differential spectrum does not. This indicates that the noise is common-mode for two signals, which, in this case, is coming from the laser intensity noise and phase or amplitude noise of motion from the moving stage. These spiky noises are undesirable for the fingerprint spectroscopy because they could be assigned as Raman transitions by mistake. Due to the balanced detection, common-mode noise is effectively canceled out.

6.7 Conclusion

This chapter explored coherent anti-Stokes Raman dual-comb spectroscopy and microscopy. In the proof-of-principle experiment, the simple experimental setup based on two frequency combs revealed a broadband nonlinear Raman spectrum over 1200 cm^{-1} with resolution of 4

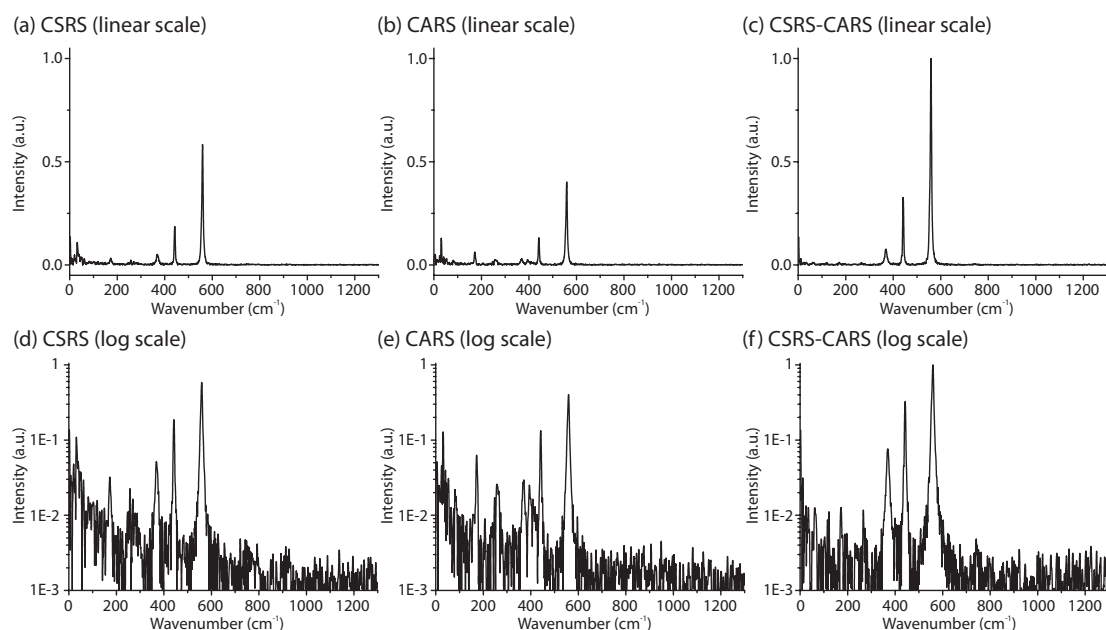


Figure 6.14: Raman spectra of (a) Stokes signal (CSRS), (b) anti-Stokes signal (CARS), (c) differential signal of CSRS and CARS signals. (d)-(f) are displayed with logarithmic intensity scale of (a)-(c).

cm^{-1} within $15 \mu\text{s}$. A liquid sample of 4 different chemical species was measured and showed a non-resonant background-free complex Raman spectrum with good signal-to-noise-ratio within short measurement time (1000 with $300 \mu\text{s}$, 210 with $15 \mu\text{s}$). Time-resolved spectroscopy was demonstrated by measuring consecutive spectra with time resolution of 10 ms. Heterodyne detection with a local oscillator was also demonstrated and the linear dependence on the sample concentration was observed. Hyper-spectral microscopy imaging was demonstrated with spatial scanning of the sample. Each pixel was measured within $12 \mu\text{s}$ and the sampling measurement time of a $45 \mu\text{m} \times 45 \mu\text{m}$ 2D image was 24.3 ms which was about video rate. Each pixel has broadband spectrum over 1400 cm^{-1} with resolution of 10 cm^{-1} . The low duty cycle, however, limited the real measurement time to 40.5 s. The proof-of-principle duty cycle improvement was demonstrated and factor of 50 improvement was achieved without effort. Proof-of-principle differential detection of CARS and CSRS was demonstrated with Michelson Fourier transform spectroscopy. The demonstration showed the signal-to-noise ratio improvement by more than factor of 2.

This work dealt with simple chemical samples to show the potential of dual-comb CARS, but this method could flourish in fields of chemical, biological, medical, or material sciences, e.g. high-speed label-free in vivo biomedical imaging, by its high-speed spectroscopic

capability.

Several schemes exploiting coherent Raman scattering for novel spectroscopy and microscopy applications have recently emerged, and we expect that their combination with our method will deliver techniques with improved performance and utility. For example, our dual-comb approach could benefit surface-enhanced [156, 210] CARS measurements or studies of Raman optical activity [211]. Moreover, exciting imaging capabilities might arise when extending our method to exploit either near-field effects (for example at a metal tip [212]) or far-field effects (for example state depletion [213]) to achieve sub-wavelength spatial resolution.

6.8 Comparison between DC-RIKES and DC-CARS

In this thesis, dual-comb spectroscopy was combined with two types of nonlinear Raman scattering processes, Raman-induced Kerr-effect spectroscopy (Chapter.5) and Coherent anti-Stokes Raman spectroscopy (Chapter.6). Here, we have a look at pros and cons and compare them.

Bandwidth of the Raman spectrum

The bandwidth of the Raman spectrum of DC-RIKES is limited by spectral span of Stokes and local oscillator lasers. In this thesis, we use two erbium-fiber combs with spectral span (spectrum from edge to edge) of 420 cm^{-1} ($6250\text{-}6670 \text{ cm}^{-1}$, $1500\text{-}1600 \text{ nm}$). In the experiment, optical filtering cut out the spectrum down to 150 cm^{-1} for signal-to-noise ratio improvement.

On the other hand, DC-CARS uses two TiSa lasers with spectral span of 1750 cm^{-1} ($11765\text{-}13515 \text{ cm}^{-1}$, $740\text{-}850 \text{ nm}$), therefore the potential bandwidth of the system is 1750 cm^{-1} , but it is practically limited by the optical filtering¹ for signal-to-background ratio improvement. The low frequency side of the Raman spectrum is limited by the difference of these cutoff 180 cm^{-1} , and the high frequency side is limited by filtered spectral span of the laser at 1565 cm^{-1} .

¹In the experiment in this thesis, cutoffs of the filters are at 13330 cm^{-1} for low-frequency-pass, and at 13510 cm^{-1} for high-frequency-pass filter.

Spectral region of the Raman spectrum

The Raman transition frequencies that DC-RIKES can investigate is determined by difference frequency between pump and Stokes lasers. In the experiment in this thesis, the difference is around 3100 cm^{-1} region.²

The spectral region of the DC-CARS, on the other hand, is from low frequency side (ideally zero, but practically limited by optical filtering) up to the frequency limited by the laser bandwidth. This is suitable for investigating molecular fingerprints lying around $500\text{-}1500\text{ cm}^{-1}$. Only by replacing lasers the ones with larger bandwidth, one could reach almost full Raman spectral region up to 4000 cm^{-1} easily. Optimization of the optical filtering could expand the low frequency limit, and for example, pure rotational Raman spectra, which lies around $1\text{-}200\text{ cm}^{-1}$, could be investigated.

Spectral resolution

The instrumental spectral resolution of DC-RIKES is limited by the bandwidth of the pump laser. In the experiment, the pump laser has bandwidth of 37 cm^{-1} (the observed linewidth of the Raman signal is narrower, 27.5 cm^{-1} , due to the optical chirp). The resolution of dual-comb spectroscopy of Stokes comb and local oscillator comb is determined by measurement time of the interferogram, which can be down to repetition frequency, in this case 0.003 cm^{-1} (100 MHz), with Fourier transform of an interferogram. In the experiment, this was set to 6.7 cm^{-1} , so that the instrumental resolution is limited by the pump laser linewidth.

The spectral resolution of DC-CARS is set by measurement time of the interferogram, which can be up to the pulse repetition frequency (0.003 cm^{-1} by the laser with 100 MHz repetition frequency) in the case of Fourier transform of an interferogram. In the experiment, however, the resolution is set to 4 cm^{-1} which is about the intrinsic width of the lines of the liquid sample.

Measurement time

The measurement time of an interferogram for the same spectral span and resolution is in principle identical because the optimum down-conversion factor is chosen by the spectral span to be observed.

²The pump laser emits at 9615 cm^{-1} (1040 nm) and the Stokes laser centered at 6451 cm^{-1} .

Sensitivity

Since the two systems use different types of lasers (ps and fs lasers for DC-RIKES, and fs lasers for DC-CARS), comparing the sensitivity cannot be easily made³.

From dual-comb spectroscopy point of view, dynamic range of the detection and data sampling of the interferogram is often the limiting factor of the signal-to-noise ratio. Since DC-RIKES detects the heterodyne signals between a small amount of emission-like Raman fields and a full pulse train of local field containing the full broadband spectrum, the detector dynamic range has advantage by twice as much as DC-SRS, which detects the heterodyne signals between two full pulse trains containing full spectra. Concerning the data sampling dynamic range, the interferogram (AC part of the signal) does not have strong peak and one can use amplification efficiently and avoid the situation that the dynamic range limits the signal-to-noise ratio. In the experiment, due to the chromatic aberration of the focusing lens, focal points of the pump and Stokes beams are apart from each other and this lost efficiency significantly.

On the other hand, DC-CARS detects only a small amount of emission-like anti-Stokes fields. This overcomes both detection and sampling dynamic range issues (relatively strong non-resonant fields are detected by the detector but these are by far smaller than the excitation pulse fields.).

Implementation

DC-RIKES requires three lasers including a picosecond pump laser and two femtosecond lasers (Stokes and local oscillator), and the pump and Stokes pulse trains have to be synchronized. Dual-comb spectroscopy between Raman emission by the Stokes pulses and pulses from the local oscillator suffers from phase errors of both timing and phase jitters. DC-CARS, on the other hand, requires only two femtosecond lasers. This process is only limited by the timing jitter of the pulses, because it is intrinsically immune to the phase jitters, which makes the experiment much easier regarding the phase error correction.

³For example, depending on the sample, the sample damage threshold can be either pulse peak intensity or average power.

Chapter 7

Summary and outlook

This thesis addressed several challenges of dual-comb spectroscopy and resulted in fruitful achievements. Here we conclude the work in this thesis with future outlook.

Chapter.3 addressed a general issue, so called interferometric phase error, and demonstrated a new technique which successfully solved the issue. The adaptive sampling elegantly compensated for the relative timing and phase jitters due to the instability of the free-running combs. This technique is operated only by analog electronics without any stabilization of the combs nor post computational processing. This technique drastically relaxed constraint of dual-comb spectroscopy concerning the comb's stability. This technique could be a trigger for dual-comb spectroscopy to be spread in a variety of fields where such broadband and fast spectroscopy could open up new investigations. The easy implementation is especially suitable for hands-on researches such as environmental gas analysis. This technique is important not only because of easy implementation but also because it compensates for phase errors over the entire frequency range of the instability including high frequency jitters which cannot be suppressed by any state-of-the-art stabilization technique. In this sense, this technique provides a fundamental solution for distortion-free dual-comb spectroscopy which cannot be achieved with conventional fully stabilized frequency combs. The adaptive sampling was also demonstrated in the frequency converted region with the adaptive signal generated only by the fundamental lasers. This demonstration supports the idea that dual-comb spectroscopy in the extreme frequency, e.g. XUV region, can be done easily without demanding additional experimental efforts in the extreme frequency range.

Chapter.4 dealt with the development of a mid-infrared frequency comb suitable molecular fundamental vibrational spectroscopy. A PPLN based tunable synchronously pumping

optical parametric oscillator pumped by a TiSa oscillator with 20 fs pulse duration was developed. The spectral tuning range was 2400-5500 cm^{-1} with a few to tens of mW average power over the range. The duration of the mid-infrared idler pulse is 33 fs (4.3 cycles) and their spectrum spans over 390 cm^{-1} at 4460 cm^{-1} . The developed system has an intriguing potential for some applications. While it is ready to do broadband linear dual-comb spectroscopy with a second similar system, even nonlinear dual-comb spectroscopy with the ultrashort mid-infrared pulses can be feasible. In order to investigate a new way to expand the spectral bandwidth of mid-infrared frequency combs, supercontinuum generation in a silicon waveguide was demonstrated. The spectrum of the pulses centered at 4360 cm^{-1} from the developed OPO was successfully broadened from 3070 cm^{-1} to 6480 cm^{-1} at -30 dB level which is above an octave span. The coherence of the supercontinuum generation was confirmed by beat note measurements with continuous-wave lasers. This octave spanning mid-infrared broadband pulses could be used for ultra broadband mid-infrared linear dual-comb spectroscopy or for a f-2f interferometer to stabilize the CEO of the comb.

Chapter.5 demonstrated experiment of the first nonlinear dual-comb spectroscopy: Raman-induced Kerr-effect dual-comb spectroscopy. The experiment measured Raman spectra over 150 cm^{-1} spectral span with the spectral resolution of 27.5 cm^{-1} and detected the Raman signal of C-H stretching vibration of benzonitrile around 3100 cm^{-1} . The measurement time of a single spectrum was 2.93 μs and the total measurement time with 100 averaging to achieve reasonable signal-to-noise ratio was 332 ms (the effective measurement time was 293 μs). The estimated Raman gain was 10^{-5} and the relative noise level was 10^{-6} . The weaker fundamental methyl and aromatic C-H stretches of p-Xylene were also measured with averaging of 1062 spectra within total measurement time of 3.5 s (the effective measurement time of 3.2 ms). In this proof-of-principle demonstration, focusing of the pump and Stokes beams were not optimized because of the chromatic aberration of the focusing objective between 1 μm and 1.55 μm . insufficient spatial overlap of the pump and Stokes pulses at the sample limits the efficiency of the nonlinear process. Optimizing the focusing condition could drastically improves the Raman signal intensity. The signal-to-noise ratio could also be improved with careful polarization management, e.g. getting rid of strain-induced depolarization in optics.

Chapter.6 demonstrated experiment of another nonlinear Raman dual-comb spectroscopy: Coherent anti-Stokes Raman dual-comb spectroscopy. In the proof-of-principle experiment, the simple experimental setup based on two frequency combs revealed a broadband nonlinear Raman spectrum over 1200 cm^{-1} with resolution of 4 cm^{-1} within 15 μs . A

liquid sample of 4 different chemical species was measured and showed a non-resonant background-free complex Raman spectrum with good signal-to-noise-ratio within short measurement time (1000 with 300 μs , 210 with 15 μs). Time-resolved spectroscopy was demonstrated by measuring consecutive spectra with time resolution of 10 ms. Heterodyne detection with a local oscillator was also demonstrated and the linear dependence on the sample concentration was observed. Hyper-spectral microscopic imaging was demonstrated with raster scanning of the sample. Each spectrum was measured within 12 μs and the sampling measurement time of a 45 μm x 45 μm 2D image was 24.3 ms which was about video rate. Each pixel has broadband spectrum over 1400 cm^{-1} with resolution of 10 cm^{-1} . The low duty cycle, however, limited the real measurement time to 40.5 s. The proof-of-principle duty cycle improvement was demonstrated and factor of 50 improvement was achieved without effort. Proof-of-principle differential detection of CARS and CSRS was demonstrated with Michelson Fourier transform spectroscopy. The demonstration showed the signal-to-noise ratio improvement by more than factor of 2.

This work dealt with simple chemical samples to show the potential of dual-comb CARS, but this method could flourish in fields of chemical, biological, medical, or material sciences, e.g. high-speed label-free in vivo biomedical imaging, by its high-speed spectroscopic capability.

Bibliography

- [1] K. Goda and B. Jalali, “Dispersive Fourier transformation for fast continuous single-shot measurements,” *Nat. Photon.* **7**, 102–112 (2013).
- [2] T. Udem, R. Holzwarth, and T. W. Hänsch, “Optical frequency metrology,” *Nature* **416**, 233–237 (2002).
- [3] T. W. Hänsch, “Nobel lecture: Passion for precision,” *Rev. Mod. Phys.* **78**, 1297–1309 (2006).
- [4] N. R. Newbury, “Searching for applications with a fine-tooth comb,” *Nat. Photon.* **5**, 186–188 (2011).
- [5] S. A. Diddams, L. Hollberg, and V. Mbele, “Molecular fingerprinting with the resolved modes of a femtosecond laser frequency comb,” *Nature* **445**, 627–630 (2007).
- [6] C. Gohle, B. Stein, A. Schliesser, T. Udem, and T. W. Hänsch, “Frequency comb vernier spectroscopy for broadband, high-resolution, high-sensitivity absorption and dispersion spectra,” *Phys. Rev. Lett.* **99**, 263902 (2007).
- [7] J. Mandon, G. Guelachvili, and N. Picqué, “Fourier transform spectroscopy with a laser frequency comb,” *Nat. Photon.* **3**, 99–102 (2009).
- [8] S. Cundiff, J. Ye, and J. Hall, “Optical frequency synthesis based on mode-locked lasers,” *Review of Scientific Instruments* **72**, 3749–3771 (2001).
- [9] S. T. Cundiff and J. Ye, “*Colloquium* : Femtosecond optical frequency combs,” *Rev. Mod. Phys.* **75**, 325–342 (2003).
- [10] J. L. Hall, “Nobel lecture: Defining and measuring optical frequencies,” *Rev. Mod. Phys.* **78**, 1279–1295 (2006).

- [11] C. G. Parthey, A. Matveev, J. Alnis, B. Bernhardt, A. Beyer, R. Holzwarth, A. Maistrou, R. Pohl, K. Predehl, T. Udem, T. Wilken, N. Kolachevsky, M. Abgrall, D. Rovera, C. Salomon, P. Laurent, and T. W. Hänsch, “Improved measurement of the hydrogen $1S$ - $2S$ transition frequency,” *Phys. Rev. Lett.* **107**, 203001 (2011).
- [12] A. Matveev, C. G. Parthey, K. Predehl, J. Alnis, A. Beyer, R. Holzwarth, T. Udem, T. Wilken, N. Kolachevsky, M. Abgrall, D. Rovera, C. Salomon, P. Laurent, G. Grosche, O. Terra, T. Legero, H. Schnatz, S. Weyers, B. Altschul, and T. W. Hänsch, “Precision measurement of the hydrogen $1S$ - $2S$ frequency via a 920-km fiber link,” *Phys. Rev. Lett.* **110**, 230801 (2013).
- [13] S. A. Diddams, J. C. Bergquist, S. R. Jefferts, and C. W. Oates, “Standards of time and frequency at the outset of the 21st century,” *Science* **306**, 1318–1324 (2004).
- [14] S. A. Diddams, T. Udem, J. C. Bergquist, E. A. Curtis, R. E. Drullinger, L. Hollberg, W. M. Itano, W. D. Lee, C. W. Oates, K. R. Vogel, and D. J. Wineland, “An optical clock based on a single trapped $^{199}\text{Hg}^+$ ion,” *Science* **293**, 825–828 (2001).
- [15] M. Takamoto, F.-L. Hong, R. Higashi, and H. Katori, “An optical lattice clock,” *Nature* **435**, 321–324 (2005).
- [16] H. Katori, “Optical lattice clocks and quantum metrology,” *Nat. Photon.* **5**, 203–210 (2011).
- [17] T. Steinmetz, T. Wilken, C. Araujo-Hauck, R. Holzwarth, T. W. Hänsch, L. Pasquini, A. Manescau, S. D’Odorico, M. T. Murphy, T. Kentischer, W. Schmidt, and T. Udem, “Laser frequency combs for astronomical observations,” *Science* **321**, 1335–1337 (2008).
- [18] T. Wilken, G. L. Curto, R. A. Probst, T. Steinmetz, A. Manescau, L. Pasquini, J. I. G. Hernández, R. Rebolo, T. W. Hänsch, T. Udem *et al.*, “A spectrograph for exoplanet observations calibrated at the centimetre-per-second level,” *Nature* **485**, 611–614 (2012).
- [19] A. Baltuška, T. Fuji, and T. Kobayashi, “Controlling the carrier-envelope phase of ultrashort light pulses with optical parametric amplifiers,” *Phys. Rev. Lett.* **88**, 133901 (2002).
- [20] P. Corkum and F. Krausz, “Attosecond science,” *Nature Phys.* **3**, 381–387 (2007).

- [21] I. Coddington, W. C. Swann, and N. R. Newbury, “Coherent multiheterodyne spectroscopy using stabilized optical frequency combs,” *Phys. Rev. Lett.* **100**, 013902 (2008).
- [22] K. Predehl, G. Grosche, S. M. F. Raupach, S. Droste, O. Terra, J. Alnis, T. Legero, T. W. Hänsch, T. Udem, R. Holzwarth, and H. Schnatz, “A 920-kilometer optical fiber link for frequency metrology at the 19th decimal place,” *Science* **336**, 441–444 (2012).
- [23] F. R. Giorgetta, W. C. Swann, L. C. Sinclair, E. Baumann, I. Coddington, and N. R. Newbury, “Optical two-way time and frequency transfer over free space,” *Nat. Photon.* **7**, 434–438 (2013).
- [24] T. Fortier, M. Kirchner, F. Quinlan, J. Taylor, J. Bergquist, T. Rosenband, N. Lemke, A. Ludlow, Y. Jiang, C. Oates, and S. Diddams, “Generation of ultrastable microwaves via optical frequency division,” *Nat. Photon.* **5**, 425–429 (2011).
- [25] I. Coddington, W. Swann, L. Nenadovic, and N. Newbury, “Rapid and precise absolute distance measurements at long range,” *Nat. Photon.* **3**, 351–356 (2009).
- [26] J. Lee, Y.-J. Kim, K. Lee, S. Lee, and S.-W. Kim, “Time-of-flight measurement with femtosecond light pulses,” *Nat. Photon.* **4**, 716–720 (2010).
- [27] S. T. Cundiff and A. M. Weiner, “Optical arbitrary waveform generation,” *Nat. Photon.* **4**, 760–766 (2010).
- [28] F. Giorgetta, I. Coddington, E. Baumann, W. Swann, and N. Newbury, “Fast high-resolution spectroscopy of dynamic continuous-wave laser sources,” *Nat. Photon.* **4**, 853–857 (2010).
- [29] T.-A. Liu, R.-H. Shu, and J.-L. Peng, “Semi-automatic, octave-spanning optical frequency counter,” *Opt. Express* **16**, 10728–10735 (2008).
- [30] P. Del’Haye, O. Arcizet, M. Gorodetsky, R. Holzwarth, and T. Kippenberg, “Frequency comb assisted diode laser spectroscopy for measurement of microcavity dispersion,” *Nat. Photon.* **3**, 529–533 (2009).
- [31] R. Holzwarth, T. Udem, T. W. Hänsch, J. C. Knight, W. J. Wadsworth, and P. S. J. Russell, “Optical frequency synthesizer for precision spectroscopy,” *Phys. Rev. Lett.* **85**, 2264–2267 (2000).

- [32] D. J. Jones, S. A. Diddams, J. K. Ranka, A. Stentz, R. S. Windeler, J. L. Hall, and S. T. Cundiff, “Carrier-envelope phase control of femtosecond mode-locked lasers and direct optical frequency synthesis,” *Science* **288**, 635–639 (2000).
- [33] F. Adler, P. Masłowski, A. Foltynowicz, K. C. Cossel, T. C. Briles, I. Hartl, and J. Ye, “Mid-infrared fourier transform spectroscopy with a broadband frequency comb,” *Opt. Express* **18**, 21861–21872 (2010).
- [34] C.N.R.S. Colloquium, *J. Phys. Radium*. **19** (1957).
- [35] S.-J. Lee, B. Widiyatmoko, M. Kourogi, and M. Ohtsu, “Ultrahigh scanning speed optical coherence tomography using optical frequency comb generators,” *Japanese Journal of Applied Physics* **40**, L878–L880 (2001).
- [36] S. Schiller, “Spectrometry with frequency combs,” *Opt. Lett.* **27**, 766–768 (2002).
- [37] F. Keilmann, C. Gohle, and R. Holzwarth, “Time-domain mid-infrared frequency-comb spectrometer,” *Opt. Lett.* **29**, 1542–1544 (2004).
- [38] A. Schliesser, M. Brehm, F. Keilmann, and D. van der Weide, “Frequency-comb infrared spectrometer for rapid, remote chemical sensing,” *Opt. Express* **13**, 9029–9038 (2005).
- [39] M. Brehm, A. Schliesser, and F. Keilmann, “Spectroscopic near-field microscopy using frequency combs in the mid-infrared,” *Opt. Express* **14**, 11222–11233 (2006).
- [40] I. Coddington, W. C. Swann, and N. R. Newbury, “Time-domain spectroscopy of molecular free-induction decay in the infrared,” *Opt. Lett.* **35**, 1395–1397 (2010).
- [41] I. Coddington, W. C. Swann, and N. R. Newbury, “Coherent dual-comb spectroscopy at high signal-to-noise ratio,” *Phys. Rev. A* **82**, 043817 (2010).
- [42] N. R. Newbury, I. Coddington, and W. Swann, “Sensitivity of coherent dual-comb spectroscopy,” *Opt. Express* **18**, 7929–7945 (2010).
- [43] A. M. Zolot, F. R. Giorgetta, E. Baumann, J. W. Nicholson, W. C. Swann, I. Coddington, and N. R. Newbury, “Direct-comb molecular spectroscopy with accurate, resolved comb teeth over 43 THz,” *Opt. Lett.* **37**, 638–640 (2012).

- [44] A. Zolot, F. Giorgetta, E. Baumann, W. Swann, I. Coddington, and N. Newbury, “Broad-band frequency references in the near-infrared: Accurate dual comb spectroscopy of methane and acetylene,” *Journal of Quantitative Spectroscopy and Radiative Transfer* **118**, 26 – 39 (2013).
- [45] E. Baumann, F. R. Giorgetta, W. C. Swann, A. M. Zolot, I. Coddington, and N. R. Newbury, “Spectroscopy of the methane ν_3 band with an accurate midinfrared coherent dual-comb spectrometer,” *Phys. Rev. A* **84**, 062513 (2011).
- [46] B. Bernhardt, E. Sorokin, P. Jacquet, R. Thon, T. Becker, I. Sorokina, N. Picqué, and T. Hänsch, “Mid-infrared dual-comb spectroscopy with 2.4 μm $\text{Cr}^{2+}:\text{ZnSe}$ femtosecond lasers,” *Applied Physics B* **100**, 3–8 (2010).
- [47] B. Bernhardt, “Dual comb spectroscopy,” Ph.D. thesis, Ludwig-Maximilians-Universität München (2011). [Http://edoc.ub.uni-muenchen.de/13435/1/Bernhardt_Birgitta.pdf](http://edoc.ub.uni-muenchen.de/13435/1/Bernhardt_Birgitta.pdf).
- [48] S. Boudreau, S. Levasseur, C. Perilla, S. Roy, and J. Genest, “Chemical detection with hyperspectral lidar using dual frequency combs,” *Opt. Express* **21**, 7411–7418 (2013).
- [49] P. Giaccari, J.-D. Deschênes, P. Saucier, J. Genest, and P. Tremblay, “Active fourier-transform spectroscopy combining the direct RF beating of two fiber-based mode-locked lasers with a novel referencing method,” *Opt. Express* **16**, 4347–4365 (2008).
- [50] J.-D. Deschênes, P. Giaccari, and J. Genest, “Optical referencing technique with CW lasers as intermediate oscillators for continuous full delay range frequency comb interferometry,” *Opt. Express* **18**, 23358–23370 (2010).
- [51] J. Roy, J.-D. Deschênes, S. Potvin, and J. Genest, “Continuous real-time correction and averaging for frequency comb interferometry,” *Opt. Express* **20**, 21932–21939 (2012).
- [52] T. Ideguchi, A. Poisson, G. Guelachvili, T. W. Hänsch, and N. Picqué, “Adaptive dual-comb spectroscopy in the green region,” *Opt. Lett.* **37**, 4847–4849 (2012).
- [53] T. Ideguchi, A. Poisson, G. Guelachvili, N. Picqué, and T. W. Hänsch, “Adaptive real-time dual-comb spectroscopy,” *Nat. Commun.* **5**, 3375 (2014).

- [54] Z. Zhang, T. Gardiner, and D. T. Reid, “Mid-infrared dual-comb spectroscopy with an optical parametric oscillator,” *Opt. Lett.* **38**, 3148–3150 (2013).
- [55] T. Yasui, E. Saneyoshi, and T. Araki, “Asynchronous optical sampling terahertz time-domain spectroscopy for ultrahigh spectral resolution and rapid data acquisition,” *Applied Physics Letters* **87**, 061101 (2005).
- [56] T. Yasui, Y. Kabetani, E. Saneyoshi, S. Yokoyama, and T. Araki, “Terahertz frequency comb by multifrequency-heterodyning photoconductive detection for high-accuracy, high-resolution terahertz spectroscopy,” *Applied Physics Letters* **88**, 241104 (2006).
- [57] T. Yasui, M. Nose, A. Ihara, K. Kawamoto, S. Yokoyama, H. Inaba, K. Minoshima, and T. Araki, “Fiber-based, hybrid terahertz spectrometer using dual fiber combs,” *Opt. Lett.* **35**, 1689–1691 (2010).
- [58] T. Yasui, Y.-D. Hsieh, Y. Iyonaga, Y. Sakaguchi, S. Yokoyama, H. Inaba, K. Minoshima, F. Hindle, and T. Araki, “Gapless dual-comb spectroscopy in terahertz region,” arXiv preprint arXiv:1303.5799 (2013).
- [59] T. Ideguchi, B. Bernhardt, G. Guelachvili, T. W. Hänsch, and N. Picqué, “Raman-induced Kerr-effect dual-comb spectroscopy,” *Opt. Lett.* **37**, 4498–4500 (2012).
- [60] T. Ideguchi, S. Holzner, B. Bernhardt, G. Guelachvili, N. Picqué, and T. W. Hänsch, “Coherent Raman spectro-imaging with laser frequency combs,” *Nature* **502**, 355–358 (2013).
- [61] A. Hipke, S. A. Meek, T. Ideguchi, T. W. Hänsch, and N. Picqué, “Broadband high-resolution two-photon spectroscopy with laser frequency combs,” arXiv preprint arXiv:1311.6138 (2013).
- [62] A. Hipke, S. A. Meek, G. Guelachvili, T. W. Hänsch, and N. Picqué, “Doppler-free broad spectral bandwidth two-photon spectroscopy with two laser frequency combs,” in “CLEO: 2013 Postdeadline,” (Optical Society of America, 2013), p. CTh5C.8.
- [63] N. Kuse, A. Ozawa, I. Ito, and Y. Kobayashi, “Dual-comb saturated absorption spectroscopy,” in “CLEO: 2013,” (Optical Society of America, 2013), p. CTu2I.1.

- [64] T.-A. Liu, N. R. Newbury, and I. Coddington, “Sub-micron absolute distance measurements in sub-millisecond times with dual free-running femtosecond Er fiber-lasers,” *Opt. Express* **19**, 18501–18509 (2011).
- [65] V. Michaud-Belleau, J. Roy, S. Potvin, J.-R. Carrier, L.-S. Verret, M. Charlebois, J. Genest, and C. N. Allen, “Whispering gallery mode sensing with a dual frequency comb probe,” *Opt. Express* **20**, 3066–3075 (2012).
- [66] N. Kuse, A. Ozawa, and Y. Kobayashi, “Static FBG strain sensor with high resolution and large dynamic range by dual-comb spectroscopy,” *Opt. Express* **21**, 11141–11149 (2013).
- [67] G. Guelachvili, “Distortions in fourier spectra and diagnosis,” in “Spectrometric Techniques, Volume II,” , G. A. Vanasse, ed. (Academic Press (New York), 1981), pp. 1–62.
- [68] N. R. Newbury and W. C. Swann, “Low-noise fiber-laser frequency combs (invited),” *J. Opt. Soc. Am. B* **24**, 1756–1770 (2007).
- [69] S. Diddams, J. Ye, and L. Hollberg, “Femtosecond lasers for optical clocks and low noise frequency synthesis,” in “Femtosecond Optical Frequency Comb: Principle, Operation, and Applications,” , J. Ye and S. Cundiff, eds. (Springer US, 2005), pp. 225–262.
- [70] B. Bernhardt, A. Ozawa, P. Jacquet, M. Jacquy, Y. Kobayashi, T. Udem, R. Holzwarth, G. Guelachvili, T. W. Hänsch, and N. Picqué, “Cavity-enhanced dual-comb spectroscopy,” *Nat. Photon.* **4**, 55–57 (2010).
- [71] F. Zhu, H. Hundertmark, A. A. Kolomenskii, J. Strohaber, R. Holzwarth, and H. A. Schuessler, “High-power mid-infrared frequency comb source based on a femtosecond Er: fiber oscillator,” *Opt. Lett.* **38**, 2360–2362 (2013).
- [72] L. Rothman, I. Gordon, A. Barbe, D. Benner, P. Bernath, M. Birk, V. Boudon, L. Brown, A. Campargue, J.-P. Champion, K. Chance, L. Coudert, V. Dana, V. Devi, S. Fally, J.-M. Flaud, R. Gamache, A. Goldman, D. Jacquemart, I. Kleiner, N. Lacombe, W. Lafferty, J.-Y. Mandin, S. Massie, S. Mikhailenko, C. Miller, N. Moazzen-Ahmadi, O. Naumenko, A. Nikitin, J. Orphal, V. Perevalov, A. Perrin, A. Predoi-Cross, C. Rinsland, M. Rotger, M. Šimečková, M. Smith, K. Sung, S. Tashkun,

- J. Tennyson, R. Toth, A. Vandaele, and J. V. Auwera, “The {HITRAN} 2008 molecular spectroscopic database,” *Journal of Quantitative Spectroscopy and Radiative Transfer* **110**, 533 – 572 (2009).
- [73] C. Erny, K. Moutzouris, J. Biegert, D. Kühlke, F. Adler, A. Leitenstorfer, and U. Keller, “Mid-infrared difference-frequency generation of ultrashort pulses tunable between 3.2 and 4.8 μm from a compact fiber source,” *Opt. Lett.* **32**, 1138–1140 (2007).
- [74] S. Gerstenkorn and P. Luc, “Atlas du spectre d’Absorption de la Molecule d’Iode entre 14800–20000 cm^{-1} (Centre National de la Recherche Scientifique, Paris, 1978);” Absolute iodine (I_2) standards measured by means of fourier transform spectroscopy,” *Rev. Phys. Appl* **14**, 791–794 (1979).
- [75] H. Salami and A. J. Ross, “A molecular iodine atlas in ascii format,” *J. Mol. Spectrosc.* **233**, 157–159 (2005).
- [76] A. Schliesser, N. Picqué, and T. W. Hänsch, “Mid-infrared frequency combs,” *Nat. Photon.* **6**, 440–449 (2012).
- [77] M. N. Cizmeciyan, H. Cankaya, A. Kurt, and A. Sennaroglu, “Kerr-lens mode-locked femtosecond $\text{Cr}^{2+}:\text{ZnSe}$ laser at 2420 nm,” *Opt. Lett.* **34**, 3056–3058 (2009).
- [78] N. Tolstik, E. Sorokin, and I. T. Sorokina, “Kerr-lens mode-locked $\text{Cr}:\text{ZnS}$ laser,” *Opt. Lett.* **38**, 299–301 (2013).
- [79] E. Sorokin, N. Tolstik, K. I. Schaffers, and I. T. Sorokina, “Femtosecond SESAM-modelocked $\text{Cr}:\text{ZnS}$ laser,” *Opt. Express* **20**, 28947–28952 (2012).
- [80] M. N. Cizmeciyan, J. W. Kim, S. Bae, B. H. Hong, F. Rotermund, and A. Sennaroglu, “Graphene mode-locked femtosecond $\text{Cr}:\text{ZnSe}$ laser at 2500 nm,” *Opt. Lett.* **38**, 341–343 (2013).
- [81] L. Nelson, E. Ippen, and H. Haus, “Broadly tunable sub-500 fs pulses from an additive-pulse mode-locked thulium-doped fiber ring laser,” *Applied Physics Letters* **67**, 19–21 (1995).
- [82] M. A. Solodyankin, E. D. Obraztsova, A. S. Lobach, A. I. Chernov, A. V. Tausenev, V. I. Konov, and E. M. Dianov, “Mode-locked 1.93 μm thulium fiber laser with a carbon nanotube absorber,” *Opt. Lett.* **33**, 1336–1338 (2008).

- [83] K. Kieu and F. Wise, “Soliton thulium-doped fiber laser with carbon nanotube saturable absorber,” *Photonics Technology Letters, IEEE* **21**, 128–130 (2009).
- [84] F. Haxsen, D. Wandt, U. Morgner, J. Neumann, and D. Kracht, “Pulse characteristics of a passively mode-locked thulium fiber laser with positive and negative cavity dispersion,” *Opt. Express* **18**, 18981–18988 (2010).
- [85] Q. Wang, J. Geng, Z. Jiang, T. Luo, and S. Jiang, “Mode-locked Tm-Ho-codoped fiber laser at 2.06 μm ,” *Photonics Technology Letters, IEEE* **23**, 682–684 (2011).
- [86] C. R. Phillips, C. Langrock, J. S. Pelc, M. M. Fejer, J. Jiang, M. E. Fermann, and I. Hartl, “Supercontinuum generation in quasi-phase-matched LiNbO₃ waveguide pumped by a Tm-doped fiber laser system,” *Opt. Lett.* **36**, 3912–3914 (2011).
- [87] F. Adler and S. A. Diddams, “High-power, hybrid Er:fiber/Tm:fiber frequency comb source in the 2 μm wavelength region,” *Opt. Lett.* **37**, 1400–1402 (2012).
- [88] N. Coluccelli, A. Gambetta, D. Gatti, M. Marangoni, A. D. Lieto, M. Tonelli, G. Galzerano, and P. Laporta, “1.6-W self-referenced frequency comb at 2.06 μm using a Ho:YLF multipass amplifier,” *Opt. Lett.* **36**, 2299–2301 (2011).
- [89] P. Del’Haye, A. Schliesser, O. Arcizet, T. Wilken, R. Holzwarth, and T. Kippenberg, “Optical frequency comb generation from a monolithic microresonator,” *Nature* **450**, 1214–1217 (2007).
- [90] T. J. Kippenberg, R. Holzwarth, and S. A. Diddams, “Microresonator-based optical frequency combs,” *Science* **332**, 555–559 (2011).
- [91] K. Saha, Y. Okawachi, B. Shim, J. S. Levy, R. Salem, A. R. Johnson, M. A. Foster, M. R. E. Lamont, M. Lipson, and A. L. Gaeta, “Modelocking and femtosecond pulse generation in chip-based frequency combs,” *Opt. Express* **21**, 1335–1343 (2013).
- [92] T. Herr, V. Brasch, J. Jost, C. Wang, N. Kondratiev, M. Gorodetsky, and T. Kippenberg, “Temporal solitons in optical microresonators,” *Nat. Photon.* (2013).
- [93] C. Wang, T. Herr, P. Del’Haye, A. Schliesser, J. Hofer, R. Holzwarth, T. Hänsch, N. Picqué, and T. Kippenberg, “Mid-infrared optical frequency combs at 2.5 μm based on crystalline microresonators,” *Nat. Commun.* **4**, 1345 (2013).

- [94] R. Paiella, F. Capasso, C. Gmachl, D. L. Sivco, J. N. Baillargeon, A. L. Hutchinson, A. Y. Cho, and H. C. Liu, “Self-mode-locking of quantum cascade lasers with giant ultrafast optical nonlinearities,” *Science* **290**, 1739–1742 (2000).
- [95] C. Y. Wang, L. Kuznetsova, V. M. Gkortsas, L. Diehl, F. X. Kärtner, M. A. Belkin, A. Belyanin, X. Li, D. Ham, H. Schneider, P. Grant, C. Y. Song, S. Haffouz, Z. R. Wasilewski, H. Liu, and F. Capasso, “Mode-locked pulses from mid-infrared quantum cascade lasers,” *Opt. Express* **17**, 12929–12943 (2009).
- [96] A. Hugi, G. Villares, S. Blaser, H. Liu, and J. Faist, “Mid-infrared frequency comb based on a quantum cascade laser,” *Nature* **492**, 229–233 (2012).
- [97] P. Maddaloni, P. Malara, G. Gagliardi, and P. D. Natale, “Mid-infrared fibre-based optical comb,” *New Journal of Physics* **8**, 262 (2006).
- [98] S. M. Foreman, D. J. Jones, and J. Ye, “Flexible and rapidly configurable femtosecond pulse generation in the mid-IR,” *Opt. Lett.* **28**, 370–372 (2003).
- [99] S. M. Foreman, A. Marian, J. Ye, E. A. Petrukhin, M. A. Gubin, O. D. Mücke, F. N. C. Wong, E. P. Ippen, and F. X. Kärtner, “Demonstration of a HeNe/CH₄-based optical molecular clock,” *Opt. Lett.* **30**, 570–572 (2005).
- [100] M. Gubin, A. Kireev, A. Konyashchenko, P. Kryukov, A. Shelkovnikov, A. Tausenev, and D. Tyurikov, “Femtosecond fiber laser based methane optical clock,” *Applied Physics B* **95**, 661–666 (2009).
- [101] A. Sell, R. Scheu, A. Leitenstorfer, and R. Huber, “Field-resolved detection of phase-locked infrared transients from a compact Er: fiber system tunable between 55 and 107 THz,” *Applied Physics Letters* **93**, 251107–251107–3 (2008).
- [102] S. A. Meek, A. Poisson, G. Guelachvili, T. W. Hänsch, and N. Picqué, “Fourier transform spectroscopy around 3 μm with a broad difference frequency comb,” *Applied Physics B* pp. 1–6 (2013). Published online.
- [103] A. Gambetta, R. Ramponi, and M. Marangoni, “Mid-infrared optical combs from a compact amplified Er-doped fiber oscillator,” *Opt. Lett.* **33**, 2671–2673 (2008).
- [104] F. Keilmann and S. Amarie, “Mid-infrared frequency comb spanning an octave based on an Er fiber laser and difference-frequency generation,” *Journal of Infrared, Millimeter, and Terahertz Waves* **33**, 479–484 (2012).

- [105] A. Ruehl, A. Gambetta, I. Hartl, M. E. Fermann, K. S. E. Eikema, and M. Marangoni, “Widely-tunable mid-infrared frequency comb source based on difference frequency generation,” *Opt. Lett.* **37**, 2232–2234 (2012).
- [106] M. H. Dunn and M. Ebrahimzadeh, “Parametric generation of tunable light from continuous-wave to femtosecond pulses,” *Science* **286**, 1513–1517 (1999).
- [107] D. Reid, J. Sun, T. Lamour, and T. Ferreiro, “Advances in ultrafast optical parametric oscillators,” *Laser Physics Letters* **8**, 8–15 (2011).
- [108] P. Loza-Alvarez, C. T. A. Brown, D. T. Reid, W. Sibbett, and M. Missey, “High-repetition-rate ultrashort-pulse optical parametric oscillator continuously tunable from 2.8 to 6.8 μm ,” *Opt. Lett.* **24**, 1523–1525 (1999).
- [109] T. Andres, P. Haag, S. Zelt, J.-P. Meyn, A. Borsutzky, R. Beigang, and R. Wallenstein, “Synchronously pumped femtosecond optical parametric oscillator of congruent and stoichiometric MgO-doped periodically poled lithium niobate,” *Applied Physics B* **76**, 241–244 (2003).
- [110] J. H. Sun, B. J. S. Gale, and D. T. Reid, “Composite frequency comb spanning 0.4–2.4 μm from a phase-controlled femtosecond Ti:sapphire laser and synchronously pumped optical parametric oscillator,” *Opt. Lett.* **32**, 1414–1416 (2007).
- [111] R. Gebs, T. Dekorsy, S. A. Diddams, and A. Bartels, “1-GHz repetition rate femtosecond OPO with stabilized offset between signal and idler frequency combs,” *Opt. Express* **16**, 5397–5405 (2008).
- [112] Z. Zhang, J. Sun, T. Gardiner, and D. T. Reid, “Broadband conversion in an Yb:KYW-pumped ultrafast optical parametric oscillator with a long nonlinear crystal,” *Opt. Express* **19**, 17127–17132 (2011).
- [113] F. Adler, K. C. Cossel, M. J. Thorpe, I. Hartl, M. E. Fermann, and J. Ye, “Phase-stabilized, 1.5 W frequency comb at 2.8–4.8 μm ,” *Opt. Lett.* **34**, 1330–1332 (2009).
- [114] D. Reid, B. Gale, and J. Sun, “Frequency comb generation and carrier-envelope phase control in femtosecond optical parametric oscillators,” *Laser Physics* **18**, 87–103 (2008).

- [115] T. I. Ferreiro, J. Sun, and D. T. Reid, “Locking the carrier-envelope-offset frequency of an optical parametric oscillator without f-2f self-referencing,” *Opt. Lett.* **35**, 1668–1670 (2010).
- [116] T. I. Ferreiro, J. Sun, and D. T. Reid, “Frequency stability of a femtosecond optical parametric oscillator frequency comb,” *Opt. Express* **19**, 24159–24164 (2011).
- [117] R. A. McCracken, J. Sun, C. G. Leburn, and D. T. Reid, “Broadband phase coherence between an ultrafast laser and an OPO using lock-to-zero CEO stabilization,” *Opt. Express* **20**, 16269–16274 (2012).
- [118] N. Leindecker, A. Marandi, R. L. Byer, and K. L. Vodopyanov, “Broadband degenerate OPO for mid-infrared frequency comb generation,” *Opt. Express* **19**, 6296–6302 (2011).
- [119] K. L. Vodopyanov, E. Sorokin, I. T. Sorokina, and P. G. Schunemann, “Mid-IR frequency comb source spanning 4.4–5.4 μm based on subharmonic GaAs optical parametric oscillator,” *Opt. Lett.* **36**, 2275–2277 (2011).
- [120] N. Leindecker, A. Marandi, R. L. Byer, K. L. Vodopyanov, J. Jiang, I. Hartl, M. Fermann, and P. G. Schunemann, “Octave-spanning ultrafast OPO with 2.6–6.1 μm instantaneous bandwidth pumped by femtosecond Tm-fiber laser,” *Opt. Express* **20**, 7046–7053 (2012).
- [121] M. W. Haakestad, A. Marandi, N. Leindecker, and K. L. Vodopyanov, “Five-cycle pulses near $\lambda = 3 \mu\text{m}$ produced in a subharmonic optical parametric oscillator via fine dispersion management,” *Laser Photonics Reviews* **7**, L93–L97 (2013).
- [122] A. Marandi, N. C. Leindecker, V. Pervak, R. L. Byer, and K. L. Vodopyanov, “Coherence properties of a broadband femtosecond mid-IR optical parametric oscillator operating at degeneracy,” *Opt. Express* **20**, 7255–7262 (2012).
- [123] L. Nugent-Glandorf, T. Neely, F. Adler, A. J. Fleisher, K. C. Cossel, B. Bjork, T. Dinneen, J. Ye, and S. A. Diddams, “Mid-infrared virtually imaged phased array spectrometer for rapid and broadband trace gas detection,” *Opt. Lett.* **37**, 3285–3287 (2012).

- [124] T. W. Neely, L. Nugent-Glandorf, F. Adler, and S. A. Diddams, “Broadband mid-infrared frequency upconversion and spectroscopy with an aperiodically poled LiNbO₃ waveguide,” *Opt. Lett.* **37**, 4332–4334 (2012).
- [125] E. Sorokin, I. T. Sorokina, J. Mandon, G. Guelachvili, and N. Picqué, “Sensitive multiplex spectroscopy in the molecular fingerprint 2.4 μm region with a Cr²⁺:ZnSe femtosecond laser,” *Opt. Express* **15**, 16540–16545 (2007).
- [126] A. Foltynowicz, P. Maslowski, A. Fleisher, B. Bjork, and J. Ye, “Cavity-enhanced optical frequency comb spectroscopy in the mid-infrared application to trace detection of hydrogen peroxide,” *Applied Physics B* **110**, 163–175 (2013).
- [127] D. C. Edelstein, E. S. Wachman, and C. L. Tang, “Broadly tunable high repetition rate femtosecond optical parametric oscillator,” *Applied Physics Letters* **54**, 1728–1730 (1989).
- [128] O. Paul, A. Quosig, T. Bauer, M. Nittmann, J. Bartschke, G. Anstett, and J. L’huillier, “Temperature-dependent sellmeier equation in the MIR for the extraordinary refractive index of 5% MgO doped congruent LiNbO₃,” *Applied Physics B* **86**, 111–115 (2007).
- [129] B. J. Eggleton, B. Luther-Davies, and K. Richardson, “Chalcogenide photonics,” *Nat. Photon.* **5**, 141–148 (2011).
- [130] Y. Yu, X. Gai, T. Wang, P. Ma, R. Wang, Z. Yang, D.-Y. Choi, S. Madden, and B. Luther-Davies, “Mid-infrared supercontinuum generation in chalcogenides,” *Opt. Mater. Express* **3**, 1075–1086 (2013).
- [131] B. Jalali and S. Fathpour, “Silicon photonics,” *Lightwave Technology, Journal of* **24**, 4600–4615 (2006).
- [132] B. Kuyken, “Four-wave-mixing in dispersion-engineered silicon nanophotonic circuits for telecommunication and sensing applications,” Ph.D. thesis, Ghent University (2013). [Http://photonics.intec.ugent.be/download/phd195.pdf](http://photonics.intec.ugent.be/download/phd195.pdf).
- [133] B. Kuyken, X. Liu, R. M. O. Jr., R. Baets, G. Roelkens, and W. M. J. Green, “Mid-infrared to telecom-band supercontinuum generation in highly nonlinear silicon-on-insulator wire waveguides,” *Opt. Express* **19**, 20172–20181 (2011).

- [134] J. K. Ranka, R. S. Windeler, and A. J. Stentz, “Visible continuum generation in air-silica microstructure optical fibers with anomalous dispersion at 800 nm,” *Opt. Lett.* **25**, 25–27 (2000).
- [135] M. Bellini and T. W. Hänsch, “Phase-locked white-light continuum pulses: toward a universal optical frequency-comb synthesizer,” *Opt. Lett.* **25**, 1049–1051 (2000).
- [136] J. M. Dudley, G. Genty, and S. Coen, “Supercontinuum generation in photonic crystal fiber,” *Rev. Mod. Phys.* **78**, 1135–1184 (2006).
- [137] J. M. Dudley and S. Coen, “Coherence properties of supercontinuum spectra generated in photonic crystal and tapered optical fibers,” *Opt. Lett.* **27**, 1180–1182 (2002).
- [138] W. Bogaerts, “Nanophotonic waveguides and photonic crystals in silicon-on-insulator,” Ph.D. thesis, Ghent University (2004). [Http://photonics.intec.ugent.be/download/phd135.pdf](http://photonics.intec.ugent.be/download/phd135.pdf).
- [139] H. Tsang, C. S. Wong, T. Liang, I. E. Day, S. Roberts, A. Harpin, J. Drake, and M. Asghari, “Optical dispersion, two-photon absorption and self-phase modulation in silicon waveguides at 1.5 μm wavelength,” *Applied Physics Letters* **80**, 416–418 (2002).
- [140] C. L. Evans and X. S. Xie, “Coherent anti-Stokes Raman scattering microscopy: Chemical imaging for biology and medicine,” *Annual Review of Analytical Chemistry* **1**, 883–909 (2008).
- [141] B. G. Saar, C. W. Freudiger, J. Reichman, C. M. Stanley, G. R. Holtom, and X. S. Xie, “Video-rate molecular imaging in vivo with stimulated Raman scattering,” *Science* **330**, 1368–1370 (2010).
- [142] Y. Ozeki, W. Umemura, K. Sumimura, N. Nishizawa, K. Fukui, and K. Itoh, “Stimulated Raman hyperspectral imaging based on spectral filtering of broadband fiber laser pulses,” *Opt. Lett.* **37**, 431–433 (2012).
- [143] L. Kong, M. Ji, G. R. Holtom, D. Fu, C. W. Freudiger, and X. S. Xie, “Multicolor stimulated Raman scattering microscopy with a rapidly tunable optical parametric oscillator,” *Opt. Lett.* **38**, 145–147 (2013).

- [144] A. F. Pegoraro, A. Ridsdale, D. J. Moffatt, Y. Jia, J. P. Pezacki, and A. Stolow, “Optimally chirped multimodal cars microscopy based on a single ti:sapphireoscillator,” *Opt. Express* **17**, 2984–2996 (2009).
- [145] D. Fu, G. Holtom, C. Freudiger, X. Zhang, and X. S. Xie, “Hyperspectral imaging with stimulated Raman scattering by chirped femtosecond lasers,” *The Journal of Physical Chemistry B* **117**, 4634–4640 (2013).
- [146] R. W. Boyd, *Nonlinear optics* (Academic press, 2003).
- [147] W. Min, C. W. Freudiger, S. Lu, and X. S. Xie, “Coherent nonlinear optical imaging: Beyond fluorescence microscopy,” *Annual Review of Physical Chemistry* **62**, 507–530 (2011).
- [148] C. W. Freudiger, W. Min, B. G. Saar, S. Lu, G. R. Holtom, C. He, J. C. Tsai, J. X. Kang, and X. S. Xie, “Label-free biomedical imaging with high sensitivity by stimulated Raman scattering microscopy,” *Science* **322**, 1857–1861 (2008).
- [149] P. Nandakumar, A. Kovalev, and A. Volkmer, “Vibrational imaging based on stimulated Raman scattering microscopy,” *New Journal of Physics* **11**, 033026 (2009).
- [150] Y. Ozeki, Y. Kitagawa, K. Sumimura, N. Nishizawa, W. Umemura, S. Kajiyama, K. Fukui, and K. Itoh, “Stimulated raman scattering microscope with shot noise limited sensitivity using subharmonically synchronized laser pulses,” *Opt. Express* **18**, 13708–13719 (2010).
- [151] Y. Ozeki, W. Umemura, Y. Otsuka, S. Satoh, H. Hashimoto, K. Sumimura, N. Nishizawa, K. Fukui, and K. Itoh, “High-speed molecular spectral imaging of tissue with stimulated Raman scattering,” *Nat. Photon.* **6**, 845–851 (2012).
- [152] C. W. Freudiger, W. Min, G. R. Holtom, B. Xu, M. Dantus, and X. S. Xie, “Highly specific label-free molecular imaging with spectrally tailored excitation-stimulated Raman scattering (STE-SRS) microscopy,” *Nat. Photon.* **5**, 103–109 (2011).
- [153] F.-K. Lu, M. Ji, D. Fu, X. Ni, C. W. Freudiger, G. Holtom, and X. S. Xie, “Multicolor stimulated Raman scattering microscopy,” *Molecular Physics* **110**, 1927–1932 (2012).
- [154] D. Fu, F.-K. Lu, X. Zhang, C. Freudiger, D. R. Pernik, G. Holtom, and X. S. Xie, “Quantitative chemical imaging with multiplex stimulated Raman scattering microscopy,” *Journal of the American Chemical Society* **134**, 3623–3626 (2012).

- [155] P. Kukura, D. W. McCamant, and R. A. Mathies, “Femtosecond stimulated Raman spectroscopy,” *Annual Review of Physical Chemistry* **58**, 461–488 (2007).
- [156] R. Frontiera and R. Mathies, “Femtosecond stimulated Raman spectroscopy,” *Laser Photonics Reviews* **5**, 102–113 (2011).
- [157] E. Ploetz, B. Marx, T. Klein, R. Huber, and P. Gilch, “A 75 MHz light source for femtosecond stimulated Raman microscopy,” *Opt. Express* **17**, 18612–18620 (2009).
- [158] H. Frostig, O. Katz, A. Natan, and Y. Silberberg, “Single-pulse stimulated Raman scattering spectroscopy,” *Opt. Lett.* **36**, 1248–1250 (2011).
- [159] M. D. Levenson and S. Kano, *Introduction to nonlinear laser spectroscopy* (Academic Press (Boston), 1988).
- [160] D. Heiman, R. W. Hellwarth, M. D. Levenson, and G. Martin, “Raman-induced Kerr effect,” *Phys. Rev. Lett.* **36**, 189–192 (1976).
- [161] S. Shim and R. A. Mathies, “Femtosecond Raman-induced Kerr effect spectroscopy,” *Journal of Raman Spectroscopy* **39**, 1526–1530 (2008).
- [162] B. R. Bachler, M. E. Fermann, and J. P. Ogilvie, “Multiplex Raman induced Kerr effect microscopy,” *Opt. Express* **20**, 835–844 (2012).
- [163] C. W. Freudiger, M. B. J. Roeffaers, X. Zhang, B. G. Saar, W. Min, and X. S. Xie, “Optical heterodyne-detected Raman-induced Kerr effect (OHD-RIKE) microscopy,” *The Journal of Physical Chemistry B* **115**, 5574–5581 (2011).
- [164] V. Kumar, M. Casella, E. Molotokaite, D. Gatti, P. Kukura, C. Manzoni, D. Polli, M. Marangoni, and G. Cerullo, “Balanced-detection Raman-induced Kerr-effect spectroscopy,” *Phys. Rev. A* **86**, 053810 (2012).
- [165] L.-S. Ma, R. K. Shelton, H. C. Kapteyn, M. M. Murnane, and J. Ye, “Sub-10-femtosecond active synchronization of two passively mode-locked Ti:sapphire oscillators,” *Phys. Rev. A* **64**, 021802 (2001).
- [166] R. K. Shelton, S. M. Foreman, L.-S. Ma, J. L. Hall, H. C. Kapteyn, M. M. Murnane, M. Notcutt, and J. Ye, “Subfemtosecond timing jitter between two independent, actively synchronized, mode-locked lasers,” *Opt. Lett.* **27**, 312–314 (2002).

- [167] E. O. Potma, D. J. Jones, J.-X. Cheng, X. S. Xie, and J. Ye, “High-sensitivity coherent anti-Stokes Raman scattering microscopy with two tightly synchronized picosecond lasers,” *Opt. Lett.* **27**, 1168–1170 (2002).
- [168] D. J. Jones, E. O. Potma, J.-X. Cheng, B. Burfeindt, Y. Pang, J. Ye, and X. S. Xie, “Synchronization of two passively mode-locked, picosecond lasers within 20 fs for coherent anti-Stokes Raman scattering microscopy,” *Review of Scientific Instruments* **73**, 2843–2848 (2002).
- [169] H. Carleton and W. Maloney, “A balanced optical heterodyne detector,” *Applied Optics* **7**, 1241 (1968).
- [170] R. Stierlin, R. Bättig, P.-D. Henchoz, and H. Weber, “Excess-noise suppression in a fibre-optic balanced heterodyne detection system,” *Optical and Quantum Electronics* **18**, 445–454 (1986).
- [171] J.-X. Cheng and X. S. Xie, “Coherent anti-Stokes Raman scattering microscopy: Instrumentation, theory, and applications,” *The Journal of Physical Chemistry B* **108**, 827–840 (2004).
- [172] A. Volkmer, J.-X. Cheng, and X. Sunney Xie, “Vibrational imaging with high sensitivity via epidetected coherent anti-Stokes Raman scattering microscopy,” *Phys. Rev. Lett.* **87**, 023901 (2001).
- [173] J.-X. Cheng, L. D. Book, and X. S. Xie, “Polarization coherent anti-Stokes Raman scattering microscopy,” *Opt. Lett.* **26**, 1341–1343 (2001).
- [174] F. Lu, W. Zheng, C. Sheppard, and Z. Huang, “Interferometric polarization coherent anti-Stokes Raman scattering (IP-CARS) microscopy,” *Opt. Lett.* **33**, 602–604 (2008).
- [175] A. Volkmer, L. D. Book, and X. Xie, “Time-resolved coherent anti-Stokes Raman scattering microscopy: Imaging based on Raman free induction decay,” *Applied Physics Letters* **80**, 1505–1507 (2002).
- [176] C. L. Evans, E. O. Potma, and X. S. Xie, “Coherent anti-Stokes Raman scattering spectral interferometry: determination of the real and imaginary components of nonlinear susceptibility $\chi(3)$ for vibrational microscopy,” *Opt. Lett.* **29**, 2923–2925 (2004).

- [177] S.-H. Lim, A. G. Caster, and S. R. Leone, “Single-pulse phase-control interferometric coherent anti-Stokes Raman scattering spectroscopy,” *Phys. Rev. A* **72**, 041803 (2005).
- [178] D. Marks, C. Vinegoni, J. S. Bredfeldt, and S. Boppart, “Interferometric differentiation between resonant coherent anti-Stokes Raman scattering and nonresonant four-wave-mixing processes,” *Applied Physics Letters* **85**, 5787–5789 (2004).
- [179] E. O. Potma, C. L. Evans, and X. S. Xie, “Heterodyne coherent anti-Stokes Raman scattering (CARS) imaging,” *Opt. Lett.* **31**, 241–243 (2006).
- [180] B. von Vacano, T. Buckup, and M. Motzkus, “Highly sensitive single-beam heterodyne coherent anti-Stokes Raman scattering,” *Opt. Lett.* **31**, 2495–2497 (2006).
- [181] M. Jurna, J. P. Korterik, C. Otto, J. L. Herek, and H. L. Offerhaus, “Background free CARS imaging by phase sensitive heterodyne CARS,” *Opt. Express* **16**, 15863–15869 (2008).
- [182] N. Dudovich, D. Oron, and Y. Silberberg, “Single-pulse coherently controlled nonlinear Raman spectroscopy and microscopy,” *Nature* **418**, 512–514 (2002).
- [183] S.-H. Lim, A. G. Caster, O. Nicolet, and S. R. Leone, “Chemical imaging by single pulse interferometric coherent anti-Stokes Raman scattering microscopy,” *The Journal of Physical Chemistry B* **110**, 5196–5204 (2006).
- [184] H. Li, D. A. Harris, B. Xu, P. J. Wrzesinski, V. V. Lozovoy, and M. Dantus, “Coherent mode-selective Raman excitation towards standoff detection,” *Opt. Express* **16**, 5499–5504 (2008).
- [185] Y. Silberberg, “Quantum coherent control for nonlinear spectroscopy and microscopy,” *Annual Review of Physical Chemistry* **60**, 277–292 (2009).
- [186] E. M. Vartiainen, H. A. Rinia, M. Müller, and M. Bonn, “Direct extraction of Raman line-shapes from congested CARS spectra,” *Opt. Express* **14**, 3622–3630 (2006).
- [187] Y. Liu, Y. J. Lee, and M. T. Cicerone, “Broadband CARS spectral phase retrieval using a time-domain Kramers–Kronig transform,” *Opt. Lett.* **34**, 1363–1365 (2009).

- [188] F. Ganikhanov, C. L. Evans, B. G. Saar, and X. S. Xie, "High-sensitivity vibrational imaging with frequency modulation coherent anti-Stokes Raman scattering (FM CARS) microscopy," *Opt. Lett.* **31**, 1872–1874 (2006).
- [189] B. G. Saar, G. R. Holtom, C. W. Freudiger, C. Ackermann, W. Hill, and X. S. Xie, "Intracavity wavelength modulation of an optical parametric oscillator for coherent Raman microscopy," *Opt. Express* **17**, 12532–12539 (2009).
- [190] Y. Yan, E. B. Gamble, and K. A. Nelson, "Impulsive stimulated scattering: General importance in femtosecond laser pulse interactions with matter, and spectroscopic applications," *The Journal of Chemical Physics* **83**, 5391–5399 (1985).
- [191] Y. Yan and K. A. Nelson, "Impulsive stimulated light scattering. I. general theory," *The Journal of Chemical Physics* **87**, 6240–6256 (1987).
- [192] S. D. Silvestri, J. Fujimoto, E. Ippen, E. B. G. Jr., L. R. Williams, and K. A. Nelson, "Femtosecond time-resolved measurements of optic phonon dephasing by impulsive stimulated raman scattering in α -perylene crystal from 20 to 300 K," *Chemical Physics Letters* **116**, 146 – 152 (1985).
- [193] S. Ruhman, A. G. Joly, and K. A. Nelson, "Time-resolved observations of coherent molecular vibrational motion and the general occurrence of impulsive stimulated scattering," *The Journal of Chemical Physics* **86**, 6563–6565 (1987).
- [194] L. R. Williams and K. A. Nelson, "Excimer formation in pyrene molecular crystal: Femtosecond dynamics of an oriented bimolecular reaction," *The Journal of Chemical Physics* **87**, 7346–7347 (1987).
- [195] H. Graener and A. Laubereau, "High resolution Fourier transform Raman spectroscopy with ultrashort laser pulses," *Optics Communications* **54**, 141 – 146 (1985).
- [196] J. P. Ogilvie, E. Beaurepaire, A. Alexandrou, and M. Joffre, "Fourier-transform coherent anti-Stokes Raman scattering microscopy," *Opt. Lett.* **31**, 480–482 (2006).
- [197] N. Dudovich, D. Oron, and Y. Silberberg, "Single-pulse coherent anti-Stokes Raman spectroscopy in the fingerprint spectral region," *The Journal of Chemical Physics* **118**, 9208–9215 (2003).

- [198] M. Cui, M. Joffre, J. Skodack, and J. P. Ogilvie, “Interferometric Fourier transform coherent anti-Stokes Raman scattering,” *Opt. Express* **14**, 8448–8458 (2006).
- [199] A. M. Weiner, D. E. Leaird, G. P. Wiederrecht, and K. A. Nelson, “Femtosecond multiple-pulse impulsive stimulated Raman scattering spectroscopy,” *J. Opt. Soc. Am. B* **8**, 1264–1275 (1991).
- [200] D. Schafer, J. A. Squier, J. v. Maarseveen, D. Bonn, M. Bonn, and M. Müller, “In situ quantitative measurement of concentration profiles in a microreactor with submicron resolution using multiplex CARS microscopy,” *Journal of the American Chemical Society* **130**, 11592–11593 (2008).
- [201] K. P. Knutsen, B. M. Messer, R. M. Onorato, and R. J. Saykally, “Chirped coherent anti-Stokes Raman scattering for high spectral resolution spectroscopy and chemically selective imaging,” *The Journal of Physical Chemistry B* **110**, 5854–5864 (2006).
- [202] B. von Vacano and M. Motzkus, “Time-resolving molecular vibration for microanalytics: single laser beam nonlinear Raman spectroscopy in simulation and experiment,” *Phys. Chem. Chem. Phys* **10**, 681–691 (2008).
- [203] C. L. Evans, E. O. Potma, M. Puoris’haag, D. Côté, C. P. Lin, and X. S. Xie, “Chemical imaging of tissue in vivo with video-rate coherent anti-Stokes Raman scattering microscopy,” *Proceedings of the National Academy of Sciences of the United States of America* **102**, 16807–16812 (2005).
- [204] M. Müller and J. M. Schins, “Imaging the thermodynamic state of lipid membranes with multiplex CARS microscopy,” *The Journal of Physical Chemistry B* **106**, 3715–3723 (2002).
- [205] T. C. Briles, D. C. Yost, A. Cingöz, J. Ye, and T. R. Schibli, “Simple piezoelectric-actuated mirror with 180 kHz servo bandwidth,” *Opt. Express* **18**, 9739–9746 (2010).
- [206] K. Iwakuni, H. Inaba, Y. Nakajima, T. Kobayashi, K. Hosaka, A. Onae, and F.-L. Hong, “Narrow linewidth comb realized with a mode-locked fiber laser using an intra-cavity waveguide electro-optic modulator for high-speed control,” *Opt. Express* **20**, 13769–13776 (2012).

-
- [207] M. Cui, J. Skodack, and J. P. Ogilvie, “Chemical imaging with Fourier transform coherent anti-Stokes Raman scattering microscopy,” *Appl. Opt.* **47**, 5790–5798 (2008).
- [208] A. Wipfler, T. Buckup, and M. Motzkus, “Multiplexing single-beam coherent anti-Stokes Raman spectroscopy with heterodyne detection,” *Applied Physics Letters* **100**, 071102 (2012).
- [209] A. Bartels, D. Heinecke, and S. A. Diddams, “10-GHz self-referenced optical frequency comb,” *Science* **326**, 681 (2009).
- [210] C. Steuwe, C. F. Kaminski, J. J. Baumberg, and S. Mahajan, “Surface enhanced coherent anti-Stokes Raman scattering on nanostructured gold surfaces,” *Nano Letters* **11**, 5339–5343 (2011).
- [211] K. Hiramatsu, M. Okuno, H. Kano, P. Leproux, V. Couderc, and H. Hamaguchi, “Observation of Raman optical activity by heterodyne-detected polarization-resolved coherent anti-Stokes Raman scattering,” *Phys. Rev. Lett.* **109**, 083901 (2012).
- [212] T. Ichimura, N. Hayazawa, M. Hashimoto, Y. Inouye, and S. Kawata, “Tip-enhanced coherent anti-Stokes Raman scattering for vibrational nanoimaging,” *Phys. Rev. Lett.* **92**, 220801 (2004).
- [213] C. Cleff, P. Groß, C. Fallnich, H. L. Offerhaus, J. L. Herek, K. Kruse, W. P. Beeker, C. J. Lee, and K.-J. Boller, “Ground-state depletion for subdiffraction-limited spatial resolution in coherent anti-Stokes Raman scattering microscopy,” *Phys. Rev. A* **86**, 023825 (2012).

List of Publications

An octave spanning mid-infrared frequency comb generated in a silicon nanophotonic wire waveguide

B. Kuyken, T. Ideguchi, S. Holzner, M. Yan, T. W. Hänsch, J. Van Campenhout, P. Verheyen, F. Leo, R. Baets, G. Roelkens, and N. Picqué
in preparation

Few-cycle, Broadband, Mid-infrared Optical Parametric Oscillator Pumped by a 20-fs Ti:sapphire Laser

S. Chaitanya Kumar, A. Esteban-Martin, T. Ideguchi, M. Yan, S. Holzner, T. W. Hänsch, N. Picqué, and M. Ebrahim-Zadeh
in preparation

Differential femtosecond coherent Stokes and anti-Stokes Raman spectroscopy

T. Ideguchi, S. Holzner, M. Yang, G. Guelachvili, T. W. Hänsch, and N. Picqué
in preparation

Broadband high-resolution two-photon spectroscopy with laser frequency combs

A. Hipke, S. A. Meek, T. Ideguchi, T. W. Hänsch, and N. Picqué
arXiv:1311.6138 (2013). Submitted

Adaptive real-time dual-comb spectroscopy

T. Ideguchi, A. Poisson, G. Guelachvili, N. Picqué, and T. W. Hänsch
Nature Communications **5**, 3375 (2014).

Coherent Raman spectro-imaging with laser frequency comb

T. Ideguchi, S. Holzner, B. Bernhardt, G. Guelachvili, N. Picqué, and T. W. Hänsch
Nature **502**, 355-358 (2013).

Adaptive dual-comb spectroscopy in the green

T. Ideguchi, A. Poisson, G. Guelachvili, T. W. Hänsch, and N. Picqué
Optics Letters **37**, 4847-4849 (2012).

Raman-induced Kerr-effect dual-comb spectroscopy

T. Ideguchi, B. Bernhardt, G. Guelachvili, T. W. Hänsch, and N. Picqué
Optics Letters **37**, 4498-4500 (2012).

Conference contributions

Adaptive Dual-Comb Spectroscopy with Free-Running Lasers

T. Ideguchi, S. Holzner, B. Bernhardt, G. Guelachvili, N. Picqué, and T. W. Hänsch
Conference on Lasers and Electro-Optics Pacific Rim (CLEO-PR) 2013 , Kyoto, Japan
(2013)

Dual-Comb Coherent Raman Spectro-Imaging

S. Holzner, T. Ideguchi, B. Bernhardt, G. Guelachvili, N. Picqué, and T. W. Hänsch
Conference on Lasers and Electro-Optics Pacific Rim (CLEO-PR) 2013 , Kyoto, Japan
(2013)

Simultaneous Coherent Stokes and Anti-Stokes Raman Spectroscopy with Two Laser Frequency Combs

S. Holzner, T. Ideguchi, G. Guelachvili, T. W. Hänsch, and N. Picqué
Conference on Lasers and Electro-Optics (CLEO) 2013, San Jose, USA Paper: CTu3E.1
(2013)

Coherent anti-Stokes Raman dual-comb spectro-microscopy

T. Ideguchi, S. Holzner, B. Bernhardt, G. Guelachvili, N. Picqué, and T. W. Hänsch
Conference on Lasers and Electro-Optics (CLEO) 2013, San Jose, USA Paper: CTu3H.2
(2013)

Ultra-rapid anti-Stokes Raman dual-comb spectroscopy and microscopy

T. Ideguchi, S. Holzner, B. Bernhardt, G. Guelachvili, N. Picqué, and T. W. Hänsch
The European Conference on Lasers and Electro-Optics (CLEO/Europe) 2013, München,
Germany, paper: CH-5.2 (2013)

Femtosecond stimulated Raman Dual-Comb Spectroscopy (postdeadline)

T. Ideguchi, B. Bernhardt, G. Guelachvili, T. W. Hänsch, and N. Picqué
Conference on Lasers and Electro-Optics (CLEO) 2012, San Jose, USA Paper: CTh5C.6
(2012)

Real-time Dual-comb Spectroscopy of Iodine in the Visible

T. Ideguchi*, A. Poisson*, G. Guelachvili, T. W. Hänsch, and N. Picqué
Conference on Lasers and Electro-Optics (CLEO) 2012, San Jose, USA Paper: CW1J.3
(2012)

Adaptive Dual-Comb Spectroscopy with Free-running Lasers and Resolved Comb Lines (invited talk)

A. Poisson*, T. Ideguchi*, G. Guelachvili, N. Picqué, and T. W. Hänsch
Conference on Lasers and Electro-Optics (CLEO) 2012, San Jose, USA Paper: CW1J.1
(2012)

Fourier Transform Spectroscopy with Laser Frequency Combs (invited talk)

B. Bernhardt, T. Ideguchi, A. Poisson, T. W. Hänsch, N. Picqué and G. Guelachvili
OSA Fourier Transform Spectroscopy, Toronto, Canada, paper: FThB1 (2011)

Dual-comb spectroscopy with adaptive sampling (poster)

T. Ideguchi, A. Poisson, G. Guelachvili, T. W. Hänsch, and N. Picqué
The European Conference on Lasers and Electro-Optics (CLEO/Europe) 2011, München,
Germany, paper: CH.P.23 (2011)

Curriculum Vitae

Takuro Ideguchi
Max-Planck-Institut für Quanten Optik
Hans-Kopfermann-Straße 1
85748 Garching
Citizenship: Japanese
takuro.ideguchi@mpq.mpg.de

Personal Data

Date of birth: 29.04.1982
Place of birth: Ibaraki, Japan

Education

- 04/2010 - present Graduate student in the group of Theodor W. Hänsch at Max-Planck-Institute of Quantum Optics, Garching, Germany
- 04/2006 - 03/2008 Master's course studies in Department of Applied Physics at the University of Tokyo, Tokyo, Japan
Master's thesis in the group of Makoto Kuwata-Gonokami at the University of Tokyo, Tokyo, Japan
Subject: *Coherent quantum control of excitons at ultracold and high density in Cu_2O with phase manipulated pulses*
- 04/2002 - 03/2006 Undergraduate studies in Department of Applied Physics at the University of Tokyo, Tokyo, Japan
Bachelor's thesis in the group of Makoto Kuwata-Gonokami at the University of Tokyo, Tokyo, Japan
Subject: *Laser-based continuous-wave excitonic Lyman spectroscopy in Cu_2O*

Working experience

- 04/2008 - 03/2010 Canon Inc., Ibaraki, Japan

Awards

- 06/2013 Theodore Maiman Student Paper Competition Semi-Finalist (OSA Foundation, Conference on Lasers and Electro-Optics 2013)
- 05/2012 Theodore Maiman Student Paper Competition Semi-Finalist (OSA Foundation, Conference on Lasers and Electro-Optics 2012)
- 12/2009 Best patent Award in Development Center of Electrophotography in Canon Inc.
- 03/2008 Shoji Tanaka Award (The Best Master Thesis Award in Department of Applied Physics in the University of Tokyo)

Acknowledgments

First of all, I sincerely thank Professor **Theodor W. Hänsch** for giving me the wonderful opportunity to work with him and many outstanding scientists in his group. His deep insight and curiosity about science have stimulated me all the time and I learned a lot of things from his attitude to science. I will keep in mind that individual curiosity drives creating new science and technology.

I send my best thank to **Nathalie Picqué** who gave me the great theme to explore. I very much respect her attitude to science which often brings new ideas to her mind. We have shared lots of experimental accomplishments and each of them was very exciting. I have been very much encouraged by her “Congratulations”. All what I have learned from her have built the foundation of my scientific activity.

I send my thank to **Guy Guelachvili** for his essential comments to our experiments and drafts of publications. It was indirect connection but I believe the work in this thesis gained a lot from his experience.

Birgitta Bernhardt was always nice and her kind help and suggestions made my experiments went smoothly. Her decision making process was logical and it was nice to work with her. Vielen Dank, Birgitta.

The work “Adaptive dual-comb spectroscopy” was made with **Antonin Poisson**. It was one of the best moments that we made the experimental success together in the lab. Merci, Antonin.

It was nice to work with **Arthur Hipke** in the same group. We shared knowledge about our experiments and I’m happy that both of our experiments went pretty well. The ski trip with him was really cool experience. Vielen Dank, Arthur.

The work “Coherent anti-Stokes Raman spectroscopy and microscopy” was made with **Simon Holzner**. I pretty much enjoyed talking with him not only about our experiments but also about topics in our daily lives. Japan trip with him was a good memory. Vielen Dank, Simon.

I was happy to share our time with **Samuel Meek** in the same group and enjoyed talking with him. I have been impressed by his way of thinking about science and technology. Biergarten events were parts of good memories in Munich. Thank you, Sam.

I send my thank to **Eugene Frumker** who shared some time in the same group. I enjoyed talking with him about science and technology as well as topics in our daily lives.

It was nice to work with **Ming Yan** who joined my experiments at the late stage of this

thesis work. We shared Asian spirits in the European group. Xie xie, Ming.

Clément Lafargue is the newest member who joined our group. It was nice to work with him in the lab. I learned French way of life from him. Merci, Clément.

Professor **Majid Ebrahim-Zadeh**, **Chaitanya Kumar Suddapalli**, and **Adolfo Esteban-Martin** were the collaborators who developed the “Mid-infrared frequency comb base on optical parametric oscillator” together. Visiting their lab at ICFO in Barcelona and working with them was really nice experience. The experiments at MPQ together were also nice memory. Gracias, Majid, Chaitanya and Adolfo.

Professor **Roel Baets**, Professor **Gunther Roelkens**, and **Bart Kuyken** were the collaborators who made the “Mid-infrared supercontinuum generation in silicon waveguide” together. I very much thank them for such a nice collaboration between Belgium and Germany. Working with Bart in the lab at MPQ till late at night and finally having the nice results was good memory. Heel hartelijk bedankt, prof. Baets, prof. Roelkens, and Bart.

Thomas Udem always stimulated me by his deep understanding about Physics. His unique way of explanation always get essence of the subject and simplifies complicated physics. Vielen Dank, Thomas.

Ronald Holzwarth paved the road for me to come to MPQ. His kind invitation to Munich was the start point of my long journey to Germany after talking with him at an Izakaya bar in Tokyo. Vielen Dank, Ronald.

I thank **Akira Ozawa** who was the very first contact person in Hänsch group. I appreciated his kind answer to my email.

I thank **Peter Hommelhoff**, **Randolf Pohl**, **Masaki Hori**, **Harald Weinfurter** and **David Hunger** who have lead their groups and given me lots of opportunities to learn many interesting physics through their outstanding researches. Their questions and comments to my works always got points and made me think about my works more deeply.

I send my thank to **Alexey**, **Andreas**, **Anna**, **Arthur M.**, **Axel**, **Camille**, **Christian P.**, **Christian S.**, **Christine**, **Daniel**, **Dylan**, **Elisabeth**, **Guido**, **Hanno**, **Jakob**, **Janis**, **Johannes G.**, **Johannes H.**, **John**, **Josue**, **Julian**, **Katharina**, **Lothar**, **Marc**, **Markus**, **Max**, **Michael F.**, **Michael K.**, **Pascal**, **Pierre**, **Rafael**, **Remi**, **Roman**, **Sebastian K.**, **Sebastian T.**, **Stefan**, **Taku**, **Tilo**, **Tino**, **Tobi**, **Tobias N.**, **Tobias L.**, **Tobias W.**, who are my former and current colleagues around Hänsch group in MPQ. There have been a lot of fun with you all.

Many thanks to **Takeshi Fukuhara** and **Toshiyuki Tashima** who spent MPQ life to-

gether as Japanese colleagues. It was always nice to go drinking with you.

I thank **Helmut Brücker**, **Wolfgang Simon**, and **Karl Linner** for helping my experiments with their professional engineering supports.

Many thanks to Ms.**Ingrid Hermann** and Ms.**Gabriele Gschwendtner** who have helped me a lot for administrative things.

Finally I warmly thank my family and friends who have supported me from all over the world.